UNIVERSITA' DEGLI STUDI DI PADOVA
DIPARTIMENTO DI INGEGNERIA INDUSTRIALE - DII
CORSO DI LAUREA MAGISTRALE IN
INGEGNERIA CHIMICA E DEI PROCESSI INDUSTRIALI

Tesi di Laurea Magistrale in Ingegneria Chimica e dei Processi Industriali

METHANOL GAS-PHASE ABATEMENT IN A MEMBRANE PHOTOREACTOR BY MEANS OF INNOVATIVE NANOCOMPOSITE CATALYSTS

Relatore: Ing. Martina Roso
Correlatore: Prof. Michele Modesti

Laureando: Stefano Guerra
matricola: 1177762

ANNO ACCADEMICO: 2018-2019

Abstract

In this work, the design and the development of a new photoreactor are carried out to perform gaseous photocatalytic oxidation of methanol in air stream. The photoreactor is equipped with a nanostructured membrane obtained via electrospinning: the optimization of the process conditions is carried out. On the membrane surface, eight different catalysts are deposited. Namely, they are formed by titanium and cerium dioxides, mixed in different concentrations with graphene. They are prepared according to two innovative synthetic techniques, recently developed for this purpose: mechano-chemical and top-down routes. The reaction, that occurs at room temperature, is activated by UV-radiation: two lamps are tested (UV-A and UV-C).

The catalysts are characterized by UV-Vis Diffuse Reflectance Spectroscopy (DRS) and Scattered Electron Microscopy (SEM); the membranes obtained via electrospinning are characterized with Thermo Gravimetric Analysis (TGA) and SEM.

The membranes are tested in a batch reactor with recycle for several days. UV-A lamp does not provide promising results, while UV-C lamp activates the reaction. Seven catalysts out eight display photocatalytic activity, but their specific performances can be compared to the benchmark titanium dioxide.

Riassunto esteso

La crescita industriale sviluppatasi negli ultimi decenni ha causato, tra le molte conseguenze, un inquinamento degli ambienti esterni molto pronunciato. La comunita' scientifica e l'opinione pubblica stanno monitorando questo problema e stanno cercando soluzioni atte a porvi rimedio. Cio' nonostante, un aspetto trascurato e' l'inquinamento dei luoghi confinati (case, scuole, ospedali, luoghi di lavoro, di svago, di cura, etc.). Questi luoghi sono caratterizzati dall'inquinamento *indoor* che si origina da solventi, prodotti per la pulizia, vernici, ma anche muffe e batteri. Solo negli ultimi decenni, la comunita' scientifica sta indagando anche questo ambito; questo e' infatti un problema attuale poiche' di media, un individuo trascorre piu' dell' 80% della sua giornata in ambienti chiusi e poiche' la concentrazione di inquinanti in ambienti confinati puo' essere fino a 5 volte quella dell'esterno.

Tra i vari composti dannosi per l'uomo, ne esiste una classe particolarmente pericolosa: COV (Composti Organici Volatili), caratterizzati da una bassa temperatura di ebollizione e quindi facilmente rintracciabili nell'aria in piccole concentrazioni. Questi composti possono essere responsabili di molti sintomi, che sebbene aspecifici e di minore intensita', possono portare negli anni all'insorgenza di malattie a carico del sistema circolatorio, respiratorio. La messa a punto di sistemi che permettano l'abbattimento di questo tipo di composti chimici e' l'obiettivo di questo lavoro.

Diverse tecniche esistono per condurre l'abbattimento di questi composti: tuttavia queste tecniche sono adattabili al solo ambito industriale, mentre manca un'applicazione a livello civile e domestico. Una di queste tecniche e' la fotocatalisi eterogenea. In questa tecnica un catalizzatore (in questo caso ossidi di semiconduttori), previa attivazione con radiazione UV, puo' catalizzare l'abbattimento degli inquinanti. Questa tecnica ha molti vantaggi, tra i quali la possibilita' di lavorare in condizioni miti di temperatura e pressione, la caratteristica peculiare di portare alla distruzione completa degli inquinanti (le

altre tecniche, invece, favoriscono il passaggio dell'inquinante da una fase all'altra), la non-selettivita' verso gli inquinanti e la produzione di specie chimiche meno tossiche. Il materiale impiegato piu' tradizionale e' l'ossido di titanio (TiO_2) ma in questa tesi e' stato valutato anche l'ossido di cerio (CeO_2). Questi catalizzatori sono stati miscelati in maniera diversa con il grafene. Questo materiale, scoperto solo nel 2004, ha attirato l'attenzione nell'ambito della fotocatalisi, perche' migliora le proprieta' catalitiche del semiconduttore con il quale e' accoppiato, aumentando la possibilita' che l'inquinante venga ossidato. Questi catalizzatori sono stati prodotti con due tecniche specifiche: la prima tecnica e' chiamata sintesi meccano-chimica, nella quale, come e' stato mostrato di recente, l'intimo contatto tra due diverse specie fornisce proprieta' particolari, superiori alla semplice miscelazione. La seconda tecnica e' chiamata *top-down*: con questa preparazione, diverse interazioni chimiche tra le due specie vengono a formarsi.

Le reazioni di foto-ossidazione catalitica avvengono su membrane sulle quali sono depositati questi catalizzatori. Le membrane sono costituite da nanofibre ottenute per elettrofilatura. Questa tecnica e' molto promettente per la realizzazione di materiali e strutture di dimensioni nanometriche, ma che possiedano elevata area superficiale. I nanomateriali possiedono infatti, caratteristiche peculiari che massimizzano le velocita' di reazione. I catalizzatori sono depositati poi sulle membrane elettrofilate con una tecnica di atomizzazione, chiamata *electrospraying*.

In questo lavoro, la produzione, l'assemblaggio delle membrane sono stati studiati e ottimizzati prendendo in considerazione diverse opportunita': la membrana, con gli appositi supporti e' stata inserita in un fotoreattore. La progettazione del fotoreattore e' stata condotta in questa tesi di laurea, andando a sfruttare la radiazione emessa da una sorgente UV, ponendo la membrana coassialmente rispetto all'asse della lampada. Cosi' facendo, l'intensita' della radiazione e' stata massimizzata. L'aria tecnica di bombola, opportunamente inquinata di metanolo e' stata flussata all'interno del fotoreattore batch con ricircolo. Per monitorare l'abbattimento del metanolo nel tempo si e' impiegato un gas cromatografo abbinato ad uno spettrometro di massa.

Le tecniche analitiche impiegate sono qui elencate. I catalizzatori sono stati caratterizzati con spettroscopia UV-Visibile in riflettanza diffusa, le membrane sono state caratterizzate con analisi termogravimetriche, attraverso il microscopio a trasmissione elettronica e con diffrazione a raggi X.

Otto catalizzatori sono stati testati, supportati su altrettante membrane in poli-acrilonitrile (PAN); due diverse lampade sono state impiegate: una con spettro di emissione nell'UV-A, l'altra nell'UV-C.

Mentre la lampada UV-A non ha attivato le reazioni di fotoossidazione, la lampada UV-C ha favorito l'abbattimento del metanolo. Dopo 6 ore di reazione, la conversione del metanolo si e' attestata nei casi migliori al 60-70%, mentre nella maggior parte dei casi, la conversione finale e' stata del 30-40%. Lo studio delle performance catalitiche ha permesso di valutare quale tecnica di sintesi fornisca i risultati piu' soddisfacenti. Si evidenzia, in conclusione, come l'attivita' dei nanocompositi risulti comparabile a quella del biossido di titanio.

Futuri sviluppi in questo ambito riguardano l'ottimizzazione della deposizione del catalizzatore, al fine di renderlo il piu' omogeneo possibile sulla superficie delle fibre e la valutazione della quantita' di catalizzatore per evitare effetti di schermaggio che diminuiscono l'attivita' fotocatalitica.

Contents

Introduction

In the last decades, the changed human activities have led to an increased attention on the indoor air pollution problem (i.e. the presence of chemical compounds, but also dust, bacteria and other biological contaminants), that is common of confined buildings, such as offices, houses, commercial facilities. This issue is a current problem, since it has been calculated that, on average, people spend more than the 80% of their daily life in closed spaces. Furthermore, in some extreme cases, the concentration of organic pollutants is higher in indoor environment, with respect to outdoor: the public concern, however, is focused only on the latter one.

Among all the contaminants, volatile organic compounds are chemical compounds characterized by low boiling point: for that reason, they easily evaporate and they can be found in gas phase in small concentration. However, the presence of small amount of these contaminants is responsible of a series of minor diseases, grouped together under the name of "Sick Building Syndrome".

The removal techniques are restricted nowadays to industrial scale and the application on the civil scale is limited. For that reason, different technologies are needed to perform pollutant abatement. Nanotechnology offers innovative tools to prepare photo-catalytic membranes that can accomplish pollutant removal. These nanostructured membranes have high specific surface and good photocatalytic performances.

The objectives of this work are to size a new type of nanostructured membrane reactor and to assess its photocatalytic performances with an air stream polluted with methanol. For these reason, different catalysts are tested (titanium dioxide, cerium dioxide, mixed or milled with graphene, according to different preparation routes) supported on nanostructured membranes obtained via electrospinning. These nanocomposites are synthetized with innovative techniques that are proven to provide intimate coupling between the catalysts. The work is divided into six Chapters:

- Chapter 1 deals with air pollution issue of confined environments, then the techniques used to remove chemical compounds are described.
- In Chapter 2 heterogeneous photocatalysis (one of the chemical compound removal techniques) is described: in particular, photocatalytic oxidation is explained and the mechanism of methanol oxidation is reported.
- Chapter 3 focuses on electrospinning method to prepare nanofibers and membranes; then the different parameters that can play a role on this process are analyzed.
- Chapter 4 deals with the material employed in this work, the instruments used and the analytical techniques employed.
- In Chapter 5 the optimization of electrospinning and electrospraying processes is presented and the characterization of the catalysts and of the electrospun membranes is then carried out.
- Finally, Chapter 6 deals with the experimental setup to carry out photocatalytic oxidation of methanol. The reactor and the lab-scale plant is first described; then the photocatalytic performances are then described and compared.

The experimental tests are carried out in the Polymer Engineering Group laboratories in the Industrial Engineeering Department, University of Padova, in collaboration with the University of Udine.

Chapter 1

Air Pollution

In this first Chapter, a brief outline of *Indoor Air Quality* (IAQ) and indoor air pollution is reported. Between all compounds that are responsible for pollution, particular importance is given to VOCs (*Volatile Organic Compounds*). Then, different air remediation techniques are reported, in particular heterogeneous photocatalysis.

1.1 Indoor air pollution

"*Indoor air pollution*" refers to the release of contaminants of different types (chemical or biological, particles or gases) in closed, confined places used for dwelling, recreation, job, in institution or commercial facilities. In this definition, industrial workplaces are not included, since the contaminants are strongly related to the industrial activity that takes place on them. In Italy a specific legislation exists for industrial workplaces[1].
Since the 1970s, there has been increasing concern within the scientific community over the effects of indoor air quality on human health (*Jones A.P.*, 1999). For example, the larger use of synthetic building materials have led to more comfortable and energy-efficient buildings, but, at the same time, new materials release contaminants that may build up to higher concentrations than outside. Not only synthetic new materials are sources of pollution: deteriorating materials can become friable and release pollutants into the air. Before 1970s, indoor air pollution was almost neglected and nowadays, even if the issue is serious, the bulk of public concern is focused mainly on the health effects of outdoor pollution, which is considered a bigger problem than indoor one.

[1]Decreto Legislativo 9 Aprile 2008, n. 81, *"Testo Unico sulla Sicurezza sul Lavoro"*, rev. Aprile 2019

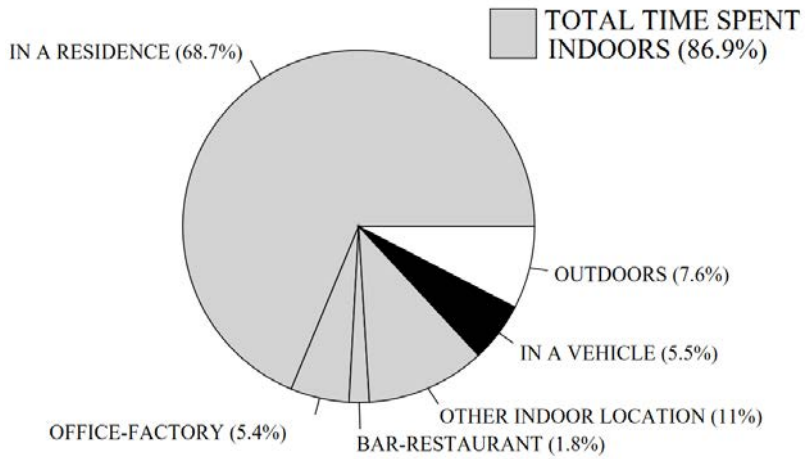

Figure 1.1: Pie chart showing the mean percentage of time the NHAPS respondents spent in six different locations on the diary day (weighted) (*Klepeis N.E. et al.*, 2001)

This public opinion is formed despite, in developed countries, on average, people spend more than 80% of their day inside buildings. In Figure 1.1 there is the graphical representation of NHAPS survey, two-year national probability telephone survey, conducted by the University of Maryland's Survey Research Center, from September 1992 through September 1994 (*Klepeis N.E. et al.*, 2001). The pie chart shows that, on average people spend indoors (residence, office or factory, bar or restaurant and other indoor locations) the 86.9% of their time.

Although there is no evidence that indoor exposure to contaminants is more harmful, it is proven that concentrations of pollutants are often higher than the one found outside.

Indoor air pollutants emanate from several sources (some of those are: adhesives, solvents, building materials, due to volatilization and fuel combustion processes, paints, tobacco smoke, fabric of buildings). Especially in the industrial zones with heavy traffic, outdoor sources can significantly contribute to indoor pollution. Also, tobacco smoke contributes to indoor pollution, since it releases thousand substances, like particles, vapors, gases. Contamination sources can be divided in two categories: continuous (caused by traffic, vehicles) and discontinuous (caused by detergents, maintenance, related to usage).

The actual human exposures are difficult to quantify since the behavior and activity of individuals affect the level of exposure. The individual sensitivity to contaminants, the concentration, the time and frequency of the exposure play a significant role on the out-

break of an illness.

Indoor pollutants can cause transient morbidity, disability, disease and even death in extreme cases. In the early 1970s, a new type of syndrome starts to appear: "*Sick Building Syndrome*" (SBS) in which occupants of buildings describe a broad range of vague, indefinite and subjective health complaints. Nose, eyes, throat irritation, headaches, dizziness, fatigue are examples of immediate effects of exposure. The symptoms are non-specific, relatively minor but are frequent among the occupant of "contaminated" buildings. SBS causes are several: indoor and outdoor pollutants diffusion, insufficient ventilation, presence of bacteria, mold, and factors as temperature and humidity. The symptoms often disappear after leaving the building, but sometimes they are responsible for long-term diseases: heart disease and respiratory problems are some examples. SBS normally is reported in offices, schools, hospitals, homes for elderly, apartments. Although SBS is considered a minor illness, its symptoms cause absenteeism and lowered productivity in workers. In conclusion, there is the need to further investigate the link between the indoor-air quality and health and to effectively contrast indoor air pollution.

Three methods are suggested to improve indoor air quality: 1) Source control: in some cases, harmful products can be avoided, but especially in metropolis, source control is ungovernable; 2) Increased ventilation, that however can transport more pollutant from the outdoor environment and 3) Air cleaning, which is the issue this work is based on, and it seems the most feasible option to improve air quality.

From normative standpoint, in Italy there is no legislation that rules air quality in closed environments. However, there are some guidelines.[2] In this guideline there are important indications for evaluating and manage risks related to indoor air pollution. Furthermore, there are indication to prevent and control it. For example, it is recommendable to build energy-efficient and environment-friendly edifices, to renovate old buildings, to do periodic maintenance on air conditioning systems. Furthermore, prudent lifestyles, the usage of products that are less harmful both for humans and environment can lead to a better air quality control in confined places. As matter of example there are: detergents that do not contain chlorine, ammonia or formaldehyde, water-based paints that have similar performance of the solvent-based products, along with the simplest action of frequent

[2] Gazzetta Ufficiale Suppl. Ordin. n. 276, 27/11/2011, *Linee guida per la tutela e la promozione della salute negli ambienti confinati.*

ventilation of confined environment.

1.2 Volatile Organic Compounds (VOCs)

Amongst all the types of contaminants, of particular importance are VOCs (*Volatile Organic Compounds*), due to their intrinsic danger potential and their wide use in every-day life. They are detrimental to human health, since they can cause Sick Building Syndrome outbreak. It is found that indoor air contains a larger number of VOCs at even higher concentration than outside. The mean concentration of each VOC is between 5 $\mu g/m^3$ and 50 $\mu g/m^3$ (*Brown et al*, 1994)
According to EPA (*Environmental Protection Agency*) VOC is "any compound of carbon, excluding carbon monoxide, carbon dioxide, carbonic acid, metallic carbides or carbonates, and ammonium carbonate, which participates in atmospheric photochemical reactions".
WHO (*World Health Organization*) defines VOCs as compounds that have a boiling point that ranges between 50 and 260℃, excluding pesticides. Their low boiling point means that they readily evaporate. They can easily evaporate, also in standard conditions (room temperature and atmospheric pressure). A compound is more volatile as its boiling temperature is lower. Applying this principle, organic compounds are classified into various categories which include: "*Very Volatile Organic Compounds*" (VVOCs), "*Volatile Organic Compounds*" (VOCs), "*Semi-Volatile Organic Compounds*" (SVOCs) and "*Non-Volatile Organic Compounds*" (NVOCs). In Table 1.1 there is the classification of the World Health Organization of VOC according to their boiling point.

VOCs can arise from paints, varnishes, solvents, preservatives. They are normally higher in newly constructed buildings or in those in which decoration works have recently taken place. Table 1.2 lists the classes of VOCs identified in indoor air, in which aromatics, aldehydes, and halocarbons are the most occurring compounds (*Cheng, Brown*, 2003): the emission sources reported in Table are: 1: Established buildings, 2: New and renovated buildings, 3: School, 4: New car interiors, 5: Carpets, 6: Floor coverings, 7: Wood-based panel and furniture, 8: Solid woods, 9: Paints, 10: Cleaning products, 11: Unflued gas heaters and electric ovens, 12: Office equipment.

In Table 1.3 there is a list of indoor pollutants and their sources (*Namiesnik et al.*,

Table 1.1: Volatile Organic Compounds according to WHO

Description	**Acronym**	**Boiling Point Range [℃]**	**Example Compounds**
Very Volatile Organic Compounds	VVOC	<0 to 50-100	Propane, butane, methyl chloride
Volatile Organic Compounds	VOC	50-100 to 240-260	Formaldehyde, toluene, acetone, ethanol, methanol
Semi Volatile Organic Compounds	SVOC	240-260 to 380-400	Pesticides (DDT), plasticizer (phthalates), fire retardants (PCBs,PBB)

Table 1.2: Volatile Organic Compounds: classification and emission sources (*Cheng, Brown*, 2003)

VOC	**1**	**2**	**3**	**4**	**5**	**6**	**7**	**8**	**9**	**10**	**11**	**12**
Aliphatic and cyclic hydrocarbons	x	x		x	x		x		x	x	x	
Aromatic hydrocarbons	x	x	x	x	x	x	x		x		x	x
Aldehydes	x	x	x	x	x	x	x	x	x	x	x	x
Terpenes	x	x	x	x			x	x	x	x		
Alcohols	x	x	x	x	x	x	x	x	x		x	
Esthers	x	x		x			x	x	x			
Halocarbons	x	x					x				x	
Glycols/glycolethers	x	x	x	x			x		x			
Ketones	x	x	x	x		x	x	x	x	x	x	x
Siloxanes											x	
Alkenes		x					x					
Organic acids		x	x				x	x	x		x	
Ethers									x			
Other VOCs	x	x		x			x				x	

Table 1.3: Specific indoor sources of organic vapors (*Namiesnik et al*, 1992)

Compounds	**Sources**
Formaldehyde	Pressed wood products, wood
Acetaldehyde	Glues, deodorants, fuels, preventives, mold growth on leathers
Benzene	smoking
Aromatic hydrocarbons	Paints, adhesives, gasoline, combustion sources
Aliphatic hydrocarbons	Paints, adhesives, gasoline, combustion products
Terpenes	Scented deodorizers, polishes, fabrics, fabric softener, cigarettes, food beverages
Alcohols	Aerosols, window cleaners, paints, paints thinners, cosmetics and adhesives
Ketones	Lacquers, varnishes, polish removers, adhesives
Ethers	Resins, paints, varnishes, lacquers, dyes, soaps, cosmetics
Esters	Plastic, resins, plasticizers, lacquers solvents, flavors, perfumes

1992). It is seen that construction coverings and household cleaning products are the bigger responsible for indoor pollution.

In order to quantify the concentration of VOCs it is useful to sum them up to compute the TVOCs (*Total Volatile Organic Compounds*), rather than individual values. However, it is important to note that average VOC concentrations may lead to inaccurate indication of personal exposures: individuals are often close to VOC sources or they may be subjected to pollutants emitted from substances on their person.

Exposure to VOC can result in acute and chronic health effects. VOCs at high concentration are potent narcotics, can depress the central nervous system, can lead irritation of the eyes, respiratory tracts, sensitization of eyes, skin, lungs, mucous membrane irritation. At higher concentration VOCs are responsible for headache, drowsiness, fatigue, and confusion, up to lethargy, dizziness. These symptoms can eventually progress to convulsion, coma and death. The health effects, however, depend on the pollutant, on its concentration and on the duration of exposition. Many VOCs are known to be toxic, carcinogenic, mutagenic o teratogenic. Frequent exposition, for example, to compound such as benzene, p-dichlorobenzene, chloroform, dichloromethane can cause cancer on-

Table 1.4: Physical-chemical properties of methanol, (Labchem, *Methanol Safety Data Sheet*)

Property	**Value**
Molar weight [g/mol]	32.04
Vapor pressure (25℃) [hPa]	128
Boiling temperature (1 atm) [℃]	64.65
Liquid density (20℃) [kg/m^3]	791
Vapor specific density (air = 1) [-]	1.1
Explosive limits in air, LEL-UEL [v/v]	5.5-36.5%
Flash point [℃]	9.7
Autoignition temperature [℃]	455

set. Therefore, developing new systems and technologies to perform VOCs abatement is of fundamental importance to improve air quality.

1.3 Methanol

Methanol (in the following sections labeled as "MeOH") is the simplest alcohol, with just one carbon atom, formed by a methyl bonded to a hydroxyl group. At room temperature is a light, volatile, colorless, flammable polar liquid. Its odor is similar to ethanol. The structure is reported in Fig. 1.2. The main physical-chemical properties are reported in Table 1.4. Since the boiling temperature is 64.6℃, according to the definition of WHO (Tab. 1.1), methanol is a VOC.

In closed environment there are different sources of emission: solvents, household cleaners, methylated spirit (denaturated alcohol), fungicides and insecticides, paints and paint products (such as thinners), varnish removers but also in architectural surface coatings. Furthermore, methanol originates from a wide range of microbiological processes (from decaying organic matter), biological decomposition of biological wastes, sewage, and sludge.
Methanol is a toxic component for human: toxicity can be of two different types:

1. Acute if referred to the effects that a substance can cause from a single exposure or from multiple exposures in a short period of time: the adverse effect should occur within 14-day period of the administration of the substance. Methanol is

harmful by ingestion, inhalation, skin absorption. If swallowed can cause damage to the liver, kidneys, heart. It can cause temporary or permanent blindness when ingested or passed through the skin: it acts as central nervous system depressant. Exposure to high concentrations can cause coma and even death.

2. Chronic if referred to the adverse effects due to long term exposure to a toxicant. Exposure to this pollutant may cause irritation of the eyes, nose, mouth and throat. Also, it can be responsible for liver damage, headaches, insomnia, cardiac depression, nausea, vomiting, blurred vision, optic nerve damage, dizziness and a feeling of intoxication. Methanol exposure may lead to severe abdominal, leg and back pain. Repeated contact can dry the skin, resulting in the skin cracking, peeling and itching. In this second case the accumulation of the toxicant within the body is responsible for toxicity.

The toxicity parameter are reported in Table 1.5. Table 1.6 makes a list of H-codes and H-phrases for this compound.
The Threshold Limit Value (TLV) of a chemical substance is the level to which a worker can be exposed day after day for a working lifetime without adverse effects, in particular:

1. TLV-TWA (*Time Weighted Average*) is average exposure on the basis of a 8h/day, 40h/week work schedule that does not cause any adverse effects,

2. TLV-STEL (*Short Time Exposure Limit*) is the value of 15-minute exposure that should not be exceeded at any time during a workday, even if the 8-hour TWA is within the TLV-TWA.

3. TLV-C (*Ceiling*) is the absolute exposure limit that should not be exceeded at any time.

4. LD_{50} (*Lethal Dose 50*) or LC_{50} (*Lethal Concentration 50*) is the amount of a toxic agent that is sufficient to kill the 50% of a population of animals (usually rats) within a certain time, computed statistically.

The *California Environmental Protection Agency* (CalEPA) has calculated a chronic inhalation reference exposure level of 10 mg/m^3 based on developmental effects in mice. The CalEPA reference exposure level is a concentration at or below which adverse health

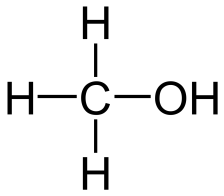

Figure 1.2: Methanol structure formula

Table 1.5: Toxicity of methanol

Parameter	Value
TLV-TWA [ppm]	200
TLV-STEL [ppm]	250
LD_{50} (rat inhalation, 4h)	64000

effects are not likely to occur. Methanol inhalation in rats leads to skeletal, cardiocirculatory and nervous apparatus deformity. Indeed, methanol does not have any reproductive or developmental effects in humans, furthermore there is no evidence of carcinogenic effects neither in humans nor in animals.
If emitted in atmosphere it reacts with hydroxyl radicals, formed via photochemical reaction, and it can lead to formaldehyde, which is carcinogenic. Hence, studying methanol abatement is important not only for the effects that the alcohol can induce, but also in order to prevent formaldehyde formation.

1.4 VOCs removal techniques

In this section different methods for VOC removal are described. Among them, there is heterogeneous photocatalysis, the technique adopted in this work, which is deeply

Table 1.6: H-phrases for methanol

Code	H-phrase
H225	Highly flammable liquid and vapor
H301	Toxic if swallowed
H311	Toxic in contact with skin
H331	Toxic if inhaled
H370	Causes damage to organs

described in the next Chapter.

1.4.1 Incineration

This technique deals with the total destruction of the organic compounds: it therefore does not allow the energy recovery from them. Pollutant is completely oxidized to obtain the products of total combustion (i.e. carbonic anhydride and water). Employing this technique, the abatement maximum efficiency obtained is higher than 95%. The efficiency is, however, function of different parameters: reactor residence time, temperature, turbulence inside the system. There are two types of incineration: thermal and catalytic. In the first case, which is employed frequently, the pollutant concentration is lower than the 50% of the LEL (*Lower Explosive Limit*, methanol LEL is reported in Table 1.4). Temperature ranges between 870 and 1200℃, depending on the pollutant, time residence between 0.75 and 2 s. The efficiency of the process is in the range 95-99.9%; in order to obtain the highest level of oxidation a residence time higher than 1 s is needed.
In the second case, catalytic incineration is used with pollutant concentration lower than 25% of LEL, the temperature between 315 and 540/650℃, depending on the pollutant, space velocity in the range 10 000 (alkali metals) and 40 000 (noble metals) h^{-1}. Space velocity depends on the employed catalysts and is the ratio of gas velocity and height of catalytic bed. Catalysts are generally oxides of noble metals, as platinum, palladium, vanadium, titanium and manganese.

1.4.2 Adsorption

This techniques is characterized by the transfer of pollutant from a gaseous stream to the surface of a solid material that has adsorbent properties. Generally, activated carbons are employed (GAC: *Granular Activated Carbon* or PAC: *Powdered Activated Carbon*), but also silica gel, molecular sieves, polymers and activated aluminum. Abatement efficiency can reach maximum values of 95-98%: these values can obtained with engineered activated carbon system. Adsorption can be physical or chemical.
The less employed is the chemical one, due to the difficult adsorbent material regeneration.
In the physic adsorption there is an interaction between pollutant molecules and adsor-

bent material: the interaction is due to secondary electrostatic forces and it leads to pollutant trapping. Surface regeneration is very simple, due to the weak entity of the bonds. The capacity of the adsorbent material to retain the pollutant depends on various factor: pollutant boiling temperature, concentration, molecular weight, relative humidity, competitive gaseous molecules that might block the active sites. The efficiency technique depends on the regeneration capability: in the activated carbon, as a matter of example, in order to strip the pollutant several conditions need to be met: the maximum adsorption must be 10-15% by weight, the boiling temperature needs to be in the range 50-100℃, the pollutant molecular weight needs to be higher than 50 g/mol. Furthermore, the maximum relative humidity must be lower than 50%: otherwise water molecules would be adsorbed on the active sites and would saturate activated carbon.

1.4.3 Condensation

This technique involves the cooling of a gaseous steam-rich stream: the cooling leads to pollutant condensation. The condensation occurs due to the onset of electrostatic molecular forces, which in turn are originated by the lowered molecular agitation, which favors more frequent molecule contacts. The temperature at which this phenomenon occurs is the dew temperature, at even lower temperature the pollutant vapor pressure further decreases and also its vapor concentration. Employing condensation, the efficiency is more than 90%. Depending on the employed fluid used to refrigerate the polluted stream, different condensation processes can be distinguished: conventional, refrigeration, cryogenic condensation. The conventional condensation makes use of water to decrease the temperature down to 4℃, while refrigerants can work down to -18℃. The cooling occurs either via direct contact or employing a surface that allows heat transfer, keeping refrigerant fluid and the stream apart. To reach even lower temperature (-100℃) compressed refrigerant fluids are needed. By means of cryogenic condensation employing liquid nitrogen and liquid carbonic anhydride it is possible to cool down the stream at -195℃.

1.4.4 Biofiltration

This innovative method deals with the abatement of pollutant in a gaseous stream by an organic matrix (inert materials as barks, clays, polyurethanes). These materials contain microorganisms for which pollutants are nourishment. The presence of sulfur and chlorine compounds could lead to salts by-products formation. There are conventional and engineered biofilters (with high specific surface). The organic matrix is placed in bed with variable height between 0.5 and 1.5 m, needed to ensure a proper residence time (around 30 s). On the upper part of the filter, water is sprayed to keep wet the mass and to give the missing nourishment to maintain the bacteria population and regulate pH. With respect to other techniques, biofiltration have some criticalities: a longer residence time is needed to ensure good pollutant abatement; furthermore the inlet stream does not have to contain harmful compounds for microorganisms. Employing this technique, the manpower is not demanding: a bed mixing is needed once a year, performed by a robotic arm. Biofilters have several advantages, since they can work at ambient temperature, they can treat different streams and flowrates, they are cheap and they do not need chemicals.

1.4.5 Heterogeneous photocatalysis

Photocatalysis is based on the capability of the photocatalyst to adsorb simultaneously both reactants and to absorb efficient photons. It is part part on the new *Advanced Oxidation Processes*, (AOPs). It is defined as the "acceleration of photoreaction in the presence of a catalyst" (*Ibhadon A. O., Fitzpatrick P.*, 2013). Photocatalysis is discovered by Fujishima and Honda in 1972 in the photochemical splitting of water into hydrogen and oxygen in the presence of TiO_2. From that time, photocatalysis has attracted growing interest in the fields of removal of organic and inorganic species from aqueous or gas-phase systems in environmental clean-up. As for classical heterogeneous photocatalysis, the overall processes can be divided into different steps:

1. Transfer of the reactants in the fluid phase to the surface
2. Adsorption of at least one of the reactants
3. Reaction in the adsorbed phase

4. Desorption of the products

5. Removal of the products from the interface region

The reaction that occurs at step number 3, with respect to conventional catalysis has a different mode of activation of the catalyst: thermal, in this case is replaced by a photonic activation.
Heterogeneous photocatalysis has different advantages (they are reported in Section 2.2). One important feature of photocatalysis, contrary to all other techniques (biofiltration, condensation, adsorption) is the total destruction of the pollutant. In the other techniques, the pollutant is simply transferred from one phase to another, which needs further purification steps. In liquid-phase it brings an important advantage, since no sludge requiring landfill disposal is produced. Photocatalysis seems to be an efficient method to remove VOCs: the article of *Wang et al*, (2007) review a list of photocatalytic oxidation reactions of different compounds (benzene, formaldehyde, acetone, acetaldehyde, xylenes, and so on) at different operating conditions: inlet concentration, relative humidity (RH), presence of other pollutants in the vapor stream.
In the majority of cases, photocatalysis is activated by UV-radiation, since most employed catalysts absorb in that portion of electromagnetic spectrum. UV in natural sunlight represents only 5-8% of the solar spectrum at sea level. This fact is a big limitation in employing natural sunlight: hence artificial illumination is needed.
However, TiO_2 doped with transition metal ions such as Ag, Au, Fe, Ru has an absorption band red-shifted into the visible region. Employing natural sunlight would be a great simplification of the process, would lead to cost savings and would facilitate the application of photocatalysis on industrial scale. On the other hand, however, the effect of these metal ion doped catalysts on environment and on human health need to be assessed. Therefore the need for more stable, efficient catalysts, activated by the natural sunlight is the goal of researchers nowadays.

References

Brown S. K., Sim M. R., Abramson M. J., Gray C. N., (1994) "Concentrations of volatile organic-compounds in indoor air - a review". *Indoor Air Int J Indoor Air Qual Clim*, **4**:123-34.

Cheng M., Brown S. K. (2003), "VOCs identified in Australian indoor air and product emission environments", *Proceedings of National Clean Air Conference*, 23-27.

Jones A. P., (1999), "Indoor air quality and health", *Atmospheric Environment*, **33** (28): 4535-4564.

Klepeis, N.E., Nelson, W.C., Ott, W. R. et al, (2001), "National Human Activity Pattern Survey (NHAPS), Resource for Assessing Exposure to Environmental Pollutants", *Journal of Exposure Science & Environmental Epidemiology* **11**: 231-252.

Namiesnik J., Gorecki T., Kozdronzabiegala B, Lukasiak J., (1992), "Indoor air-quality (IAQ), pollutants, their sources and concentration levels". *Build Environment* **27**: 339-356.

Wang S., Ang H. M., Tade O. M. (2007), "Volatile Organic Compounds in Indoor Environment and Photocatalytic Oxidation: State of the Art", *Environmental International*, **33**, 694-705.

World Health Organization, (1989), *Indoor air quality: organic pollutants Report on a WHO Meeting*, Berlin, 23-27 August 1987. EURO Reports and Studies 111. Copenhagen, World Health Organization Regional Office for Europe.

http://www.npi.gov.au, National Pollutant Inventory, Australian Government, Department of the Environment and Energy.

https://www.epa.gov, United States Environmental Protection Agency.

Chapter 2

Photocatalysis

Heterogeneous photocatalysis is introduced in Chapter 1: in this Chapter it is deeply described, then PCO (*Photo Catalytic Oxidation*) processes are taken into account. The catalysts used in this work are then introduced and the reaction mechanism of methanol oxidation is illustrated. At the end, the kinetic model is briefly treated.

2.1 Theoretical principles

Heterogeneous photocatalysis on semiconductor is a well known technology. It has been studied for several decades in different fields: pollution abatement, chemical synthesis, energy innovation. It has attracted a great attention for pollutants abatement, especially when they are present at a very low concentration, due to the mild experimental condition, the non-selectivity towards different contaminants and the non-toxicity of the final products obtained.

Heterogenous photocatalysis occurs between the reactants (which, in this work are in vapor phase) and the catalyst, which is in the solid state. The reaction needs to be activated by electromagnetic radiation, which comes from an external energy source.

Semiconductor, indeed, is formed by an electronic band structure: the most energetic occupied band is the *Valence Band* (VB), the least energetic non-occupied is the *Conductive Band* (CB). In between there is an electron-forbidden energy band gap. Whenever a photon, that has an energy at least equal to the band gap, is adsorbed by a semiconductor atom, an electron of the VB has enough energy to be ”promoted” to the CB, leading to the formation of a ”hole” (h^+) in the VB.

At that point two different situations could happen: in the first case, the "promoted" electron in the conductive band (e^-_{cb}) recombines with the hole present in the valence band (h^+_{vb}): the recombination occurs on the surface or in the particle bulk with energy dissipation.
In the other case e^-_{cb} and h^+_{vb} are trapped in surface state: electron reacts with an acceptor species absorbed or close to the surface of the particle, while the hole reacts with a donor species. In this way, subsequent anodic and cathodic redox reaction can occur.
Unlike metals, semiconductors lack a continuum of interband states (it would otherwise promote the recombination of electron-hole pairs): in this way, there is a sufficiently long lifetime of electron-holes pair to diffuse to the catalyst's surface and initiate a redox reaction.
The energy level at the bottom of the CB is known as the reduction potential of photoelectrons, whereas the energy level at the top of the VB is the oxidizing ability of photoholes. The flat-band potential V_{fb} is the energy of both charge carriers at the semiconductor-electrolyte interface. Absorbed couples can be reduced photocatalytically by electrons in the CB if they have redox potential more positive than the flat band potential of the CB and they can be oxidized by holes in the VB if they have redox potential more negative than the flat band of the VB. (*Carp O. et al.*, 2004).
The efficiency of a photocatalyst depends on the competition of different processes and electrons and holes deactivation by recombination. The true ossidative pathway is subject of scientific discussion, since the oxidation can occur by direct hole attack or mediated by HO• radicals.
To compute the wavelength associated to the electromagnetic energy needed to "promote" electron from the top of the VB to the bottom of the CB, Eq. 2.1 can be used, recalling the Planck equation ($E = h\nu$) and the equation: $c = \lambda\nu$:

$$\lambda = \frac{hc}{E} \tag{2.1}$$

Where c is the light speed in vacuum (3×10^8 m/s), λ is the radiation wavelength, ν is the radiation frequency and h is the Planck constant (6.626 $\times 10^{-34} m^2\ kg\ s^{-1}$).

The phenomena are depicted in Figure 2.1b. The photon energy is represented according to the Planck equation: $E = h\nu$, the acceptor species is A, while the donor is D.

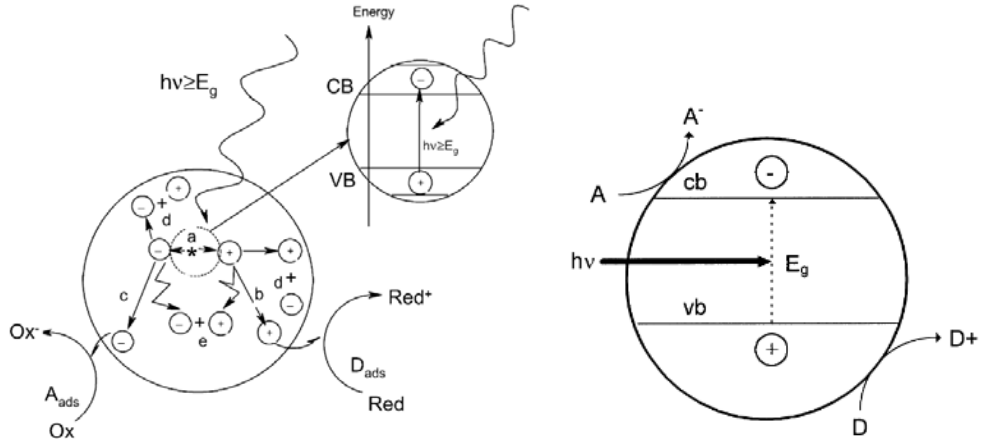

(a) *Reaction occurring on a semiconductor particle.* **(b)** *Particular of the illuminated semiconductor particle.*

Figure 2.1: Diagram of the heterogenous photocatalysis occurring on an illuminated semiconductor particle (*Carp et al*, 2004)

Species A is reduced to A^-, while species D is oxidized to D^+. The forbidden band gap is labeled as E_g, while vb and cb are respectively the valence and the conductive bands.

2.2 Photocatalytic oxidation

Between photocatalytic reactions, *Photo Catalytic Oxidation* (PCO) processes of volatile organic compound play an important role. The reactions involving electron and holes must compete effectively with the main deactivating process (electron-hole recombination) that may occur in the bulk or at the surface. Holes mediates the pollutant oxidation, through hydroxyl radical formation. Hydroxyl radicals ($HO\bullet$) are highly reactive species and short-living. On the other side, electrons are responsible of redox reaction through the formation of superoxide radicals ($O_2^-\bullet$).

Figure 2.1a summarizes the catalytic reactions occurring on a semiconductor particle. (a) represents the hole-electron pairs formation, (b) is the oxidation of the donor (D_{ads}) adsorbed on the surface, (c) is the reduction of the acceptor species adsorbed on the surface (A_{ads}), while (d) and (e) are recombination between holes and electrons that occur respectively on the semiconductor surface and on its bulk.

PCO in the field of pollutant removal have some advantages:

1. The reaction can run at mild conditions, even at room temperature and atmospheric pressure. The activation energy is provided by a light-source. Thermal oxidations

require, generally, much higher temperature;

2. PCO catalysts are active toward various contaminants: it is said that they are not selective with the respect to a specific pollutant. Also, they can mineralize most organic compounds effectively;

3. PCO final products are benign (CO_2 and H_2O), or at least less harmful than the initial pollutant;

4. Unlike the other techniques described in Section 1.4 (adsorption, condensation, biofiltration), PCO does not deal with a pollutant transfer from one phase to another one. Like incineration it deals with the total destruction of the contaminant: however, the operative conditions in photocatalysis are much softer;

5. The need of catalyst/material regeneration is generally limited;

6. There are no additive or additional chemicals required (only oxygen from the air);

7. PCO can work at very low pollutant concentration (ppm and ppb levels): for example, thermal catalytic oxidation is not economically feasible at low pollutant concentrations;

8. PCO is more cost-effective than conventional techniques: for example, activated carbon are more expensive than semiconductors.

The photocatalyst need to absorb photon and simultaneously adsorb reactants: materials that can perform PCO processes are: ZnO, ZnS, ZrO_2, CdS, Fe_2O_3 WO_3, CeO_2 and SnO_2. However, the most popular and utilized catalyst is TiO_2: its main features are described in Section 2.4. In Fig. 2.2 there are the band threshold of different semiconductors: for each material, the top of the valence band and the bottom of the conductive band are reported. On this picture, the two crystalline forms of titania are reported: namely TiO_2-A stands for anatase, while TiO_2-R stands for rutile. The gray lines are related to the reduction potential needed to perform the oxidation of organics.

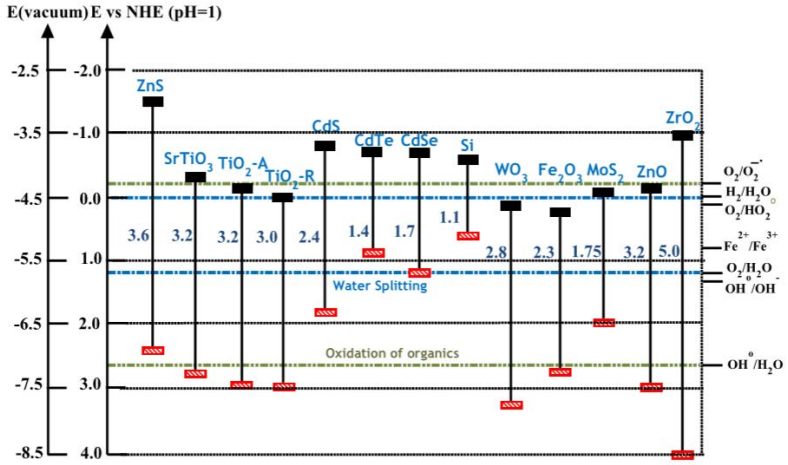

Figure 2.2: Band position: top of valence band and bottom of conduction band of different semiconductors (*Vinu et al.*, 2010).

2.3 Reaction parameters

PCO processes are affected by many physical-chemical parameters, related both to the catalyst, and to process conditions. The effect of some parameters are represented in visual representation in Figure 2.3. The work of A. H. Mamagani (*Mamagani A. H. et al*, 2017) links catalyst properties and process conditions to catalyst activity towards VOC:

2.3.1 Photocatalyst characterization

Photocatalytic activity depends on several factors related to the catalyst such as crystallinity, crystalline phase, crystal size, accessible surface area, pore structure, pore size, and adsorption capacity.

1. Photocatalyst crystallinity and crystal size: electron-hole recombination process is facilitated by the presence of lattice defects, impurities, imperfections. So, during catalyst synthesis is important to obtain a high bulk crystallinity. Furthermore, small crystal size and, in the case of TiO_2 the co-presence of anatase and rutile phases leads to higher reaction rates.

2. Surface area: as the surface area increases, greater number of active sites and electron-hole pairs forms. Furthermore, the presence of microporosity can retard the escape of pollutants from the surface (and so increasing the residence time) and increase the probability of reactants adsorption and reaction on the surface. Interconnected pore system can favor the diffusion of reactants. Furthermore, heat

treatment, while improves the crystallinity, on the other hand, adversely affects the surface area and porous structure.

3. Catalyst surface density: in the majority of studies, increasing the photocatalyst loading has improved VOC abatement, while in some cases excessive catalyst usage has led to conversion decrements. For high catalyst quantity, a screening effect can occurs, which masks part of the photocatalytic surface. For that reason, the catalyst content optimum needs to be found to avoid excess of catalyst and to ensure a total absorption of photons. Figure 2.3(a) shows the linear increase of reaction rate (r) with respect to catalyst mass, up to a plateau: increasing further the mass of the catalyst does not lead to any further rate increase. The optimum catalyst concentration is labeled as m_{opt}.

4. Photocatalyst adsorption properties: the adsorption features depend on the very structure of the pollutant and of the catalyst.

5. Catalyst support: in order to immobilize the catalyst and to maximize the exposure to light irradiance and air stream, a support material is used. The support should have: high surface area, high transparency, porous structure, high adsorptive affinity towards VOCs and stability under UV irradiation.

2.3.2 Operating parameters

The catalyst activity is function of process operating parameter: the main are:

1. Air flowrate and residence time: air flowrate has a dual effect on photocatalytic reaction. The first is that, as the flowrate increases, the reactor residence time decrease: it leads to a smaller pollutant adsorption and a lowered conversion. The second effect is that, as the flowrate increases, the mass transfer coefficient between the air and the photocatalyst surface increases. However, taking into account air flowrate applied in conditioning system, it is possible to rule out the contribution of the mass transfer and it is possible to claim that higher flow rates decrease VOCs' conversion.

2. Pollutant concentration: increasing VOC inlet concentration is responsible of improved reaction kinetics, lower removal efficiency and poorer mineralization of

pollutants to carbonic anhydride. The number of pollutant molecules that can be adsorbed increases, and boosts the reaction kinetics, at the same time the ratio active species to pollutant molecules decreases and so more VOC can leave the reactor without reacting. Furthermore, higher amount of by-products are formed. The reaction is faster as the initial concentration increases: Figure 2.3(c) reports qualitatively this behavior.

3. Relative humidity (RH): water vapor can have two effects:

   (a) Adsorbed water molecules are oxidized to hydroxyl radicals, that can improve the reaction, furthermore humidity supplies hydroxyl groups, maintaining the oxidation rate and can trap holes avoiding electron/hole recombination.

   (b) On the other side, water molecules adsorbed on the catalyst surface can form a film that hinders pollutant adsorption; also, water molecules can compete on active sites with contaminants and, at very high RH, water vapor can decrease the UV light intensity, blocking its radiation.

   However, it has been found that methanol (hydrophilic molecule), unlike benzene (hydrophobic molecule) adsorption efficiency increases with increasing RH up to 35%. Methanol is soluble in water; indeed, methanol molecules can penetrate through water layers and be adsorbed on the catalyst surface.

4. Light intensity: increasing light intensity enhances the removal efficiency and reaction rate. The behavior is reported in Figure 2.3(d): on y-axis there is the reaction rate, while on x-axis there is the radiation flux (Φ). At low Φ, reaction rate follows a linear dependence ($R \propto \Phi$), while at higher flux, the radiation follow a root dependence ($R \propto \Phi^{1/2}$).

5. Temperature: Photocatalytic systems do not require heating or thermal activation, and can be operated at room temperature

Furthermore in Figure 2.3(b) shows that for a radiation that has energy $E \geqslant E_g$, (where E_g is the energy band gap), the reaction rate is non affected of the radiation wavelength, while as $E \leqslant E_g$, reaction rate drops dramatically.

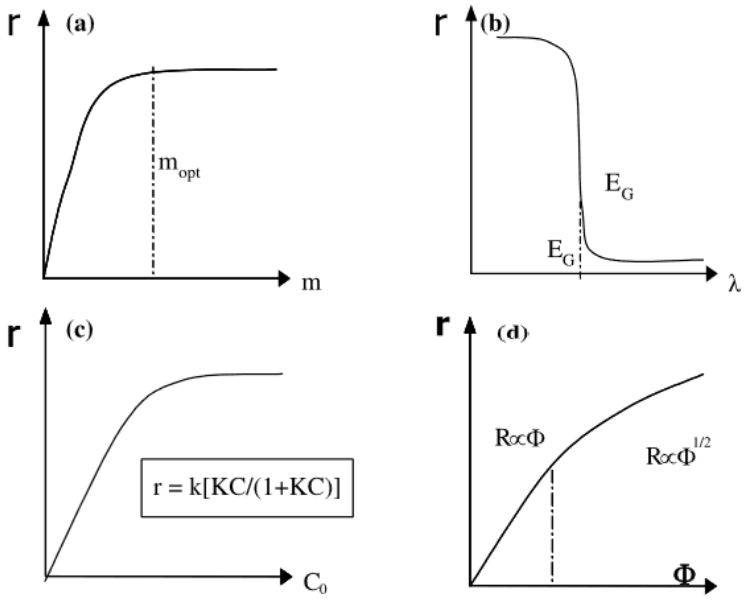

Figure 2.3: Reaction rate dependences (r) with respect to (a) catalyst concentration (b) light wavelength (c) pollutant initial concentration (d) the inverse of temperature (e) lamp radiant flux

2.4 Titanium dioxide

Titanium dioxide belongs to the family of transition metal oxides: it's major use is as white pigment in paints where it has replaced toxic lead oxides. Other uses are in plastic, paper, but also textile, food, leather, pharmaceuticals fields. It's worth to cite that due to its hemocompatibility with the human body, it is used as a biomaterial (as bone substituent and reinforcing mechanical supports).

Among all other types of catalyst, TiO_2 has received great attention and investigation for photo-catalysis oxidation (PCO) reactions. This semiconductor oxide, indeed, is so far the most promising catalyst because of to its exceptional chemical stability, non-toxicity, low cost (1.6 Euro/kg), optical and electronic properties, biologically inertia, phototactically activity, ease to produce and to use, efficiently activation by the sunlight, stability, low cost, without risk for the environment or humans. Titanium dioxide is close to being an ideal photocatalyst, having almost all the abovementioned properties. To date, several TiO_2 photocatalysts with different morphological structure have been employed: nanoparticles, nanotubes, hollow fibers, and mesoporous. This catalyst have just few disadvantages: it has high recombination rate of electrons/holes pairs, small adsorption capacity of the contaminants and poor visible-light exploitation.

In nature there are four polymorphs: anatase (tetragonal), brookite (orthorhombic), rutile (tetragonal) and TiO_2 monoclinic. The structures of rutile, anatase and brookite are arranged in terms of octahedrals. Anatase, as can be inferred from Fig. 2.4 can be seen as octahedrals connected by their vertices, while in rutile the edges are connected: in brookite, both vertices and edges are connected.

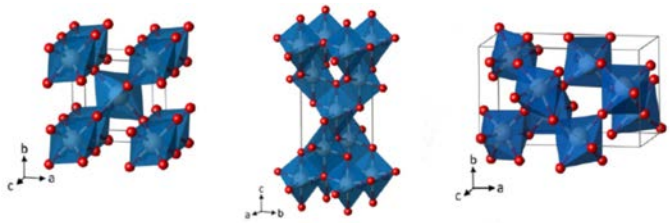

Figure 2.4: Crystal structure of rutile (left), anatase (center), brookite (right)

Anathase is most thermodynamically stable at sizes less than 11 nm, brookite is most stable between 11 and 35 nm, while rutile is most stable at sizes greater than 35 nm.

From a photocatalytic standpoint, the energy bandgap (E_g) are:

1. anatase: E_g=3.23 eV[1], λ=384 nm
2. rutile E_g=3.02 eV, λ=411 nm

The wavelength associated with the energy band gaps of anatase and rutile are calculated according to Equation 2.1. Band gap is the minimum energy that promotes hole-electron pairs formation, while the wavelength is the threshold value of the radiating source. So, it can be inferred that in order to activate the reaction UV source must be used.
UV (*Ultra-Violet*) radiation, indeed, is characterized by a wavelength range between 400-100 nm, which correspond respectively to photonic energy between 3.10-12.4 eV. Three classes can be distinguished:

1. UV-A: $\lambda = 400 - 315$ nm, E=3.10-3.94 eV;
2. UV-B: $\lambda = 315 - 280$ nm, E=3.94-4.43 eV;
3. UV-C: $\lambda = 280 - 100$ nm, E=4.43-12.4 eV;

Anatase is found to be more photocatalytically active than rutile, due to several properties of anatase phase: 1) better generation of electron-hole pairs; 2) higher affinity towards O_2

[1] 1eV=$1.602 \times 10^{-19} J$

due to the more negative redox potential of conduction band; 3) higher amount of surface hydroxyl group; 4) lower recombination rate than rutile. The company Degussa produces a commercial form of TiO_2 known as P25: it is formed by 80% of anatase and 20% of rutile, with an overall excellent activity. It has been suggested that in P25, because of the co-presence of anatase and rutile, electrons and holes can transfer between interconnecting particles and prevent electron/hole recombination. Bickely et al suggested, indeed, that the high activity for P25 is due to the presence of particles made of anatase nuclei inside a rutile layer: that makes the charges lifetime longer (electron in anatase and hole in rutile). For what catalytic activity concerns, the BET surface of P25 is: $47\,\mathrm{m}^2/\mathrm{g}$.

2.5 Cerium dioxide

Cerium dioxide (CeO_2, known also as "Ceria"), part of the Lanthanides Oxide group, in recent years, has gained increasing attention, in addition to TiO_2, doped with metals or coupled with other material, as new catalyst. It possesses different advantages: it is not toxic, it is very stable in the reaction medium, it has good electronic and optical properties, thanks to its 4f electrons. Furthermore, CeO_2 has a longer charge carriers lifetime if compared to TiO_2 but, similarly to titanium oxide has a wide bandgap (3-3.4 eV), and for that reason, its application under visible or solar light is limited, since it requires the activation by UV light (*Bellardita M et al.*, 2019). Different studies are found in scientific literature on the employment of cerium dioxide as photocatalyst. Gaseous toluene is mineralized with CeO_2 without catalysts deactivation, however its reaction rate is one order of magnitude lower than in presence of TiO_2 (*Coronado et al.*, 2002).
An important parameter determining the photocatalytic activity is the presence of oxygen vacancies in the lattice of CeO_2. They are responsible for the creation of isolated levels below the CB, which favors absorption of visible light. CeO_2 with vacancies exhibits good activity under visible light irradiation for organic photodegradation.

2.5.1 CeO_2-TiO_2 composites

One of the most exploited technique is to synthetize TiO_2 composites, in order to obtain efficient material for photocatalytic applications. Theoretically, the combination of two different metal oxide could have a synergetic effect because the electronic properties of

the mixed material is different with respect to the single ones. Coupling these two oxides that have different CB and VB could lead to a better separation of charges: consequently, the recombination will become more difficult and the charges would be more prone to react with surface-adsorbed species, leading to an increase of the reaction rate. Between other oxides, ZnO is the most studied photocatalyst after TiO_2: it absorbs a higher fraction of the solar spectrum and the quantum efficiency is higher than that of TiO_2. The study of Munoz-Batista et al. showed that toluene is oxidized employing UV radiation, employing a CeO_2-TiO_2 composite: they were able to prove the synergistic effect between the two oxides. The maximum activity is found with samples that have low CeO_2 loading (between 5%, on molar basis). The same authors have studied acetaldehyde abatement, both under UV and visible-light irradiation. The composite catalyst outperforms the titanium oxide activity by a factor bigger than 2. These results suggest the potential of the composite material toward the degradation of VOCs.

2.5.2 Graphene

Graphene is a 2D monolayer of carbon atoms ibridized sp^2, packed in a hexagonal structured, was discovered in 2004. It possesses very interesting properties: high thermal conductivity, superior mechanical strength, high specific surface area and excellent charge transport. Graphene and its derivative (GO and rGO graphene oxide and reduced graphene oxide) can bring some positive effects on the photocatalytic performances of catalysts. Graphene, indeed, creates synergy between the semiconductor and the carbon phase. The band gap energy is therefore lower and the adsorptive properties are enhanced. For that reason is incorporated into many different semiconductor to produce graphene-based composites. Liu (*Liu et al.*, 2010) suggests that the electrons possess a large mobility in the graphene layers. For that reason, electrons can react with atmospheric molecular oxygen adsorbed on the membrane to yield hydroxyl radicals: these species are then responsible of methanol oxidation. Figure 2.5 is a schematic representation of a graphene monolayer and the charge transfer.

Electron transfer, furthermore, prevents electron-hole recombination: for that reason the hole on the VB does not undergo to recombination and therefore is responsible of hydroxyl radicals formation. For these reason, graphene enhances the photocatalytic performances of semiconductors.

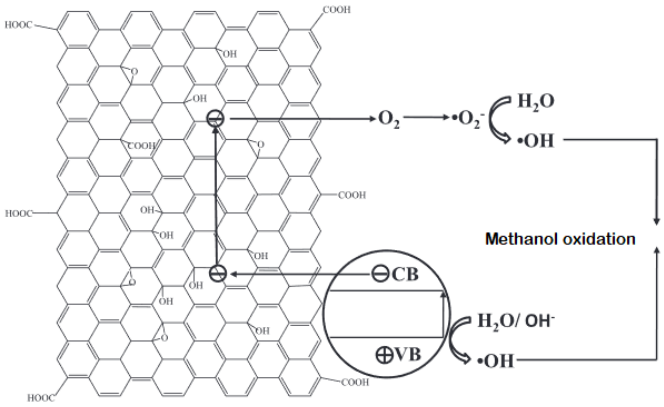

Figure 2.5: Schematic representation of electron transfer on a graphene layer, adapted from *Liu J*, 2010

2.5.3 Mechano-chemical synthesis

In order to make the contact between titanium oxide and cerium dioxide more intimate, mechano-chemical synthesis is exploited. This synthesis method has received in the last years a lot of interest for processing powders, especially when it is employed to synthetize a wide range of ultra-fine materials and solid nanocrystalline materials, in particular oxides. It is a processing technique in which mechanical and chemical phenomena are coupled on the molecular scale. The wanted product can be produced only employing mechanical action (high pressure and mechanical stress between balls and reactants). During the grinding, the chemical precursors undergo a reaction that allows the synthesis of the desired material. The synthesis route is therefore simple and versatile, relatively fast and it does not use any chemical solvent. This method exploits the bonds breaking between atoms and molecules, obtained by the applied mechanical energy to produce the desired material. The stress produced by high mechano-chemical synthesis leads to the onset of further deformation of the bond, surface and bulk defects, irregularities that can improve some features of the material (for example oxygen mobility).Mechano-chemical synthesis can be performed under different conditions: for example using a reactive atmosphere (reactive ball milling), under cryogenic conditions (cryomilling). Different parameters can influence the characteristics of the final material: milling time, temperature, frequency, atmosphere, gas pressure, powder to ball weight ratio. Different products can therefore be obtained: metastable, high-pressure, amorphous, disordered phases. Nevertheless, two intrinsic disadvantages are: the structurally amorphous product that is obtained and the formation of undesired products as a result of competing reactions. The

milling process has different advantages: easy production, reduction of reaction times, low contamination, high yields and minimum solvent or waste. Furthermore, the synthesis occurs at room temperature or a temperature lower than traditional solid-state synthesis. Therefore, it is considered an eco-friendly process with commercial and industrial potential.

The milling of ceria with carbon soot leads to the formation of a CeO_2 core wrapped in a soft carbon shell; the different hardness of the two materials helps the spreading of the softer carbon particles on the surface of ceria. The continuous bond rupture/formation typical of high-energy milling and the shear and friction forces favor an intimate ceria-carbon contact. It can promote the modification of the shape of the solid solution and the exposure of more active surface that can promote photocatalytic reaction. The proper arrangement at nanoscale increases by two order of magnitude the soot oxidation rate. This method leads to the development of ultrafine-grained and nanostructured compounds with homogeneous composition. It is therefore a versatile technique that can be used to prepare a wide range of materials.

2.6 UV photocatalysis

This paragraph concerns with the reaction mechanism that occurs on semiconductor, in this case (TiO_2) active area. The complete reaction mechanism is proposed by Vinu R., G. Madras (2010): Charge carrier generation:

$$TiO_2 + h\nu \rightarrow h^+_{vb} + e^-_{cb} \tag{2.2}$$

Charge carrier trapping:

$$Ti^{IV} - OH^- + h^+_{vb} \rightarrow Ti^{IV} - OH\bullet \tag{2.3}$$

Surface trap:

$$Ti^{IV} - OH^- + e^-_{cb} \rightarrow Ti^{III} - OH^- \tag{2.4}$$

Deep trap:

$$Ti^{IV} + e^-_{cb} \rightarrow Ti^{III} \tag{2.5}$$

Electron-hole recombination:

Free electron with a trapped hole:

$$Ti^{IV} - OH\bullet + e^-_{cb} \rightarrow Ti^{IV} - OH^- \tag{2.6}$$

Free hole with a trapped electron

$$Ti^{III} + h^+_{vb} \rightarrow Ti^{IV} \tag{2.7}$$

Free hole with a free electron:

$$h^+_{vb} + e^-_{cb} \rightarrow heat \tag{2.8}$$

Generation of hydroxyl radicals in the aqueous medium:

Hole pathway:

$$Ti^{IV} - H_2O + h^+_{vb} \rightarrow Ti^{IV} - OH\bullet + H^+ \tag{2.9}$$

Electron pathway:

$$Ti^{III} + O_2 \rightarrow Ti^{III} - O^-_2\bullet \tag{2.10}$$

$$Ti^{IV} - O^-_2\bullet + 2H^+ + e^-_{cb} \rightarrow Ti^{IV} - H_2O_2 \tag{2.11}$$

$$Ti^{IV} - O^-_2\bullet + H^+ \rightarrow Ti^{IV} - HO_2\bullet \tag{2.12}$$

$$Ti^{IV} - 2HO_2\bullet \rightarrow Ti^{IV} - H_2O_2 + O_2 \tag{2.13}$$

$$Ti^{IV} - H_2O_2 + e^-_{cb} \rightarrow Ti^{IV} - OH\bullet + OH^- \tag{2.14}$$

$$Ti^{IV} - H_2O_2 + O^-_2\bullet \rightarrow Ti^{IV} - OH\bullet + OH^- + O_2 \tag{2.15}$$

Adsorption/desorption of reductant (any organic substrate S)

$$Ti^{IV} + S \rightarrow Ti^{IV} - S \tag{2.16}$$

$$Ti^{IV} - OH\bullet + S \rightarrow Ti^{IV} - OH\bullet - S \tag{2.17}$$

Adsorption/desorption of oxidant (metallic ion):

$$Ti^{IV} + M^{n+} \rightarrow Ti^{IV} - M^{n+} \tag{2.18}$$

Photo-oxidation of reductant:

Direct attack of the hole:

$$Ti^{IV} - S + Ti^{IV}(h^{+}_{vb}) \rightarrow Ti^{IV} + Ti^{IV} - I \rightarrow CO_2 + H_2O \tag{2.19}$$

Hydroxyl radical attack:

$$Ti^{IV} - S + Ti^{IV} - OH\bullet \rightarrow Ti^{IV} + Ti^{IV} - I \rightarrow CO_2 + H_2O \tag{2.20}$$

$$Ti^{IV} - S + OH\bullet \rightarrow Ti^{IV} - I \rightarrow CO_2 + H_2O \tag{2.21}$$

$$Ti^{IV} - OH\bullet - S \rightarrow Ti^{IV} - I \rightarrow CO_2 + H_2O \tag{2.22}$$

Adsorption/desorption of organic intermediate

$$Ti^{IV} + I \rightarrow Ti^{IV} - I \tag{2.23}$$

Photoreduction of metallic ion

$$Ti^{IV} - M^{n+} + me^{-} \rightarrow Ti^{IV} - M^{(n-m)+} \tag{2.24}$$

In the reaction reported, Ti^{IV} denotes the four functionality of titanium oxide. The characteristic time-scale for the generation of charge-carriers is of order of femto-seconds. The charges can get trapped on the catalyst surface. Reaction (2.3) is the holes trapping by the surface hydroxyl groups present in TiO_2. Reactions (2.4-2.5) are the reversible trapping of electrons in the surface, and the irreversible trapping of electrons to the bottom of the CB (deep trap). Reactions (2.6-2.8) are the electron-holes recombination reactions, which occurs at the surface, or in the bulk medium due to the delocalization of the electrons and holes. This reaction affects the interfacial charge transfer and lower the quantum efficiency of the process. Reaction (2.9) represent the hydroxyl radicals formation: surface adsorbed molecules react with the holes. Reaction (2.10-2.14) are the formation of superoxide, hydroperoxide and hydroxyl species, by the electron pathway. When the reactions are carried out in non-aqueous organic medium, the surface bound hydroxyl species present in the semiconductor plays a major role.

As soon as the active species are generated, the reactants are adsorbed onto the surface of the catalyst, (reactions (2.16-2.18)). Then, the reductant is oxidized, the oxidant is reduced by the attack of the hydroxyl radicals and CB electrons, (reactions (2.19-2.22). These interfacial electron transfer steps compete with electron-hole recombination: the practical efficiency is always lower than the theoretical one. The organic compound degrades by the formation of intermediate (I), which are eventually oxidized to CO_2 and H_2O. Reaction (2.23) represents the desorption of the products from the surface, leaving the active site free. When metal ions are present in the system, they are reduced to their stable oxidation state by CB electrons (reaction 2.24). Therefore, the overall photocatalytic reaction mechanism can be depicted as:

$$(Ox_1)_{ads} + (Red_2)_{ads} \rightarrow (Red_1)_{ads} + (Ox_2)_{ads} \tag{2.25}$$

2.7 Methanol photocatalysis

The mechanism of methanol oxidation in gas phase on titanium dioxide is here reported. Methanol can be oxidized by reaction of direct and indirect hole transfer. The species that take part in the reactions are different: holes, hydroxyl radicals and superoxide radicals (*Modesti et al.*, 2013). The $HO\bullet$ and $HO_2\bullet$ radicals from the h+ attack and the $O_2^-\bullet$ superoxide radical anions, obtained from O_2 reduction by electron are very reactive species: they can oxidize the organic pollutant completely to CO_2 and H_2O or to less harmful compounds. Each oxidation step occur on the surface by interaction of the adsorbed species with the holes of the VB or through an indirect path, by means of hydroxyl radicals attack.

$$TiO_2 + h\nu \rightarrow h^+_{vb} + e^-_{cb} \tag{2.26}$$

$$CH_3OH_{ads} + h^+_{vb} \rightarrow \bullet CH_2OH_{ads} + H^+ \tag{2.27}$$

$$\bullet CH_2OH_{ads} \rightarrow CH_2O + H^+ + e^- \tag{2.28}$$

$$\bullet CH_2O_g + 2O_a \rightarrow \bullet CHO_g + HO_2\bullet \tag{2.29}$$

$$\bullet CHO_g + 2O_a \rightarrow CO_g + HO_2\bullet \tag{2.30}$$

$$\bullet CO + HO_2\bullet \rightarrow CO_2 + HO_2\bullet \tag{2.31}$$

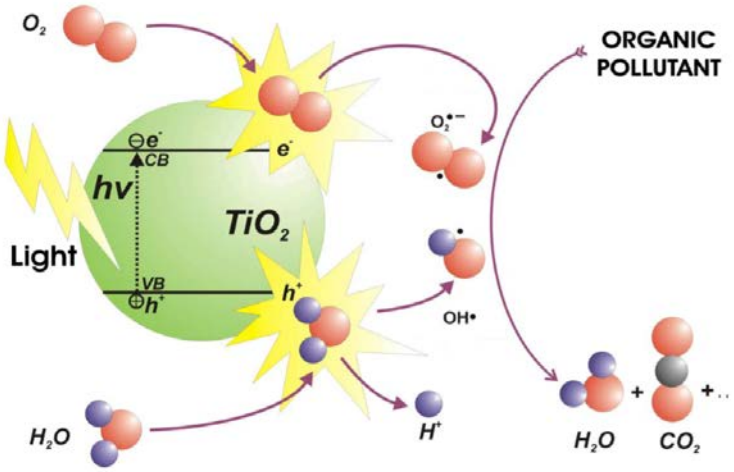

Figure 2.6: Oxidation of organic pollutant on an illuminated titania particle

$$H_2O + h_{vb}^+ \rightarrow \bullet OH + H^+ \tag{2.32}$$

$$CH_3OH + \bullet OH \rightarrow \bullet CH_2OH + H_2O \tag{2.33}$$

$$\bullet CH_2OH + \bullet OH \rightarrow CH_2O + H_2 \tag{2.34}$$

$$CH_2O + 2O_a \rightarrow CO_2 + H_2O \tag{2.35}$$

Methanol oxidation has an intermediate step of formation of formaldehyde, which is then completely oxidized to water and carbon dioxide. The formation of a by product (methyl formate) is also observed. Yeomet et al., Lichtenbergeret et al., in their works claim that this by-product is produced through the reaction between the two radicals HCO and CH_3O and the hydrogen transfer followed by formaldehyde dimerization. Methyl formate can be formed by the esterification of formic acid (which is produced by oxidation of formaldehyde) and methanol (*Modesti et al.*, 2013). Another reaction mechanism is proposed, in which condensation of methoxides with formaldehyde occurs: it yields hemiacetals intermediate which are then dehydrogenated to methyl formate. The general scheme of photo-oxidation of a organic compound is reported in Fig. 2.6. The titania particle is activated by radiation source, molecular oxygen is reduced to superoxide radicals, while water is oxidize to yield hydroxyl radicals. They are responsible for the complete mineralization of the organic pollutant.

2.8 Kinetics

In photocatalytic systems, kinetic is modeled according to Langmuir-Hinshelwood isotherm:

$$r_p = k_0 \frac{K_c C_P}{1 + K_c C_P K_w C_w} \tag{2.36}$$

where r_p is the rate of pollutant degradation coefficient, k_0 is the rate constant, K_c and K_w are the Langmuir adsorption equilibrium constants, C_p and C_w are the pollutant and vapor gaseous concentrations. This model is useful since it considers two different phenomena: chemical reaction and physical sorption. It's important to note that in this equation both methanol (pollutant) and water vapor undergo to adsorption on the active site of the catalyst.

2.9 References

Hermann J. M., (1999), "Heterogeneous photocatalysis: fundamentals and applications to the removal of various types of aqueous pollutants", *Catalysis Today* **53**: 115-129.

Ibhadon, A., Fitzpatrick, P., (2013). "Heterogeneous Photocatalysis: Recent Advances and Applications". *Catalysts*, **3**, 189-218.

Liu J., Bai H. (2010), "Self-Assembling TiO_2 Nanorods on Large Graphene Oxide Sheets at a Two-Phase Interface and Their Anti-Recombination in Photocatalytic Applications", *Advanced Functional Materials*, **20**, 4175-4181.

Mamaghani A. H., Haghighat F., Lee C.-S. (2017), "Photocatalytic oxidation technology for indoor environment air purification: The state-of-the-art". *Applied Catalysis B: Environmental*, **203**, 247-269.

Pastrana-Martinez L. M., Torres S. M. (2018), "Graphene Photocatalysts", *Multifunctional Photocatalytic Materials for Energy*, 79-101.

Chapter 3

Nanofibers and electrospinning

In this chapter a brief outline of nanofibers, their properties, the preparation techniques and their application is presented. Particular importance is given, then to electrospinning process: mechanisms and governing parameters are described. In the end, electrospraying is briefly described.

3.1 Nanofibers

Nanofibers are part of nanotechnology, which is the science concerned with the study of the phenomena, materials, structures within the dimensional range of 0.1-100 nm. "*Nano*" in the technical language, represents, indeed, a physical quantity one billionth smaller than the unit of measurement of reference, for example 1 nm = 10^{-9} m. Sometimes, especially in the commercial sector, the term "nano" refers also to materials, structures with dimension up to 300, or even 500 nm: on the other side, academic community has agreed the $<$100 nm benchmark: higher dimension is classified as "sub-micro technology". These nanomaterials exhibit unusual and unique properties (mechanical, thermal, magnetic, electrical).
On the other side, the word "fiber" is defined from a geometrical standpoint as a "slender, elongated, threadlike object or structure". Furthermore, it must have high stretching resistance in the direction of deformation. From the molecular viewpoint, a fiber is formed by long and linear polymer chains. The stretching resistance is due to the nature of covalent bonds in the polymer chain, while the stability of the structure is due to intermolecular forces (hydrogen, dipole-dipole, Van der Waals forces) that do not allow

chain unfolding. Nanofiber is therefore defined as a 1-dimensional nano scale element (like nanotubes and nanorods), in which one dimension is much bigger than the others. A nanofiber is a nanomaterial because of its diameter, and it can be considered a nanostructured material if filled with nanoparticles to yield composite nanofibers.

3.1.1 Production techniques

Different techniques are available to process fibers: they are briefly explained in this section (*Ramakrishna et al*, 2005):

1. Template synthesis: this method deals with the use of a template or mold to produce the desired material or structure. This common technique is used to produce nanostructures (for example carbon nanotubes and nanofibers). The template is a metal oxide (for example aluminum oxide) membrane with through-thickness nanopores. The use of water pressure causes extrusion of the polymer, which by contacting with a solidifying solution, forms a nanofiber. This method has a big advantage: fibers of different diameters can be easily achieved, by using different templates.

2. Self assembly: it is a technique in which the fibers are built, employing small molecules, as basic ”building blocks”. The intermolecular forces bring the smaller units together and the shape of the smaller units affects the overall shape of the macromolecular nanofibers. It is an effective technique for obtaining smaller nanofibers, but on the other hand, it is a complex process.

3. Phase Separation: in this method a polymer is blended with a solvent, before undergoing gelation. The phase separation is due to physical incompatibility. The main steps of this process are: polymer dissolution, gelation, solvent extraction, freezing and freeze-drying. The phase that contains the solvent is extracted, leaving the other remaining phase. At the end, a polymeric porous structure is obtained, constituted by nanofibers. In this case, the main advantages are: minimum equipment required, the process can directly fabricate a nanofiber matrix and the mechanical properties of the matrix can be tailored by adjusting polymer concentration. However, this method is limited to specific polymers.

4. Drawing: this technique can be seen as dry spinning at a molecular level. It can be applied to viscoelastic materials that can experience a high degree of deformation. A micropipette, of few micrometers diameter, is immersed into a droplet next to the contact line, employing a micromanipulator. The pipette is then removed from the liquor at a controlled rate to pull a nanofiber. The fiber is dumped on the surface by touching it with the micropipette end. The nanofiber drawing is frequently repeated on every droplet. The viscosity of the material at the edge of the droplet increases, due to evaporation. The material must tolerate strong deformations, but it needs to be adequately cohesive to maintain the developed stress during pulling. The equipment needed is minimum, but the process is discontinuous.

5. Melt blown: this method is used to produce both micro and nanofibers together. Just one step is needed: the polymer melt extruded through an orifice die is blown with a high speed air flow. The polymer is deposited on a collector and a micro/nanometric fiber network is obtained. However, this technique does not induce any preferential direction to the fibers and so they do not have good mechanical properties.

6. Electrospinning: it is the technique employed in this work: it is analyzed in detail in the section 3.2. However, in the simplest form it consists on: a syringe that contains the polymer solution, two electrodes and a voltage supply. A jet of polymer solution is ejected from the tip of a needle under electrostatic forces action: the jet, indeed, is electrically charged: the fibers are collected on a grounded target. This method is cost effective. Furthermore, long continuous nanofibers can be easily produced. However, the polymer jet is affected by instability.

3.2 Electrospinning

The phenomenon of electric-field induced charges within a liquid was first observed in 1600. Water behavior under the influence of electrostatic potential was studied by Gray in the 1730s. In the late 1800s, electrodynamics was used to explain the excitation of dielectric liquid when subjected to an electric potential (Larmor, 1898). At the beginning of the 20^{th} century, a huge interest arose in highly porous meshes in the textile, filtration

industries and in the military sector. This led to the invention of the electrospinning to produce fibers in the early 1900s by Cooley and Morton (Cooley 1902, Morton 1902). Cooley invented an electrospinning setup which employed auxiliary electrodes to force the polymer jet onto a rotating drum. In the 1930s, Formhals studied different innovative set-ups to produce yarns, including designs that do not require the use of a spinneret. In fact, many electrospinning set-ups are dated to more than half-century ago (multiple spinneret, parallel electrodes to produce aligned fibers, Formhals 1938, 1939).
Nevertheless, the majority of the studies are stopped due to the low production rates that do not allow an industry level scale-up. Indeed, industrial fiber spinning process has a yarn take-up rate of 200-1500 m min^{-1}, whereas electrospun yarn has a take up speed of 300 m min^{-1}. Until 1990s, there was very little research and investigation on this topic (Baumgarten, 1971). Some researches on the behavior of thin liquid jets in an electric field are conducted (Zeleny, 1971, Taylor 1964, 1966, 1969).
In the mid 1990s, electrospinning from polymer solution was reinvestigated by the Reneker group.
In the biomedical field, the most used technique is the *Melt Electro Spinning, (MES)*, which avoids the use of toxic solvents: nowadays, a rising number of researchers focuses on electrospinning with polymer melts rather then dissolving them in solvents. Dalton used electrospun polymer melts to deposit fibers directly on cells to build a layered tissue. In that way, cytotoxic solvent are not introduced into the cell culture when the fibers are deposited.
While there have been patents for different electrospinning setups since the 1900s, it is just in the last decades that researchers focused on electrospinning to fabricate nanofibers assemblies. Before going deep into the detailed mechanism of electrospinning, it is worth to have a look to the major applications of electrospun nanofibers.

3.2.1 Applications

Four main application areas for electrospun nanofibers can be identified: Bioengineering, Environmental Engineering and Biotechnology, Energy and Electronics, Safety and Defense (*Ramakrishna et al*, 2005).

1. Bioengineering: nanofibers are used for (i) tissue engineering for tissue reconstruc-

tion, (ii) wound dressing, (iii) affinity membranes and (iv) drugs delivery.
(i) Tissue scaffolds are employed to repair damaged human tissues. Seeded cells stick there and grow on tissue scaffolds, dipped in the nutrient media and the scaffold are implanted at the human tissue defects.
(ii) Wound dressing is a therapy employed to repair the skin damaged by ambustion or injury. Electrospun membranes are used in this field, since they adhere at wet wound surface, avoiding fluid accumulation. Electrospun membranes have high gas permeation and they protect the wound from infection and dehydration. An electrospun membrane is a porous structure but also a good barrier.
(iii) Affinity membranes allow the purification of streams, based on physical/chemical properties or biological functions, rather than molecular weight or size. Affinity membranes do not work on the sieving mechanism but they operate on the selectivity of the membrane to capture molecules, immobilizing some of them on their surface.
(iv) Drug delivery system has been studied employing polymeric materials, hydrogels, micelle. These polymeric drug improved therapeutic effect and reduced unwanted effect, but the drug releasing rate is still a matter of study. Instead of conventional polymeric materials, nanofibers membranes can encapsulate medical drugs and release them.

2. Environmental Engineering and Biotechnology: the function of nanofibrous membranes is to filter moisture and dusts. Unclean air which contains bacteria can be purified using fibrous nano-scale membrane. The surface can be chemically modified to kill bacteria. Filter media is employed to purify air that contains solid particles (virus, dust), but also smog and chemical solvents. High-Efficiency-Paticulare-Air (HEPA) filter of non-woven glass fiber mesh have been employed. However, to remove ultra-fine particles, mesh pore size must be small. Low pressure drop are required: electrospun membrane has a great potential and they are a promising future application in this field.

3. Energy and Electronic: clean and renewable energy are the focus in the research field nowadays: wind turbines, solar generators, hydrogen battery, lithium polymer batteries are some example. In the polymer batteries field, the usage of electrospun

polymer fibers has been expected: the membrane has a pore structure, a network of fibers, and they can be compactly packed into a small package. A fibrous structure is responsible of high electrolyte uptake, large surface areas leads to high ion conductivity. The important properties, indeed are: ion conductivity, interfacial resistance and electrochemical stability. Conductive nanofibers can be successfully employed also in supercapacitors.

4. Safety and Defense: electrospun nanofibers are employed in this field as gas, chemical, optical sensors and biosensor. Nanofibers have a high surface to volume ratio and thus can lead to sensitive sensors. Some qualities are: sensitivity, quick response time with a targeted material. Nanofibers use the chemical or physical reaction between a targeted material and a sensing material. They convert a chemical phenomenon to an electrical output.

   Furthermore, nanofibers can be employed as protective mean from chemical and biological agents. Some expected properties are: lightweight and breathable fabric, permeability to air and water vapor, insolubility in all solvents and reactive with nerve gases and other chemical agents. Nanofibers fabric have a high specific surface area, they are able to neutralize chemical agents. The fibers have a high porosity but very small pore size: they are resistant to the penetration of chemical harmful agents.

3.3 Electrospinning process

Electrospinning is a very versatile approach used to make nanofibers by the application of electrostatic forces: both a molten solution or a solvent-polymer solution can be employed. In this work solvent-polymer solution is taken into account.

Although it seems a simple technique, it is worth to notice that several parameters do play a significant role in electrospinning (coulombic, electric field, viscoelastic, surface tension, air drag, humidity, gravitational forces). In an oversimplified view, when the voltage overcomes a defined threshold value (depending on the very specific system and process conditions), electrostatic charging of the fluid at the tip of a nozzle leads to the formation of the so called ”Taylor cone”, from the apex of which a single fluid jet is ejected. The jet moves towards a ground collector which is the counter electrode. Elec-

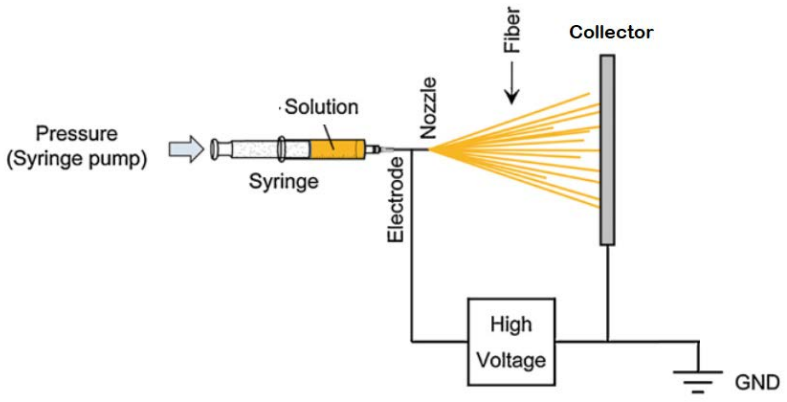

Figure 3.1: Electrospinning setup

trospinning jet could be thought as a string of charged elements in a viscoelastic medium: one end is fixed at the origin and the other end is free. A typical experimental set-up is represented in Fig. 3.1.

It is composed of a syringe-pump where the polymer solution is contained in a plastic syringe: the piston of the syringe is displaced by a volumetric pump at a constant rate: typical flow rates are between 0.002-2 mL/min. An electrode dipped in the polymer solution or in contact with the syringe needle is connected to a high voltage supply. The internal needle diameter is usually between 0.7-1 mm, while the electric potential is set between 5 and 30 kV. When the high voltage supply is turned on, the electrode induces free charges in the polymer solution. The charged ions move in response to the applied electric field toward the electrode of opposite polarity, transferring tensile forces to the polymer solution. The target or collector can be set at ground potential or be kept at a opposite polarity with respect to the polymer solution. The collectors are normally placed at a distance of 10-30 cm from the tip of the syringe. Different types, shapes and size of target can be employed: they are summarized in the following section.

3.3.1 Collector

Different types of collector can be employed. Normally a static single collector is adopted (as the one displayed in Fig. 3.1(a)). However, different collector types can be employed. Rotating collectors (Fig. 3.1(b)) rotate either rapidly to align the collected fibers or slowly to give to the fibers a random network. If the angular moment is big enough, fibers align themselves along an axis. Dual collectors (Fig. 3.2(d)) have proven to be the best solution if a ordered, aligned network is desired. Furthermore, the fibers can be easily transferred

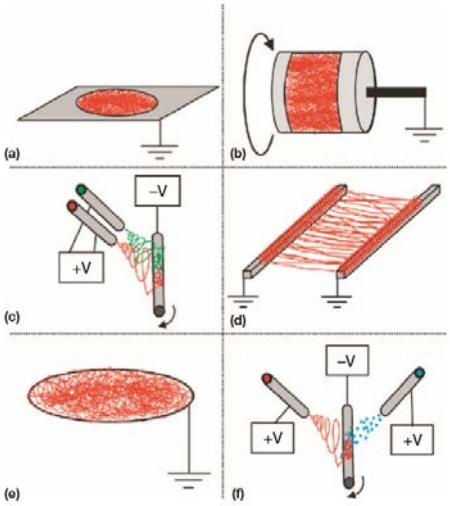

Figure 3.2: Different collector for electrospinning: (a)single collector, (b) rotating collector (c) co-electrospinning onto a rotating collector (d) dual collectors (e) ring collector and (f) simultaneous electrospinning and electrospraying onto a rotating collector (*W. Cui et al.*, 2011).

from the dual collector to any other substrate. In this case, with respect to the rotating collectors, the oriented fibers are normally single and suspended without contact with other ones: dual collector is useful where a dilute concentration of fibers is required on the surface. One problem of the dual collector is that it is not a continuous process, since the fibers start becoming non-uniform as the deposited fibers begin to insulate the collector. Also, rings collectors can be employed (Fig. 3.2(e)), coelectrospinning onto a rotating drum (Fig. 3.2(c)) that employs two different polymer solutions at the same time. On Fig. 3.2(f) both electrospinning and electrospraying (Section 3.8) are employed.

3.4 Nanofibers formation

When an electric potential is applied between the polymer solution and the collector, the charges accumulate and they are forced to the surface of the ejected droplet at the end of the needle. When the electric force is greater than the cohesive solution force, an electric-charged jet of the solution erupts. As the jet approach the target, it is elongated by electrostatic interactions between charges. In the same time, the solvent evaporates and the jet solidifies into a fiber on the collector. The electrospinning process is rather complex: Reneker and Fong examined different regions: they are listed and briefly described below:

3.4.1 Charging of the fluid

The first step can be splitted into two different sub-steps: the generation of the drop and the formation of the Taylor cone jet. In the first part the polymer solution is pumped through the syringe needle at low flow rate. The forces present on this droplet are the liquid surface tension (F_γ) and the gravity (F_g): the electric field is not applied in this moment. The radius of the droplet (r_0) at the needle tip can be computed as:

$$r_0 = \sqrt{\frac{3R\gamma}{2\rho g}} \tag{3.1}$$

where R stands for the internal radius of the needle, ρ is the liquid density, g is the gravity acceleration. Drops in this case fall on the ground, because of the gravity acceleration: even if the applied electric field is too low, the droplets can fall. As soon as the applied voltage is set to a sufficiently high value, the surface tension can be counterbalanced by the electric and gravity force ($F_\gamma = F_E + F_G$). The electric force that exists between the needle and the collector is:

$$F_E = \frac{4\pi\epsilon V^2}{ln(\frac{4L}{R})^2} \tag{3.2}$$

where L is the needle-collector distance, ϵ is the permittivity of the medium (air) and V is the applied voltage. The radius of the droplet is:

$$r = \sqrt[3]{\frac{3}{2\rho g}\left[R\gamma - \frac{2\epsilon V^2}{ln(\frac{4L}{R})}\right]} \tag{3.3}$$

which is the more general form of Equation 3.1: it can be obtained assuming null voltage. The radius decreases as the voltage increases: when the voltage reaches the critical value (V_C), the droplet is subjected to instability. The electric field leads to charge separation in the solution droplet. The needle is normally positively charged and so, on the surface of the droplet there is an accumulation of positive charges: the negative charges displace to the internal part, until an equilibrium point where the electric field inside the droplet is zero. The charge separation is responsible of a force which opposes to the surface tension. A droplet on the tip of the needle is stable when the surface tension (that acts inward) is bigger with respect to the repulsion of the forces, which acts outwards. The equilibrium condition is expressed by:

$$F_E \leq r\rho\left(\frac{r^2}{\beta} - V\right) \tag{3.4}$$

where β is the shape factor of the droplet. The maximum surface charge that a droplet can withstand is given by Rayleigh condition:

$$Q_R = 8\pi\sqrt{\epsilon\gamma r^3} \tag{3.5}$$

if the charge is higher than the Rayleigh one, the droplet deforms and then breaks into smaller droplets due to the repulsion between the positive charge on its surface.

3.4.2 Formation of the cone-jet

The droplet that is subjected to an electric field undergoes to deformation. The stretched droplet assumes the shape of a cone from which a thin liquid jet erupts. This shape is the so called "Taylor cone" and occurs when the voltage is the critical one V_C expressed as:

$$V_C = \sqrt{\left(\frac{2h}{L}\right)^2\left[ln(\frac{2L}{R}) - 1.5\right]\left(0.117\pi R\gamma\right)} \tag{3.6}$$

in which h is the needle length. The droplet moves from a spherical shape to an ellipsoid: in this way fibers can be obtained. From Eq. 3.7 it is worth to notice that the critical voltage increases as the surface tension increases. Also, solvents with high viscosity and low conductivity need high voltage. The electrostatic force ($F_E = qE$) moves the charges in the direction of the electric field, while the viscous drag force ($F_D = \pi\eta r\mu E$) tries to hold the charges.

3.4.3 Jet thinning

When the critical voltage is reached, the jet starts to appear. In the jet there is a repulsive force on the superficial charges accumulated in the jet. In the first phase the jet is stable, due to polymer chain entanglements. The jet undergoes to a thinning during its travel from the needle to the collector. The velocity increases more and more, due to jet stretching and to evaporation of the solvent. So, the jet, that accelerates more and more, is thinned progressively.

3.4.4 Jet instability

At the beginning of its travel, the jet has a straight shape, while it becomes instable approaching the collector and bends, moving with an oscillating trajectory. It undergoes to an increase of the surface and a decreasing of the charge density. Different instabilities are present in this phase, concurring to the *Whipping Instability*: namely they are: Rayleigh instability, instability symmetric to the axis and bend instability. The onset of a type of instability depends on the applied electric field. The movement of the jet is similar to hits of whip and it is confined in a conical shape, symmetrical to the axis of the jet. In this phase, the speed of surface area increment and the evaporation rate are high and it leads to the reduction of nanofibers diameter. In this stage the forces acting on the jet are: gravity, electrostatic (introduces the jet and push it towards the collector), the viscoelastic forces (they oppose to the jet fragmentation), the surface tension forces (they operate against the jet stretching) the frictional forces between the jet surface and the surroundings. The sum of these force have an impact on the diameter. The detailed quantitative description of this process is difficult, since these forces vary with high velocity due to the solvent evaporation and charges dissipation.

3.4.5 Jet solidification

The jet travels to the collector and in the same time the solvent evaporates, leading to nanofibers formation. No residual solvent should be present at the deposition on the collector, to prevent welding of the fibers. The evaporation rate depends on the distance between the needle and the collector and on the solvent vapor pressure. Figure 3.3 is a graphical representation of different electrospinning phases. On the right-hand side, the jet is represented: the first linear segment is depicted, that evolves to the Taylor cone, due to the onset of different instabilities.

3.5 Electrospinning parameters

Electrospinning technique, although being fast, simple and do not requiring complex instrumentations, have a great number of variables that can affect its performance. The parameters are different and they can be classified into three groups, depending on their

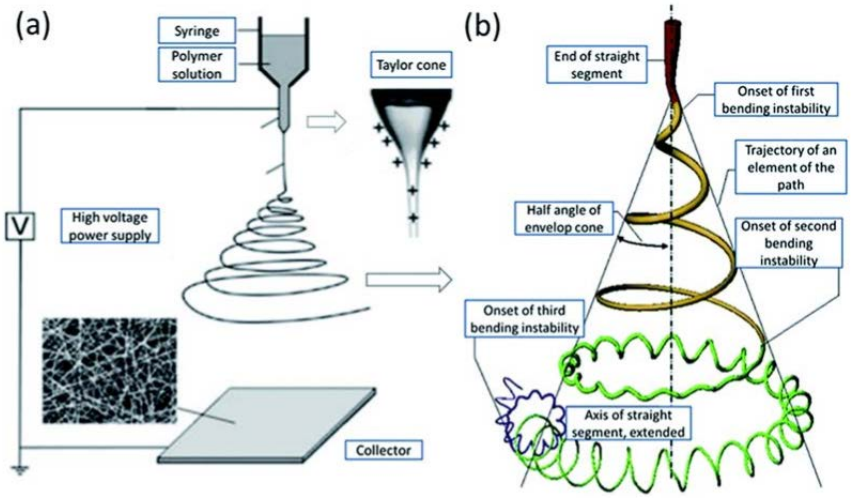

Figure 3.3: (a) Schematic electrospinning setup (b) Polymer jet from the needle tip (straight segment) to the collector, with instabilities onset.

origin and nature: polymeric solution parameters, process parameters, ambient parameters:

3.5.1 Parameters of the polymeric solution

The properties of polymer solution have a strong impact in the process and on the fiber morphology. The surface tension affects the formation of beads along the fiber length. The viscosity and the electrical properties determine the extent of elongation. This, have in turn an effect on the electrospun fiber diameter.

1. Molecular weight and solution viscosity: a necessary condition for electrospinning is that that the polymer must have a sufficient molecular weight and the solution must be of sufficient viscosity. The solution, as the jet leaves the needle, is stretched as it travels towards the collector. During the stretching of the polymer solution, the entanglement of the molecule chains is responsible for avoiding the breaking of the electrically driven jet and maintains a continuous solution jet. For example, monomeric polymer solution does not form fibers, if electrospun. The polymer length (i.e. related to its molecular weight) determines the amount of entanglement of the polymer within the solvent. Another way to increase the viscosity is to increase the polymer concentration. A higher concentration causes more chain entanglements, which is necessary to maintain the jet during electrospinning. The entanglements have a significant impact on whether the jet breaks up into small

droplets or whether fibers contain beads.

On the opposite side, a too high viscosity makes it very difficult to pump the solution out of the syringe needle, and the solution might dry at the tip of the needle before electrospinning can start. With increased viscosity, the diameter of the fiber also increases, due to the greater resistance of the solution to be stretched by the charges on jet.

2. Surface Tension: the beginning of electrospinning needs that the charged solution to overcome its surface tension. However, as the jet moves to the collector, the surface tension might cause beads formation along the jet. Surface tension decreases the surface area per unit mass of the fluid. When there is a high concentration of free solvent molecules, the solvent molecules arrange themselves into a spherical shape, because of surface tension. Increasing viscosity (greater interaction between solvent and polymer), the solvent molecules spread over the entangled polymer molecules, reducing the tendency for the solvent molecules to aggregate under the influence of surface tension. Ethanol can be added to the solution to favor the formation of smooth fibers. Another approach to reduce the surface tension is to employ a surfactant to the solution. The surfactant yields more uniform fibers.

3. Solution Conductivity: electrospinning involves stretching caused by charge repulsion at its surface. Increasing the conductivity, more charges can be carried by the jet. The conductivity can be increased by the addition of ions. A small amount of salt or a polyelectrolyte, therefore it leads to a more stretched solution. Bead formation occurs if the solution is not fully stretched. As a result, employing salts, smooth fibers are formed which may otherwise yield beaded fibers. The increasing solution stretching tends to yield fibers of smaller diameter. However, there is a limit to the reduction in the diameter. As the solution is being stretched, there will be a greater viscoelastic force acting against the columbic forces of the charges. Employing ions has the further effect of decreasing of the critical voltage for electrospinning.

4. Dielectric effect of Solvent: it has an important influence on electrospinning. A greater dielectric property reduces the beads formation and the diameter of the electrospun fibers. The bending instability of the jet increases with higher dielectric

constant. This is shown by increased deposition area of the fibers. It also favors the reduction of the fiber diameter due to the increased jet path.

3.5.2 Process parameters

Different process parameters can influence the electrospinning process. These parameters have an influence in the fiber morphology, however their influence is less significant than the solution parameters:

1. Voltage: the high voltage induces the necessary charges on the solution and, together with the external electric field, start the process when the electrostatic force in the solution overcomes the surface tension of the solution. Both negative or positive voltage more than 6 kV is able to cause the solution drop at the tip of the needle to distort into the Taylor cone. A higher voltage causes a greater stretching of the solution due to the greater columbic forces in the jet as well as the stronger electric field. These have the effect of reducing the diameter of the fibers and favors faster solvent evaporation to yield drier fibers. At a higher voltage, there is a greater tendency for beads formation. Employing auxiliary electrodes is a solution to change the electric field between the needle and the collector.
   Normally DC voltage supply is used, it is also possible to use an AC potential.

2. Feedrate: the feedrate determines the amount of solution available for electrospinning. Increasing the feedrate causes an increment in the fiber diameter or beads size. There is however a limit to the increase of the fiber diameter due to higher feedrate. A greater volume of solution drawn from the needle tip implies a longer time to the jet to dry. The solvents in the deposited fibers might not have enough time to evaporate given the same flight time. The residual solvents can cause the fibers to fuse together when they make contact. In conclusion, a lower feedrate is more desirable: the solvent have more time for evaporating.

3. Temperature: increasing the temperature leads to a higher evaporation rate and to a lowered viscosity of the polymer solution. For example, electrospinning of polyurethanes at higher temperature cause beads to fibers that have more uniform diameter. It is due to the lower viscosity of the solution and to the higher solubility

of the polymer in the solvent: it allows more even stretching of the jet. With a lower viscosity, the Columbic forces exert a greater stretching force on the solution, which leads to smaller diameter fibers. Furthermore, the increased temperature favors a higher molecules mobility, which in turn allows the Columbic force to stretch the solution further. Temperature cannot be increased too much in case of biological substances, since the temperature can cause molecules functionality loss.

4. Collector: generally, the collector is made of conductive metal (for example aluminum foil), which is electrically grounded: there is a stable potential difference between the source and the collector. Employing a non-conducting material, charges on jet accumulates on the collector, that cause fewer fibers deposited. Fibers collected on a non-conducting material have a lower packing density, caused by the repulsive forces of the accumulated charges on the collector. On the other side, on a conducting collector, charges are dissipated allowing more fibers to be attracted to the collector. Employing a porous collector (paper or metal mesh), the deposited fibers have a lower packing density than smooth surfaces (as metal foils). In a porous support, there is a faster evaporation of the residual fibers because of higher specific surface; in smooth surface there is an accumulation of solvent around the fibers due to slow evaporation rate. The diffusion of the solvent gives rise to a more packed structure. A rotating collector is employed to prepare aligned fibers, furthermore it gives more time to the solvent to evaporate. For example, employing dimethyl formamide, which is good for electrospinning but has a high boiling point, might cause wet fibers when they are collected. A rotating collector increase the evaporation rate, thus improving the morphology of the fibers.

5. Diameter of the needle: a smaller diameter of the needle reduces the clogging, reduces the amount of beads on the fibers. The reduction in the clogging is due to lowered exposure of the solution to the atmosphere. Also, a smaller needle causes a reduction in the diameter of the fibers. When the droplet size decreases due to a smaller internal diameter, the surface tension increases. At constant voltage, a greater columbic force is required to cause jet initiation. The jet is therefore less accelerated and it cause a longer time for the solution to be stretched and elongated

before it is collected.

6. Needle-Collector distance: decreasing the distance, the jet has a shorter distance to travel and the electric field strength increases at the same time: for that reason, the jet is more accelerated. When the distance is too low, the excess solvent may lead to fibers merging when they contact: the interconnection fiber mesh cause additional strength to the yarn. When distance is too low, beads are observed on the fibers. Decreasing the distance has the same effect of increasing the voltage supplied, which leads to a higher field strength.

3.5.3 Ambient Parameters

The jet surroundings has an effects on the electrospun fiber morphology.

1. Humidity: at high humidity, it is possible that water molecules condense on the fiber surface, when the process is carried out under normal atmosphere, especially when polymer are dissolved in volatile solvents. At low humidity, the fibers are smooth, but increasing humidity, circular pores are likely to form on the fiber surfaces. Furthermore, the size of the pores increases with increasing humidity, up to a coalescence to form large, non uniform shaped structures. At a very low humidity, a volatile solvent dries rapidly.

2. Type of atmosphere: different gases have been tested under high electrostatic field. For example, helium breaks down under electrostatic field, and thus electrospinning is not feasible.

3. Pressure: when the pressure is below atmospheric one, the polymer solution in the syringe is favored to flow out of the needle: it causes unstable jet initiation. As the pressure decreases, there is a solution bubbling at the needle tip. Lowering further the pressure cause a direct discharge of the electrical charges.

3.6 Theoretical model

As mentioned before, Taylor theorized the critical voltage: it is the voltage which, keeping all the other parameter constants, stretches the polymeric solution on the needle tip,

to yield the so called "Taylor cone". The drop is in equilibrium between the electric field and the surface tension. The critical voltage is expressed as:

$$V_C = \sqrt{\left(\frac{2h}{L}\right)^2 \left[ln(\frac{2L}{R}) - 1.5\right] \left(0.117\pi R\gamma\right)} \tag{3.7}$$

This formulation does not take into account neither the conductivity, nor the viscosity: it can be used with medium/low viscosities. Baumgarten verified that a higher viscosity influences the fiber diameters according to a quadratic relationship ($d \propto \eta^{0.5}$). Other researches focus on quantitative methods to evaluate the optimum conditions to run electrospinning. These methods are based on the conservation equations. Electrospinning models make use of three conservation quantities (mass, momentum and charge).

1. Conservation of Mass: considering an infinitesimal length dz of the electrospinning jet: the mass can be computed as;

$$m = \rho\pi R^2 dz \tag{3.8}$$

where ρ is the liquid density (assumed to be constant), and R is the jet radius. Over an infinitesimal time dt, the mass flow into and out from the control volume are: (v is the liquid velocity)

$$m_{in} = \rho\pi R^2 v dt|_z \tag{3.9}$$

and

$$m_{out} = \rho\pi R^2 v dt|_{z+dz} \tag{3.10}$$

which yields the conservation equation:

$$\rho\pi R^2 v dt|_z - \rho\pi R^2 v dt|_{z+dz} = 0 \tag{3.11}$$

From the last equation, it follows that:

$$\frac{\partial R^2}{\partial t} + \frac{\partial R^2}{\partial z} = 0 \tag{3.12}$$

2. Conservation of Momentum: Momentum of the fluid segment bounded by sections

z and $z + dz$ is

$$\vec{M} = \rho\pi R^2 v dz \tag{3.13}$$

In the balance the influx and outflux of momentum into and out from the bounded volume in the time interval dt need to be considered. Furthermore, due to the liquid pressure exerted on the cross section, the momentum is taken from the integral of cross-sectional force over time. Taking momentum balance:

$$\Delta\vec{M} = \vec{M}_{in} - \vec{M}_{out} + \vec{M}|_z - \vec{M}|_{z+dz} \tag{3.14}$$

which yields, after some algebraic manipulation to:

$$\frac{\partial v}{\partial t} + v\frac{\partial v}{\partial z} = -\frac{1}{\rho D^2}\frac{\partial pD^2}{\partial z} \tag{3.15}$$

A detailed momentum balance equation according to Feng (2002):

$$\frac{d}{dz}(\pi R^2 \rho v) = \pi R^2 \rho g + \frac{d}{dz}[\pi(-p + \tau_{zz})] + \frac{\gamma}{R}2\pi RR' + 2\pi R(t_t - t_n D') \tag{3.16}$$

where g is the gravity acceleration, p is liquid pressure, γ is the surface tension, t_t and t_n are respectively the tangential and normal traction on jet surface due to electricity, while R' is the slope of the jet surface with respect to jet axis.

3. Conservation of Charge: the conservation of charge equation is expressed as:

$$I = \pi D^2 KE + 2\pi Dv\sigma \tag{3.17}$$

where I is the electric current, K is the liquid conductivity, E is the vertical component of the electric field, σ is the superficial density charge. The forces acting on the jet have to satisfy the second Netwon's law. Reneker et al. suggest a good model but they do not take into account the jet instability:

$$m\frac{\partial^2 P}{\partial t^2} = f_C + f_E + f_V + f_S + f_A + f_G \tag{3.18}$$

The expression of the forces that are present in equation 3.18 are:

Coulomb force:

$$f_C = \frac{e^2}{l^2} \tag{3.19}$$

Electric force:

$$f_E = -\frac{eV}{L} \tag{3.20}$$

Viscoelastic force:

$$f_V = \frac{d\sigma_V}{dt} = \frac{G}{l}\frac{dl}{dt} - \frac{G}{\eta}\sigma_V \tag{3.21}$$

Surface tension:

$$f_S = \frac{\alpha\pi R^2 k}{\sqrt{x_i^2 + y_i^2}}[i|x|sign(x) + j|y|sign(y)] \tag{3.22}$$

Air drag:

$$f_A = 0.65\pi R\rho_{air}\nu^2\left(\frac{2\nu R}{\nu_{air}}\right)^{-0.81} \tag{3.23}$$

Gravitational force:

$$f_G = \rho g\pi R^2 \tag{3.24}$$

where e is the electric charge, l is the length of the straight jet, V is the potential difference that exists between the droplet and the collector, σ_V is the viscoelastic tension, G is the elastic modulus, η is the viscosity, α is the surface tension coefficient, k is the jet curvature, ρ is the density and ν is the kinematic viscosity.

3.7 Creation of Different Nanofibers

Changing some parameter of electrospinning, different morphologies of the nanofibers can be obtained. Beside beaded and non-beaded fibers, electrospinning is able to produce also other types of fibers with interesting morphologies and different types of nanofibers. Porous nanofibers can be obtained by varying the humidity of the environment. During the solvent evaporation, the solution is thermodynamically unstable. It thus leads to a phase separation in two phases: one polymer-rich and a polymer-poor phase. The polymer rich phase solidifies and forms a matrix, while the polymer-deficient forms the pores.

Flattened or ribbon-like fibers are obtained because of solvent evaporation during the

process. Water solvent evaporation reduces with higher solution viscosity and wet fibers that reach the collector are flattened by the impact.
Branched fibers arise from ejecting smaller jets from the surface of the primary jets. The elongation of the jet and evaporation of the solvent modify the shape and the charge per unit area carried by the jet. The jet can therefore become unstable. The instability can decrease the local charge per unit surface by ejecting a smaller jet from the surface of the primary jet or by splitting apart two smaller jets.
Helical fibers can be employed in micro-electro-mechanical system devices, optical components and drug delivery systems. They are made of a mixture of (poly)ethyleneoxide (PEO) and (poly)aniline sulfonic acid (PASA). Changing the composition of PEO, the diameter of the loop can be controlled. Force imbalance occurs, which causes fiber structural rearrangements in order to retain the force equilibrium.
Hollow nanofibers and nanotubes can be prepared via electrospinning: they are employed in separation, gas storage and energy conversion. Furthermore, employing coaxial electrospinning method it is possible to produce electrospun fibers with different polymers. In that way, core materials that will not form fibers via electrospinning can be prepared. The outer shell polymeric material is the template. They are used in drug delivery and photocatalysis.

3.8 Electrospraying

Electrospraying was initially used to produce thin film for nuclear-physics instruments; later it was employed to prepare thin films for solar cells, and there is a growing interest in employing this technique to synthetize electrodes and solid electrolytes for fuel cell and lithium batteries. It is used also in the production of solid lubricating films or photoresists.
Electrospraying employs electrical forces to perform liquid atomization. The droplets are extremely small, down to the order of 10s nanometer, and by varying the electrical field, the size of the droplets can therefore be controlled. The atomizer nozzle is a metal capillary, which is subjected to a high voltage. The liquid surface undergoes to a shear stress that causes elongation of the jet and the subsequent disintegration into droplets. The droplets can be extremely small, down to nanometers. The droplets are highly charged:

the charge can be up to a fraction of the Rayleigh limit, which is the magnitude of charge on a drop which overcomes the surface tension force that leads to the drop fission. The charge is given as:

$$Q_R = 2\pi(16\sigma_1\epsilon_0 r^3)^{1/2} \tag{3.25}$$

in which σ_1 is the liquid surface tension, ϵ_0 is the electric permittivity of the free space, while r is the droplet radius. Varying the liquid flowrate and the voltage, the charge and size of the droplet can be modified. Electrospraying is a promising technique for the production of high-quality layers and film: it allows generating fine droplets in micro size range, with a narrow size distribution. Furthermore, it is easy to be controlled, varying liquid flow rate or the applied voltage and it is less expensive than other techniques. Several advantages exist: monodisperse particle in cone-jet mode are produced (it is difficult to achieve by other particle synthesis method), the number of molecular aggregates due to coalescence of droplet with the same polarity is minimized. Also, it is notable that the product contamination is lowered, it can be operated at ambient conditions, it is cost effective and it is simple to operate. The basic setup is represented in Fig. 3.5a: it consists of a high voltage supply, a metal capillary and a grounded collector, similar to the electrospinning one (Fig. 3.1).Two main systems can be employed:

1. simple nozzle facing the substrate: high voltage is applied to the nozzle or to the substrate: the counter electrode is grounded (Fig. 3.4(a)). A disadvantage is that the substrate is an active electrode and needs to be conducting.

2. nozzle-extractor system: the system operates independently of the substrate: the nozzle is kept at high potential, the extractor and the substrate are grounded, (Fig. 3.4(b)). A disadvantage in this case is that a fraction of the total number of the droplets falls on the extractor electrode: precautions are needed to avoid this deposition.

The electrostatic spray deposition (ESD) processes are carried out at lower temperature than solid-state reactions. The optimum temperature of the substrate is critical for the process, for layer uniformity and porosity. Porosity depends on fast evaporation of the solvent, and increases with the substrate temperature.

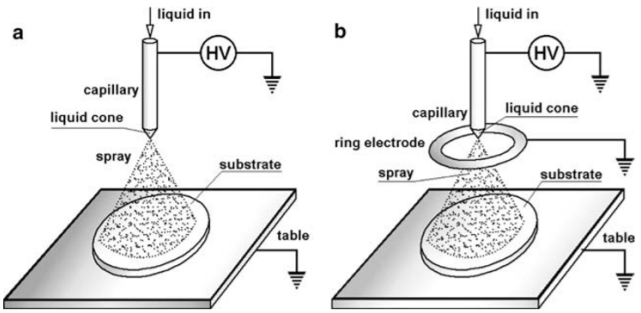

Figure 3.4: Thin film deposition by liquid atomization (a) simple nozzle for direct spraying (b) nozzle-extractor system

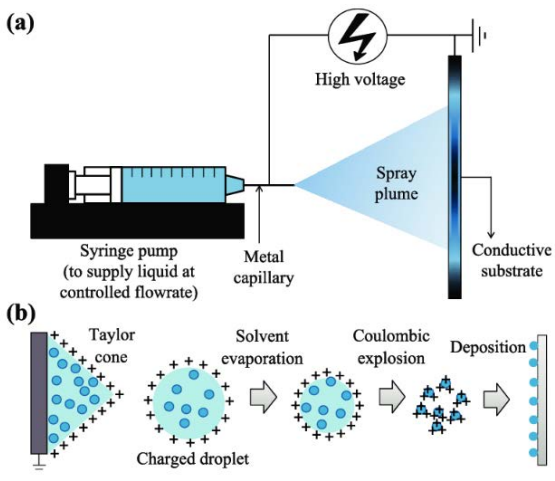

(a) *Electrospraying process setup (above), and its mechanism (below), (Saalah S. et al, 2018).*

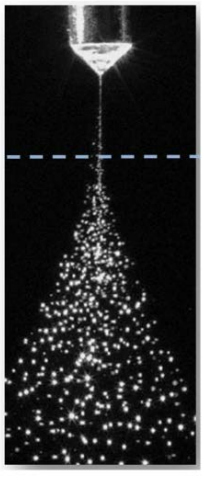

(c)

(b) *Electrospraying frame (Agathou et al., 2012).*

Figure 3.5: Electrospraying process

Electrospraying process can be divided into three stages: droplet formation, droplet shrinkage and gaseous ion formation. The solution delivered to the tip of the capillary is subjected to the electric field. Working with a positive potential, positive ions in solution accumulate at the surface: a ”Taylor cone” is then formed. The cone is then drawn to a filament, which produces positively charged droplets in a ”budding” process: the surface tension is exceeded by the applied electrostatic force. The diameter of the droplet is influenced by several parameters, as the applied potential, the solution flow rate an solvent properties. Evaporation of solvent from the droplets is responsible for a diameter reduction. At the ”Rayleigh limit”, a fission (”Coulomb explosion”) occurs: in that occasion the charge is enough to overcome the surface tension that holds the droplet together. The continuous depletion of the droplet size by solvent evaporation and fission cause the formation of droplets containing a single ion. Ion evaporation occurs on small, highly charged droplets: the charge repulsion is the driving force. Figure 3.5a(a) shows the droplet production in the electrospray interface. Figure 3.5a(b) shows a frame of the electrospraying process: the linear segment and the Taylor cone can be easily noted.

References

Agathou M. S., Kritsis D., ”Electrostatic atomization of hydrocarbon fuels and bio-alcohols for engine applications”, *Energy Conversion and Management*, **60**: 10-17.

Cui W., Chang J., Dalton. P. D., (2011), ”Electrospun Fibers for Drug Delivery”, *Comprehensive Biomaterials (2011)*, **4**, 445-462.

Javorek A., (2007), ”Electrospray droplet sources for thin ffilm deposition”, *Journal of Material Science*, **42**: 266-297.

Saalah S., Lenggoro W., (2018), ”Nanoparticles carrying Biological Molecules: recent advances and application”, *Powder and Particle Journal*.

Wunner F. M., Florczak S., Mieszczanek P., Bas O., De-Juan-Pardo E. M., Hutmacher D. W., (2017), Electrospinning with Polymer Melts - State of the Art and Future Perspectives”, *Comprehensive Biomaterials II*, **5**.

Chapter 4

Materials and Methods

In this chapter employed materials are described. Then, the instruments used and the analytical techniques are described.

4.1 Materials

The main materials employed in this work are: the polymers to prepare membranes, the solvents to solubilize the polymer and disperse the catalysts and finally the catalysts themselves. Solvents and polymers are chosen according to previous works (*Folli*, 2012, *Querini*, 2013).

4.1.1 Polymer

Electrospinning (described in detailed in the previous Chapter) employs a polymeric solution. On the polymer layer, then, the solution containing a different catalyst is deposited via electrospraying. In this multicomponent system, the polymer is the catalyst support, but also favors, due to its intrinsic high specific surface, intimate contact between the pollutant and the catalyst particles. The polymer used to prepare the photocatalytic membranes is polyacrylonitrile, (shortened as PAN), the repetitive unit is shown in Figure 4.1.

PAN is a synthetic polymer prepared by the polymerization of acrylonitrile. The process of polymerization was known since 1890s, however the first commercial fibers appear in the 1940s, when the proper spinning solvents were discovered.

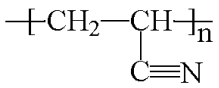

Figure 4.1: Polyacrylonitrile repetitive unit

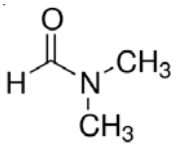

(a) *Dimethyl-formamide structure formula.*

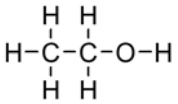

(b) *Ethanol structure formula.*

Figure 4.2: Solvents

PAN it is a rigid, hard thermoplastic material: it is resistant to most solvent, it is slow to burn and it has low gas permeability. It does not melt under normal condition and it degrades before melting (glass transition temperature T_g=110℃, melting temperature T_m=310℃). It possesses good mechanical properties, it is easy to manipulate and spin and it has UV-resistance properties. Previous studies (*Pozzan*, 2013) proved that PAN is a convenient choice for this kind of application.

4.1.2 Solvents

The solvent used in the dissolution of PAN is N,N dimethyl formamide (DMF). DMF allows to dissolve PAN and favors a homogeneous distribution on the collector: employing this solvent, also, leads to small fiber diameters formation.
Catalysts are dissolved in ethanol (EtOH): with respect to other solvents, it is less aggressive to polymeric nanofibers.
The structure formula of these solvents are reported in Fig. 4.2a-4.2b. Physical and chemical properties are reported in Table 4.1. DMF is a polar aprotic solvent: it is worth to notice that the choice of the proper solvent is very important: its viscosity, electric conductibility, surface tension, dielectric constant and vapor pressure should be suitable for the electrospinning solvent application.

Table 4.1: Physical-chemical properties of solvents

Property	DMF	EtOH
Molar weight [g/mol]	73.10	46.07
Boiling temperature (1 atm) [℃]	153	78.4
Liquid density (20℃) [kg/m^3]	940	789
Viscosity (20℃) [cP]	0.92	1.2
Sufrace tension (20℃) [mN/m]	37.10	22
Dielectric constant (25℃) [-]	36.7	24.3
Vapor pressure (20℃) [kPa]	0.380	5.95

Table 4.2: Catalysts

n.	Catalysts	Quantity [mg]	Preparation
1	TiO_2 P25	1000	
2	TiO_2 Graphene	300	Mechanochemical synthesis, milled for 2h
3	TiO_2 Graphene	1000	Mechanochemical synthesis, milled for 8h
4	TiO_2:Graphene 20:1	1340	Top-down process
5	TiO_2:Graphene 10:1	1250	Top-down process
6	CeO_2-T Graphene	300	
7	CeO_2-T Graphene	300	Mechanochemical synthesis, milled for 2h
8	CeO_2-T Graphene	1000	Mechanochemical synthesis, milled for 8h

4.1.3 Catalysts

The catalysts employed in the tests are reported in Table 4.2. The Table lists the eight catalysts that have been tested, the available quantity, the method whereby they are produced (they are listed in Chapter 2). Titania P25 is purchased by Evonik Degussa, catalysts 2, 3, 7, 8 are supplied by University of Udine, while catalysts 4, 5 are supplied by a private company.

Titanium oxide is AEROXIDE® TiO_2 P25, purchased by Evonik-Degussa: it is constituted by 80% of anatase and 20% of rutile, it is a formed by fine white particles, of average dimension of 21 nm, it has a BET surface of $47\,\mathrm{m^2/g}$. CeO_2-T has a BET surface of $55.6\,\mathrm{m^2/g}$ (*Feng G. et al.*, 2018) and it is a orange-pink powder.

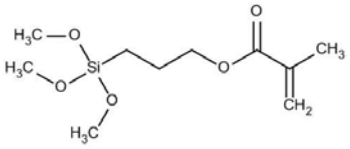

Figure 4.3: Dynasylan 4144 ®structure formula

4.1.4 Dispersant agent

In order to ensure a proper catalyst distribution on the electrospun polymer fibers, to guarantee the maximum surface area and to allow a good catalytic activity, the catalysts are dispersed through a dispersant agent in the solvent (ethanol). In the optimization process, different agents have been tested. Their performance in avoiding catalyst agglomeration in clusters and in favoring electrospraying were assessed. As dispersant agent for titanium dioxide, the chosen one is: Dynasylan®4144, purchased by Evonik-Degussa. It is a silane (3-methacryloxypropyltrimethoxysilane), the structure formula is reported in Figure 4.3. Its formula is $C_{10}H_{20}O_5Si$. It has a viscosity of 2 mPa·s and a density of 1.04 g/L (at 20℃).

4.1.5 Pollutant

The organic pollutant in this work is Methanol, purchased by Scharlau, HPLC purity grade.

4.2 Instruments

In this section, the instruments for solution preparation and for electrospinning are briefly described.

4.2.1 Sonication equipment

Sonicator is an instrument that employs ultrasounds (i.e. sound waves, with frequency higher than 19 kHz) to achieve different goals. For example, it is used to clean lens and jewelry, to disperse solutes in different solvents, to break apart cellular membranes (to extract what is contained inside the cell, for example DNA) and to favor some chemical reactions (in the field of sonochemistry). In this work it is used to perform and speed

Figure 4.4: Sonicator VC505©

up the dispersion of catalysts in ethanol, to minimize the formation of aggregates and clusters. Two different setups can be employed: ultrasound bath and ultrasonic probe. The first is used in cleaning applications, and it is not suitable when a catalyst needs to be dispersed, due to the low and non-uniform power. Probe sonicators, on the other hand, are more versatile instruments and are the preferred choice for dispersing solid in a liquid medium.

The sonicator is composed of: a generator, a converter and a probe. The generator amplifies the AC frequency from 50 Hz to 20 kHz. This signal powers a transducer, that converts the electric signal to a mechanical vibration by means of a piezoelectric crystal. These small vibrations are amplified by the sonicator, until it passes through the probe. The probe moves upward and downwards at a very high speed, the amplitude can be modified by the operator, according to the application. The liquid medium experiences a rapid alternation of compression and depression movements. Pressure variation causes the ”breakage” of the fluid into millions of microscopic droplets. This phenomenon is called ”cavitation”: the bubbles form and collapse and they increase up to 100 μm in diameter. During the collapse, the temperature and the pressure within the bubble can reach 5000℃ and up to 500 atm. Bubble lifetime is usually in the order of microsecond and the solution undergoes to rapid heating and cooling (around 109℃/s). The bubbles that form and collapse create vibration into the solution and prevent the catalyst to form aggregates. A very small probe tip can create good cavitation effects, but it has a very limited area of interest; bigger tips are not energy-intensive, but the waves can reach a larger volume.

The sonicator employed in this work is a VC505© (Fig. 4.4), supplied by Sonic Vibra-Cell. The solid probe is 254 mm long, with a diameter of 13 mm, the power is 500 W. This probe suits for dispersing organic solution that ranges between 10 and 250 mL, which demands high energy intensity.

4.2.2 Electro-spinning/spraying equipment

The experimental equipment used in this work is reported in Fig.4.5.

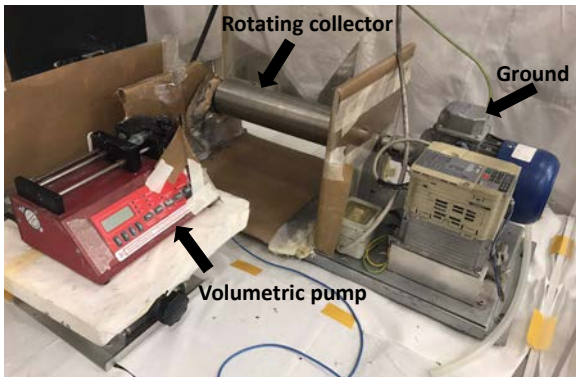

Figure 4.5: Experimental electrospinning-electrospraying setup

The equipment consists of:

1. a plastic syringe which contains the polymeric or the catalyst solution;
2. a volumetric pump: the volumetric pump is provided by New Era Pump Systems, Inc. The displacement of a plastic part at a fixed rate (that can be varied) pushes the piston of the syringe, thus the liquid is ejected from the needle tip.
3. a rotating collector: the collector has a diameter of 7.7 cm and can rotate at different speeds both clockwise and counterclockwise;
4. a high voltage supply generator is provided by Gamma High Voltage. The generator is equipped with two clips: the potential difference can be setted in the range 0-60 kV.

The collector is cylindrical shape, its length is 30 cm, the diameter is 8 cm and it can rotate either clockwise and counterclockwise. A thermohygrometer HD 2301.0, supplied by Delta Ohm is used to monitor mean conditions of humidity and temperature. The setup of Fig.4.5 is placed in a polycarbonate box, to avoid external disturbances and to confine toxic solvent inside the box.

4.3 Characterization methods

In this section the methods employed are described. Membrane characterization is carried out employing scanning electron microscope (SEM) and thermogravimetric analysis (TGA). Catalysts are analyzed with X-ray diffraction (XRD), Diffuse reflectance spectroscopy (DRS). Light source are characterized by an irradiance measure, while the degradation of the pollutant is monitored via gas chromatography coupled with mass spectrometry (GC-MS).

4.3.1 Scanning Electron Microscope (SEM)

The Scanning Electron Microscope (SEM) was invented and optimized in the 1930s and, unlike the optical microscope, does not use the light as a source of radiation: it indeed employs electron beams. The resolution of a microscope is inversely proportional to the employed radiation wavelength: therefore SEM, which employs electrons (whose wavelength is much smaller than the photons) has a resolution which is several order of magnitude higher than optical microscope. SEM makes use of electrons to analyze the signals produced by the interaction between the sample and the electrons themselves. The obtained information are different: morphological, composition of the sample and structural.
The preparation of the sample is rather simple: if it is not conductive, it is made conductive by sputtering with a conducting material (such as graphite or gold (mineralization)). SEM apparatus is represented in Fig. 4.6 and it consists of:

1. an electronic column: the electron beam is generated;
2. a vacuum chamber: here the electron beam interacts with the sample;
3. different detectors that ”capture” several signals that originate from the electron-sample interaction and they transfer them to the computer;
4. a screen where the signals are converted into images.

The electron source on the top of the column is made of a filament (tungsten or lanthanum hexaboride LaB_6), which by thermo-ionic effect, when it is heated at high temperature generates an electronic beam. The electrons are accelerated, thanks to an anode

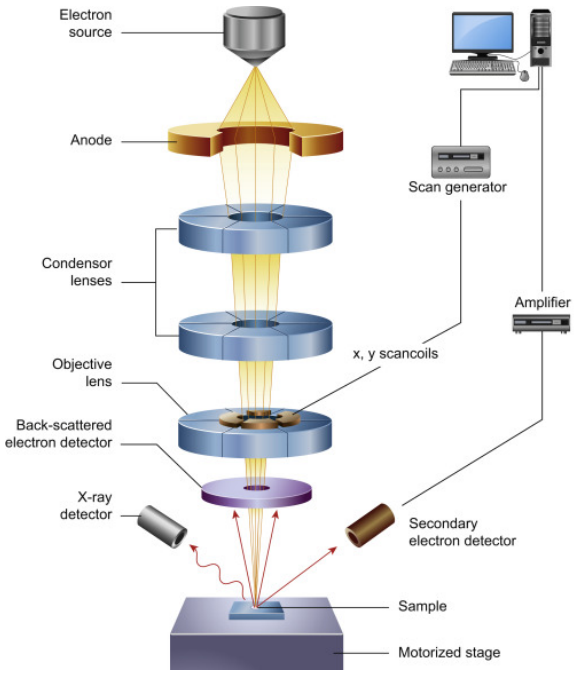

Figure 4.6: SEM apparatus

with a variable energy (100-10000 eV). Some electromagnetic lenses, then, converge and focus the diverging electron beam to obtain a convergent beam. At the bottom of the column, there are a series of coils that deflect the beam, leading to an alternating movement along parallel lines to cover a predefined area. The beam is focused by the final lens, exits the column and approaches the sample, inside the vacuum chamber. If the electrons penetrate in the sample, they lose energy but they re-emitted in different modes. Electron beams interact with the nuclei and with the electronic clouds of the atoms of the sample, both with elastic and inelastic diffusion. Different signals are originated: Figure 4.6 shows back-scattered electrons, X-radiation, secondary electron detector. The interaction volume is the region of the sample from which the interaction signals with the electron beam are generated.

SEM gives a virtual image from the signals emitted. The signals are collected by the proper collector, they are amplified and they are converted from analog signals to digital ones. The collected signals are:

1. secondary electrons (SE): they have low energy (up to 30 eV) and they are originated from the upper part of the sample (few nanometers). This signal is influenced by the morphology of the sample: the image is white and black: gray shades represent the effective tridimensional morphology of the sample;

2. back-scattered electrons (BSE): they are high-energy electrons (from 50 eV to the characteristic energy of the beam), they come from the inner part of the sample (few microns from the surface): their energy depends on the beam energy and on the chemical composition of the specimen, in particular they are related to the average atomic weight. The different gray tonalities are caused by the different chemical composition of the sample: the parts with higher atomic weight appear white, while the ones with lower atomic weight are darker: black is found when there is no emission (empty spaces in the sample);

3. X-rays: they are not due to morphological or chemical composition. RX microanalysis is used to obtain punctual information on the specific chemical composition on a determined point of the sample. The obtained image is a X-ray spectrum, by which is possible to determine the chemical composition of the material, since each peak can be associated to a specific atomic species. Furthermore, it is possible to acquire X-ray, scanning with the electron beam the entire area of the sample. The radiation, collected in each point by the spectrometer, gives as a result a map of the distribution of each chemical element. The lightest zones in the image are due to the higher abundance of the considered element.

4.3.1.1 Environmental Scansion Electron Microscope (ESEM)

With this type of microscope, it is possible to work both in vacuum, but also in differential vacuum conditions, maintaining the high resolution of SEM. Furthermore, biological materials or hydrates samples can be analyzed, without being conductive. Different analysis can be carried out: beside the morphological one, back-scattered electron analysis, qualitative and semi-quantitative elementary analysis, Energy Dispersive X-ray Analysis (EDX).

4.3.2 Thermo-gravimetric analysis (TGA)

Thermo-gravimetric analysis, shortened as TGA is used in this work to characterize membranes. TGA is part of the so called ”thermal analysis”: beside TGA, there are DSC (Differential Scanning Calorimetry) and DTA (Differential Thermal Analysis). They are based on the measurement of a physical dimension, which is temperature-dependent, subject

Figure 4.7: Thermo-gravimetric analysis apparatus, *Q600 TA Instruments*

to a determined time-temperature program. In particular, in TGA analysis, the mass of the sample is continuously measured, function of temperature or time. In that way, the weight difference is computed. The sample is placed in a pan in a controlled atmosphere furnace. The result of the analysis is represented in a thermogravimetric plot: on x-axis there can be time or temperature (in this case there is temperature), while on y-axis mass variation is reported as an absolute or relative percentual. The mass variation due to decomposition with respect to the initial one is registered. TGA apparatus is reported in Fig 4.7. TGA is always equipped with:

1. a thermic balance;
2. an oven or furnace;
3. a purge gas system that ensures an inert or reactive environment, depending on the case;
4. a computer to monitor the instrument and to acquire data.

In the thermic balance the sample is placed in the oven and it is thermally insulated from external surroundings. A mass variation of the sample is responsible for the deflection of the balance beam: the deflection interposes a shutter between a lamp and one of the two photodiodes. The current intensity variation is then amplified and then sent to a coil placed in a permanent magnet. The magnetic field generated by the current in the coil restores the beam at its original position. The amplified current is then measured and converted in mass or mass variation by the elaboration software. The oven works in the range between room temperature and 1500℃, with a maximum heating

rate of 200℃/minute. Oven insulation from external is needed to avoid any heat transfer to/from the balance. In order to purge the oven and to prevent the sample oxidation it is used nitrogen or argon.
Whenever oxidation phenomena are to be studied, oxygen or air flows can be fed. The presence, in the oven, of an inert atmosphere favors the development of decomposition gas of the sample. The decomposition would be avoided by saturation of the environment. The temperature reported is theoretically the effective temperature of the sample, however the temperature is determined by means of a small thermocouple placed as close as possible to the pan which contains the sample. Therefore, the registered temperature are slightly higher or lower than the real temperature of the sample. Thermobalances have specific systems used to control the temperature.
The information obtained by the TGA are limited with respect to other thermal analysis (DTA, DSC). TGA analysis is limited to phenomena of decomposition, oxidation, solvent evaporation, desorption or sublimation. TGA is however very useful to characterize polymers, because thermogravigrams can provide useful information on decomposition mechanisms and kinetics of molecules. TGA in some cases can be used as tool for molecule recognition. This analysis is generally used to assess the thermal stability of a compound, in this case it is used for different purposes: it is employed to evaluate the distribution of the catalyst, both in absolute value, and in distribution uniformity. In the present work, the instrument adopted is TGA Q600, purchased by TA Instruments.

4.3.3 Gas chromatography coupled with mass spectrometry

Analytical technique of Gas chromatography coupled with mass spectrometry (GC-MS) couples the chromatography analysis (GC) with mass spectrometry (MS). This technique is used to characterize qualitatively and quantitatively a broad range of substances, mainly organics, with low polarity, with low molecular weight and boiling temperature lower than 300℃. Employing MS as detector after chromatography has an intrinsic advantage, since it is possible to identify the examined molecule. The coupling of this two techniques have therefore an analytical capability to separate and identify the substance that is much bigger than the two separate techniques. GC is used to carry on the separation of different chemical species in a gaseous mixture, because of their different properties. As soon as the mixture components are separated, they are transferred to MS, where they

are undergoes to ionization and fragmentation. The main feature of the single analytical technique are here described:

4.3.3.1 Gas chromatography (GC)

Gas chromatography is analytical technique that is used to separate different components of a mixture. With this technique is possible to examine gaseous, liquid and solid samples. The main limitation of this technique, in gaseous phase, is that the component needs to vaporize in a temperature interval between room temperature and 300 ℃, which is the maximum temperature that commercial ovens and injector for GC can achieve. GC is part of the family of chromatography: the principle for which they all work is the repartition of different substances between a stationary and a mobile phase (which is an inert gas, in this case is helium (He)). The repartition is function of the affinity of substances with the two phases. Each compound is distributed in the two phases according to their physical and chemical properties: C_s and C_m are the concentration of the compound respectively in the stationary and mobile phase: taking the ratio it is possible to compute K which is the distribution coefficient which indicates how a substance is distributed between a mobile and stationary phase. From the coefficient K it is possible to compute the retention time, which is the time needed for the compound to go through the entire stationary phase. A high concentration in the stationary phase with respect to the mobile one indicates a major affinity of the compound to the stationary one: the carrier gas (mobile phase) will have some difficulties to drag this component. Other components, with higher affinity to the mobile phase will be dragged steadily from the occupied positions and transferred to the end of the stationary phase (and so to the end of the column). Between stationary phase and mobile phases there are physical and chemical interactions: they are responsible for effective separation of mixture in components: some of that are retained for more time (higher retention time (RT), higher affinity with stationary phase), some other are retained for less time (lower retention time, higher affinity with the mobile phase). The main component of a GC are:

1. one or more injection chamber;
2. one or more columns;
3. a detector.

Injection chamber is employed to ensured instantaneous vaporization of the sample: this is not the case for gaseous samples, however is important for liquid samples that need to be readily vaporized. The injection chamber contains a variable resistance system: with these resistances is possible to vary the temperature, employing the most suitable for vaporize the sample. The employed GC has two different injection modes. The samples can be injected manually by means of a syringe or employing a valve with a volume-fixed gas loop, which works with a rotative pump. In both cases, it is possible to employ a split: just a fraction of the sample enters the column, the remaining part is purged (it is important whenever the signals are saturated). Contrary to injector, the valve has a dead time, before the sample enters the chromatography column. However, the gas loop guarantees that always the same volume of the sample enters the column. In this work a gas loop of 100 μL is employed. In Figure 4.8 are reported the two position of loop valve: in (a) the carrier gas (labeled as 'eluent') enters and exits without passing in the loop: the carriers enter in the column, the loop is in load mode. Then, in (b) the loop is in analysis mode: the sample is injected and carried by eluent and finally transported in the column. The column is constituted by a stationary and a mobile phase. The stationary phase is generally a non-volatile liquid supported on a powder that fills the column (packed column) or distributed as a thin film (width is some microns) on the internal wall of the column (capillary column). The liquid employed is different according to the specific application that is subjected to, for example depends on the compounds that need to be separated. The mobile phase is a gas, labeled as "carrier" or "eluent". The gas employed are normally non-reactive, inert, with low viscosity, high pure (99.9%) as nitrogen or helium. The components of the mixture are separated and retained with different time, function to the affinity of the compounds to the stationary and mobile phases. In order to make the separation more effective, the oven temperature can be varied, maintained constant or according to a temperature-time program.

When the sample exit from the column there is the detector. There are different types of GC detectors: TCD (Thermal Conductivity Detector), FID (Flame Ionization Detector), ECD (Electrons Capture Detector). FID detector is the most employed but destructive: the carrier at the end of the column (which contains also the components to be analyzed) is mixed with air and hydrogen: the mixture is then combusted. The presence of organic molecules in the flame cause the formation of ions that in turn leads to an electric current:

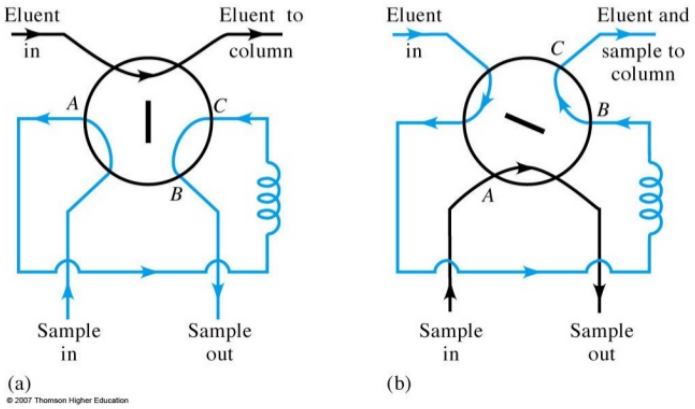

Figure 4.8: Loop injector in GC

the current, amplified represent the detector output signal. The diagram that represents the output, with respect to the time is the sample chromatograph. It is a sequence of peaks of different height and distributed on the time axis. From retention time is possible to infer the identity of the compound, the peaks area or height is a quantitative descriptor of the concentration of the component in the sample.

4.3.3.2 Mass spectrometry (MS)

Mass spectrometry is an analytical technique used to identify and quantify the compounds of the examined sample. It is used to identify the molecular structure (organic, inorganic, biological). The theoretical principle is the separation of a mixture of ions, according to the ratio mass/charge, by means of oscillating or stable magnetic fields. Ions are obtained ionizing the sample molecules, making an impact between gas sample and known-energy beam. Molecules are therefore ionized, and they fragment into smaller ions according to some routes that depend on their chemical structure. The diagram that represents the relative abundance of each ions on y-axis has on x-axis the m/z ratio: it is called mass-spectrum. Each mass-spectrum is the "finger-print" of each molecule: it is related to the chemical structure and to the ionization conditions. Employing specific libraries it is possible to compare the obtained spectrum with spectra of different molecules. Mass spectrometer is composed of three parts:

1. an ionization source

2. an anlyzer for ion separation (quadrupole)

3. a detector

In the injection, the quantity needed to carry on the analysis is few micrograms. In these conditions, the majority of the samples are in gaseous phase, the non-sublimating solids compounds are vaporized by means of ionization coil. If MS is coupled with GC, the exit of the column is the inlet to the MS, via a transfer line. The sample approaches in the MS at the end of the elution in gas phase or after a instantaneous vaporization before the column. Different ionization techniques exist: the system by which ionization is carried out strongly influences the number, the nature, and the abundance of the fragments that are present in the spectrum. In the ionic source, the ions are formed "shooting" the gas molecules with high-energy electron beam (70 eV). The supplied energy and the instability of molecular ions are responsible for molecule cleavage in smaller fragments, positively or negatively charged. At the same time, is not possible to produce both positive and negative ions, and normally one polarity is chosen (normally positive). Molecular ions and fragments are then accelerated and focused by means of a series of lenses and skimmers to quadrupole. This type of analyzer is constituted by four cylindric metals bars, in which ions are separated according to the m/z ratio employing electric fields which can be continuous or radio-frequency alternated. In that way, a portion of ions reaches the detector. The detector is formed by dynodes, electronic multiplicators that can amplify the weak ions current that impacts on the detector. The measure is reported as the ratio to the base peak (the highest peak in the spectrum): in that way, with this normalization, it is possible to register spectrum function only of the analyte and irrespective of the analysis conditions. Employing the calculator is a useful tool because it allows to easily control parameters of the analysis together with the bibliographic research of the spectrum in the spectra library: in this way the compounds identification is automatized. In Figure 4.9 there is the schematic representation of a quadrupole.

4.3.3.3 GC-MS

In this case, when the GC and MS are coupled together, the compound identification is carried in two ways: (1) comparing retention time of the molecules with reference one, (2) employing MS, comparing fragments abundance with library spectra. The spectra are

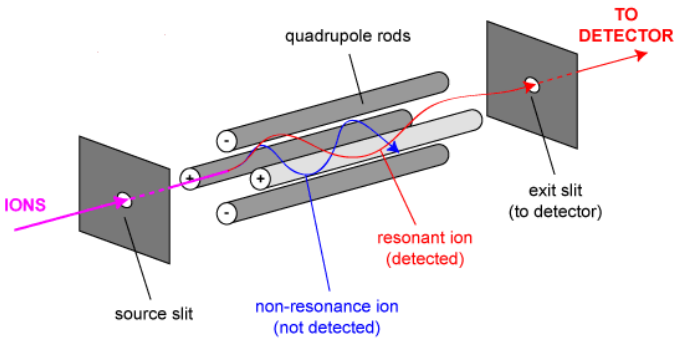

Figure 4.9: MS quadrupole

collected in datasets, in the NIST (*National Institute of Standards and Technology*). GC-MS analysis are carried in full scan mode: mass spectra are registered at defined time intervals. Each peak of the chromatogram corresponds to a specific substance with a well-defined retention time: at each corresponds also a mass spectrum, characteristic for each molecule. An other technique to acquire mass-spectra is employing SIR (*Selected Ion Recording*): the scanning is focused only on some specific m/z values, specific of the analyte. The main advantage of employing SIR technique is that the instrument sensibility increases of 500 times with respect to a full-scan acquisition. In that way it is possible to recognize substance present at very low concentration. Quantitative analysis is carried out integrating the resulting peak.

In this work the instrument employed is TRACE GC 3100 and ISQ Series of Thermo Scientific.The column employed is a capillar column MEGA-1, medium polarity, film width 5.0 μm, internal diameter 0.32 mm, length 30 m. The acquisition is carried out both in Full Scane mode, and in SIR mode to carry out the quantitative analysis.

4.3.4 X-ray diffraction (XRD)

This technique exploits the effects that the interaction between the sample and the electromagnetic radiation are able to cause. Radiation, indeed, can interact with the matter in two different ways: the first is radiation absorption where a part of the energy of the radiation is adsorbed by the sample, leading to a temperature rise or a transition to an excited state; the second mechanism is the scattering: the incident radiation is diffused by the sample, the magnetic waves varies their propagation direction. XRD uses the elastic coherent scattering, which can be thought as the sum of all the electromagnetic waves

that are scattered from atoms that lay on the same family of reticular planes. Preferentially, the analysis is carried out with samples that exhibit a crystalline structure.
According to the nature of the sample, different techniques can be recognized: SC-XRD: single crystal X-ray diffraction, XR-PD: X-ray powder diffraction: both they are non-destructive methods. The obtained result is the so-called diffraction spectrum: on the x-axis there is angle of diffraction (2θ), while y-axis reports the peaks intensity.

4.3.5 Diffuse UV-Vis reflectance spectrometry (DRS)

This analytical technique is used to investigate the absorption properties of the samples: the band gaps can therefore be assessed. The absorption wavelength is the bigger wavelength at which radiation absorption occurs. Diffuse reflectance is not specular: the incident beam is not diffuse at a specific angle; indeed it is diffuse along multiple random direction. The sample must have a thickness that favors absorption or total diffusion, before the beam exits on the opposite side of the specimen. The sample absorbs some portion of the incident light and therefore the intensity of the diffuse radiation will be lower. The result are arranged in a spectrum: x-axis is the wavelength, while in the y-axis there is absorbance (or transmittance). The measure is done measuring, as first sample, the spectrum of a total reflecting material (barium sulphate, $BaSO_4$). This is the blank sample, since it has a reflectance in the visible range next to 100%.

Chapter 5

Preparation and characterization of membranes

In this chapter, the preparation and the analytical characterization of the electrospun membranes are carried out.

5.1 Catalysts synthesis

Before analyzing the preparation of the membranes, it is worth to, at least mention, the chemical routes to synthetize the catalysts. They are prepared according two different routes (mechano-chemical synthesis and top-down process):

5.1.1 Mechano-chemical route

The synthesis of catalysts 2, 3, 7, 8 of Table 4.2 is performed in the University of Udine. CeO_2 was prepared by moderate calcination (200℃) of cerium carbonate obtained from $Ce(NO_3)$ by precipitation with NH_4HCO_3. Improved contact between graphene and catalyst (CeO_2 or TiO_2) was achieved in a mill. The employed mill is a Mini-Mill (Pulverisette 23 from Fritsch). This mill can be used for fine comminution of small quantities of medium-hard, brittle and moist, wet, dry samples. Its spherical grinding bowl ensures a good performance in grinding, mixing and homogenizing the powders: the spherical shape perfectly adapts to the comminution principle. The sample inside the mill is grinded through impact and friction between grinding balls and the inside wall

(a) *Mini Mill Pulverisette 23 from Fritsch.*

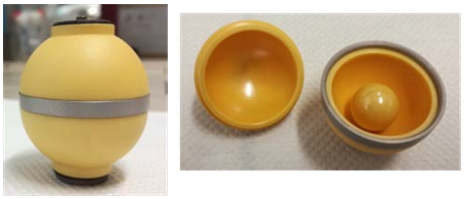

(b) *Zirconia jar and ball mill.*

Figure 5.1: Mill equipment

of the grinding bowl. The grinding bowl performs vertically oscillating movements with 900-3000 oscillation per minute at 9 mm amplitude. The Mill is reported in Fig. 5.1a.

The Mill is equipped with a zirconia ball (d=10 mm) and a 15 mL zirconia jar. In a typical experiment 1 g of ceria (or titania) particles were milled with 0.1 g of graphene. The milling time was set from 2 minutes to 8 h with a oscillation frequency of 50Hz. The experimental setup (the jar and the grinding ball is reported in Fig. 5.1b.

5.1.2 Top-down route

Hypergraph composite powder is obtained with a process that chemically combines the metal oxide and the graphite according to the ”top-down process”. Employing this method, the morphology and the physical properties of the materials are changed but the route gives rise to a chemical interaction among them. This route is very flexible, since by varying the employed oxide and the composition ratio (oxide : graphene), it is possible to obtain different properties of the final powder. The oxide can be functionalized or doped before the process to yield a composite powder that has different degree of doping, beside its intrinsic oxide : graphene ratio. Therefore, top-down route can yield a wide spectrum of composite powders with different chemical-physical properties.
The catalyst obtained with this procedure are 4-5 in Table 4.2, they are synthetized by a private Company.

5.2 Nanocomposite characterization

5.2.1 UV-Vis Diffuse Reflectance Spectroscopy (DRS)

Employing UV-Vis spectroscopy is an useful tool to study the absorption range and the band gap of semiconductor photocatalysts. The results of the analysis are reported in function of the radiation wavelength (expressed in nm) on the x-axis, while y-axis is the absorbance of the catalyst, Figure 5.2. The typical plot has both linear and non-linear zones. Absorbance limit is computed, drawing the line that better approximates the linear portion of the plot and calculating the intersection of the line with x-axis. The shape of the two curves (blue is catalyst TiO_2 Graphene 10:1, while red is "pure" CeO_2) is similar and compatible to previous works. The tangent that better approximates the linear portion is drawn: the absolute value on the x-axis (which represents the absorbance limit of the semiconductor) cannot be used as a reliable information, due to some instrumental difficulties observed during the preparation and the analysis of the samples.

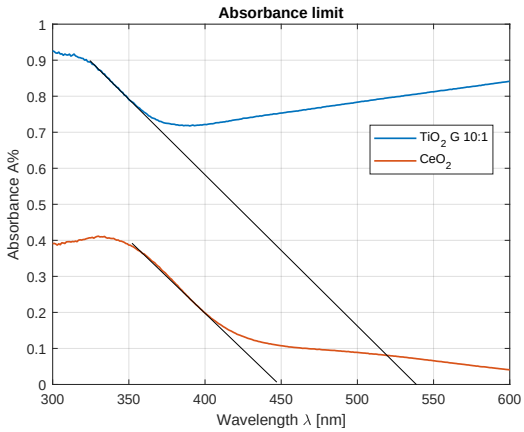

Figure 5.2: Absorbance limits determination of TiO_2 G 10:1 (blue) and CeO_2 (red) catalysts

The calculation of the band gap is carried out in the same theoretical way: the plot and the functions are different. From absorbance (A), it is possible to calculate reflectance (R) employing the relationship:

$$R = \left(\frac{1}{10}\right)^{A} \tag{5.1}$$

Kubelka-Munk model can be build, according to the following equation, when the reflectance is known:

$$F(R) = \frac{(1-R)^2}{R} \tag{5.2}$$

In this application a modified Kubelka-Munk function is employed:

$$(F(R)h\nu)^n \tag{5.3}$$

in which h is the Plank constant, ν is the radiation frequency, n is a coefficient related to electronic transition of the sample. The obtained plot (Fig. 5.3) has on the x-axis the energy of the radiation ($E = h\nu$, expressed in $[eV]$), while the y-axis is the modified-Kubelka-Munk equation (Eq. 5.3), with coefficient n equal to 0.5. The band gap is given with the intersection on the x-axis with the line that better approximates the linear portion of the curve. Also in this case, the shape of the modified Kubelka-Munk function is similar to previous work, however the absolute value of the band gap can not be employed, due to some problems in the analytical technique

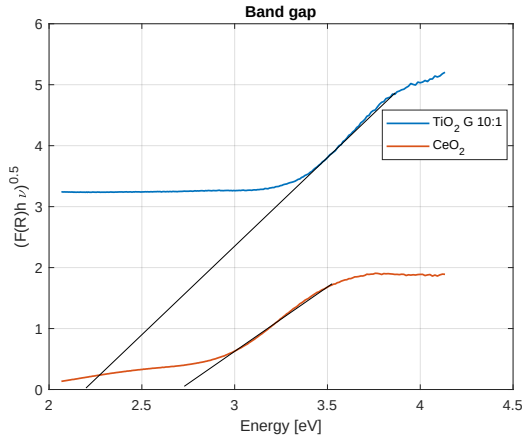

Figure 5.3: Band gaps determination of TiO_2 G 10:1 (blue) and CeO_2 (red) catalysts

5.2.2 SEM characterization

Catalysts have been characterized with ESEM (*Environmental Scanning Electron Microscope*). The aggregate dimensions are calculated by means of the software ImageJ.

From Fig.5.4a it is possible to see the homogeneous porous structure of the titania, which gives rise to the high specific surface: the mean diameter of the aggregates is 307 nm, SD (standard deviation) 72 nm.

Unlike ”pure” titania, the other catalysts, have a more broad particle size distribution,

ranging from 900 nm to few dozens of microns. The sample 5.4b and 5.4c are formed by titania and graphene photocatalysts, obtained via mechano-chemical synthesis. Comparing the two images, it is possible to see that some big aggregates are present in the sample milled for 2 hours (the biggest aggregate has a dimension of 38 μm, while the mean diameter of the finer fraction is 1.26 μm, SD 0.43), while the catalyst milled for 8 hours displays a finer structure (mean diameter of the finer fraction 0.980 μm, SD 0.45). The same behavior is found comparing the sample of ceria-titania milled for 2 hours and the one milled for 8 hours (respectively, Fig. 5.4h (mean diameter 3.14, μm, SD 1.5) and 5.4i (mean diameter 1.27 μm, SD 0.43): the specific area is much bigger, also with respect to the sample in Fig. 5.4g in which ceria and graphene are simply mixed and not milled together (mean diameter 3.81 μm, SD 1.02). It is possible to infer that a longer milling time leads to smaller, finer nanoparticles.
Ceria (Fig. 5.4f) nanoparticles have different shape with respect to titania. The shape is less regular, and more acicular with respect to titania particles, the average dimension is 2.01 μm. The samples in Fig. 5.4d-5.4e are the nanoparticles obtained via top-down process, varying the proportion between titania and graphene: their average diameter are respectively 2.11, SD 0.75 and 1.435 μm, SD 0.51.

5.2.3 EDX analysis

The spectroscopy EDX (Energy Dispersive X-ray Analysis) is used to characterize cerium dioxide catalyst. The result is reported in Fig. 5.5, confirming the presence of CeO_2 nanoparticles.

5.3 Membrane preparation

Membranes are prepared according the ”two step approach”. With this method, the polymeric membrane is first electrospun, and then the catalyst is electrosprayed on the polymer. In this way, the catalyst is deposited only on the illuminated surface, and it is not deposited on the membrane bulk. The other approach for preparing photocatalytic membranes is according to ”in mass” principle. The polymer and the catalyst are dissolved in a proper solvent that is able to solubilize/disperse both, and then the resulting solution is electrospun. Employing this approach, the membrane formation is faster; however,

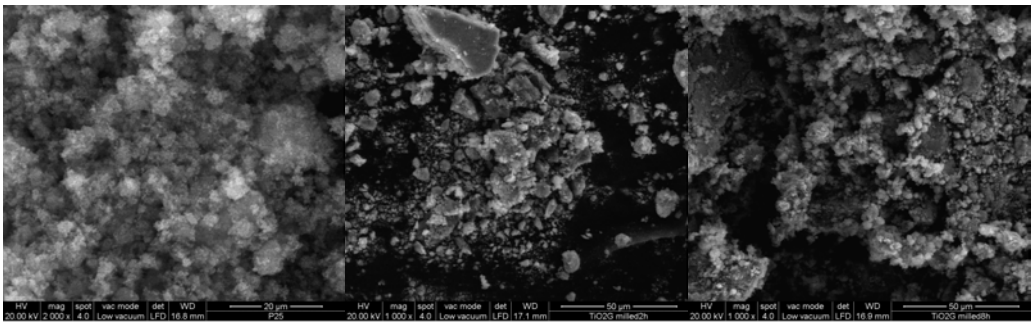

(a) *TiO_2 Degussa P25.* **(b)** *TiO_2 Graphene, milled for 2h.* **(c)** *TiO_2 Graphene, milled for 8h.*

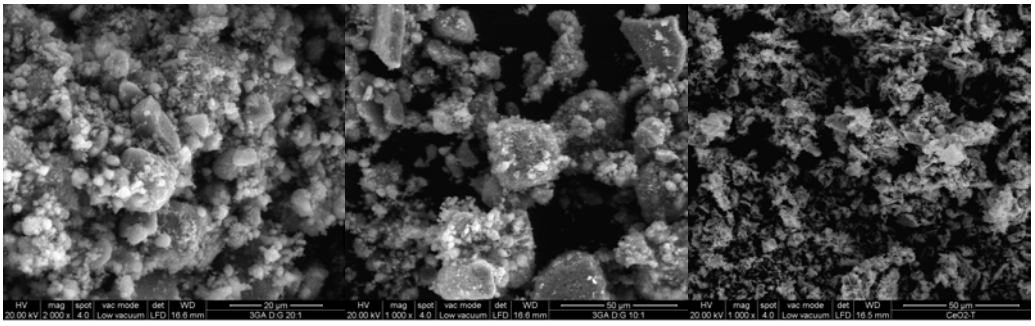

(d) *TiO_2 Graphene 20:1.* **(e)** *TiO_2 Graphene 10:1.* **(f)** *CeO_2-T.*

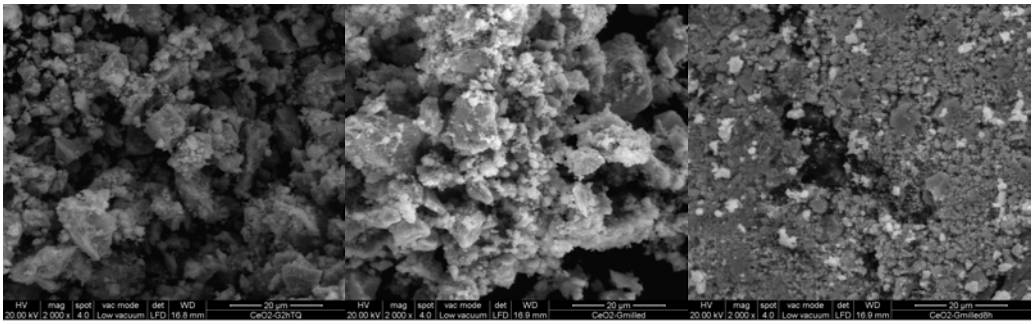

(g) *CeO_2-T Graphene.* **(h)** *CeO_2-T Graphene milled for 2h.* **(i)** *CeO_2-T Graphene milled for 8h.*

Figure 5.4: Catalyst ESEM characterization

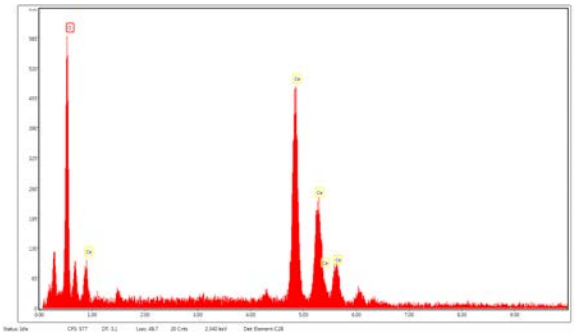

Figure 5.5: CeO_2 powder EDX characterization

Table 5.1: Process conditions for electrospinning and electrospraying

Process	Voltage [kV]	Flowrate [mL/h]	Needle-collector distance [cm]	Needle internal diameter [mm]
PAN in DMF (electrospinning)	15	0.5	15	27G 0.4 mm
catalyst in EtOH (electrospraying)	15	8	15	18G 1.2 mm

the catalyst is dispersed both on the illuminated surface and on the membrane bulk. The preparation of the membrane and the subsequent deposition of the catalyst are described in the following two sections:

5.3.1 Electrospinning

Polyacrylonitrile (5% wt.) is dissolved in DMF: the polymer dissolution is favored by magnetic stirring: 1 hour at 50℃, 12 hours at room temperature. After 13 hours of stirring, the solution is loaded on the syringe and the electrospinning process is carried out. The temperature is the ambient temperature of the electrospinning box (20℃-24℃), while the relative humidity is maintained at low values (30-35%) employing compressed air flow, to decrease the water content in the box. The collector rotates clockwise with a frequency of 3200 rpm. The employed equipment is the one displayed in Fig.4.5. The process condition for electrospinning are reported in the first row of Table 5.1.

To obtain a good coverage, the electrospinning process lasts 18 hours for each membrane.

Furthermore, the otpimization of electrospinning ”in mass” mode is carried out. The optimal flowrate has been chosen, according to the assessment by means of SEM of the morphology of the resulting fibers. The electrospinning is carried out, in ”mass approach” at three different flow rates, respectively at 0.5, 1, 2 mL/h. The white round-like aggregates present on the fibers are formed by titania nanoparticles. Making a comparison, it is possible to infer that when the flow rate is low, the fibers result much more oriented,

due to the rotating movement of the collector. The diameter is smaller in the case of lower flow rate, and the aggregate diameter is smaller, with a higher specific surface. For these reasons, the optimized flowrate is 0.5 mL/h.

5.3.2 Electrospraying

The catalysts (5% wt.) is dispersed in ethanol: the dispersion is favored employing sonication equipment. A typical composition of the solution is: 1 g of the catalyst, 19 g of ethanol. The sonication is carried out for 40 minutes (cycles of 59 seconds on and 20 seconds off, maximum amplitude 40%). Then, the dispersant agent is added to the solution (0.019 g of Dynasylan 4144 (1% with respect to the solvent weight)): a further sonication is carried out for 20 minutes (cycles of 59 seconds on and 20 seconds off, maximum amplitude 40%). Then, the solution is loaded in the syringe and the electrospraying process is carried out according to the process conditions reported in the second row of the Table 5.1. It is worth to notice that the flowrate is much higher with respect to electrospinning process: this value has been optimized in previous works. The internal diameter of the needle of the syringe is bigger in this case, since the solution has some nanoparticles dispersed in the liquid medium.
Different strategies are taken into account to disperse the catalyst in the most homogeneous way. One of these methods it to cover alternately 2 parts of the collector with a Teflon sheet and deposit the catalyst on the third part (which is not covered). Then, the sheet is removed and placed on other two places. However, the electrospinning jet is intrinsically non oriented in a specific direction, but the deposition occurs also on the Teflon sheet, leading to a ”waste” of catalyst. For that reason, the electrospinning is carried out in three-hour time, moving the volumetric pump each hour, from the bottom, to the central, up to upper portion of the rotating drum.

The polymeric membrane is not deposited directly on the collector, since there is the need to have a mesh that is able to provide to the membrane the stability and to easily displace the membrane from the rotating drum to the reactor.
Several meshes are tested. The main feature of the meshes are: (i) they do not have to

participate to the chemical reaction, (ii) they need to be stable under UV irradiation, (iii) they favor the membrane-support coupling, (iv) they must have open pores, to favor the gas flow rate and to decrease the pressure drops during work, (vi) they have to provide mechanical support to the membrane, and eventually (vii) their employment and manipulation should be easy.

Different meshes are tested: the first one in aluminum has big pore size, however it is too stiff and the aluminum wires can cause membrane breakage. The second one is made by polyester fabric, which is not able to guarantee mechanical stability and has a very small pore size, causing high pressure drops. The chosen mesh is a plastic mesh (PVC), with rectangular holes (1x2 mm), which fulfils to the requirements above-mentioned. The membrane deposited on the plastic mesh can be seen in Figure 5.6a. The gray color is due to the presence of graphene on the surface. The electrospun membrane is then covered with another plastic mesh, which constitutes a scaffold for the membrane, to yield a ”hamburger-like” structure: the membrane is placed inside two plastic meshes that gives the mechanical stability and allows the insertion in the reactor. This structure is rolled employing a cylinder (external dimeter 4 cm) and the two edges of the meshes are welded employing hot glue. In that way, the catalyst looks out over the inner side of the membrane (i.e. the one exposed to irradiation). The same membrane of Fig. 5.6a is displayed in Fig. 5.6b in a rolled arrangement: it is worth to notice that, despite the white color on the external surface (due to the PAN fibers), the catalyst is loaded on the internal surface (which is subjected to UV irradiation).

In this work, eight membranes are prepared with eight catalysts: the catalysts are listed in Table 5.2. When the catalyst weight is low, it is added to titania P25 to yield a total weight of 1000 mg.

5.4 Membrane characterization

Membranes, after use, have been characterized employing XRD, SEM and TGA. TGA employs a temperature-time program: ramp from room temperature to 910℃ with an increment of 20℃/min. TGA is employed to calculate the concentration of the catalyst on the membrane, calculating the residue of the sample at high temperature: at this temperature, indeed, the organic part decomposes, leaving only the inorganic portion.

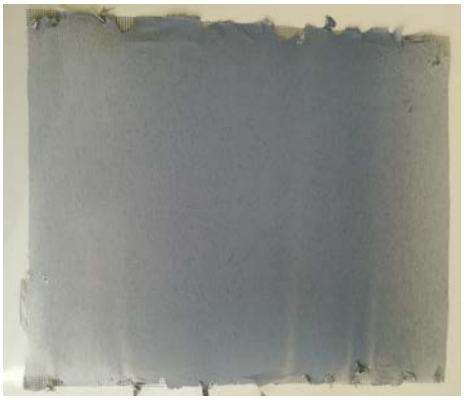

(a) *Membrane deposited on a plastic mesh.*

(b) *Membrane rolled up on two plastic meshes.*

Figure 5.6: Photocatalytic membrane before and after being rolled up

Table 5.2: Catalysts deposited on membranes

n.	Catalysts	Weight [mg]	Added TiO_2 Weight [mg]
1	TiO_2 P25	1000	0
2	TiO_2 Graphene milled 2h	300	700
3	TiO_2 Graphene milled 8h	1000	0
4	TiO_2:Graphene 20:1	1340	0
5	TiO_2:Graphene 10:1	1250	0
6	TiO_2/CeO_2-T Graphene mixed 2h	300	700
7	TiO_2/CeO_2-T Graphene milled 2h	300	700
8	CeO_2-T Graphene milled 8h	1000	0

To assess the homogeneity of the catalyst distribution on the fibers, the membranes (after use) are sampled, cutting 3/4 slices of 15/20 cm^2 each. TGA results then are overlaid to evaluate the homogeneity of the residue. The results of the analysis are reported in the following sections:

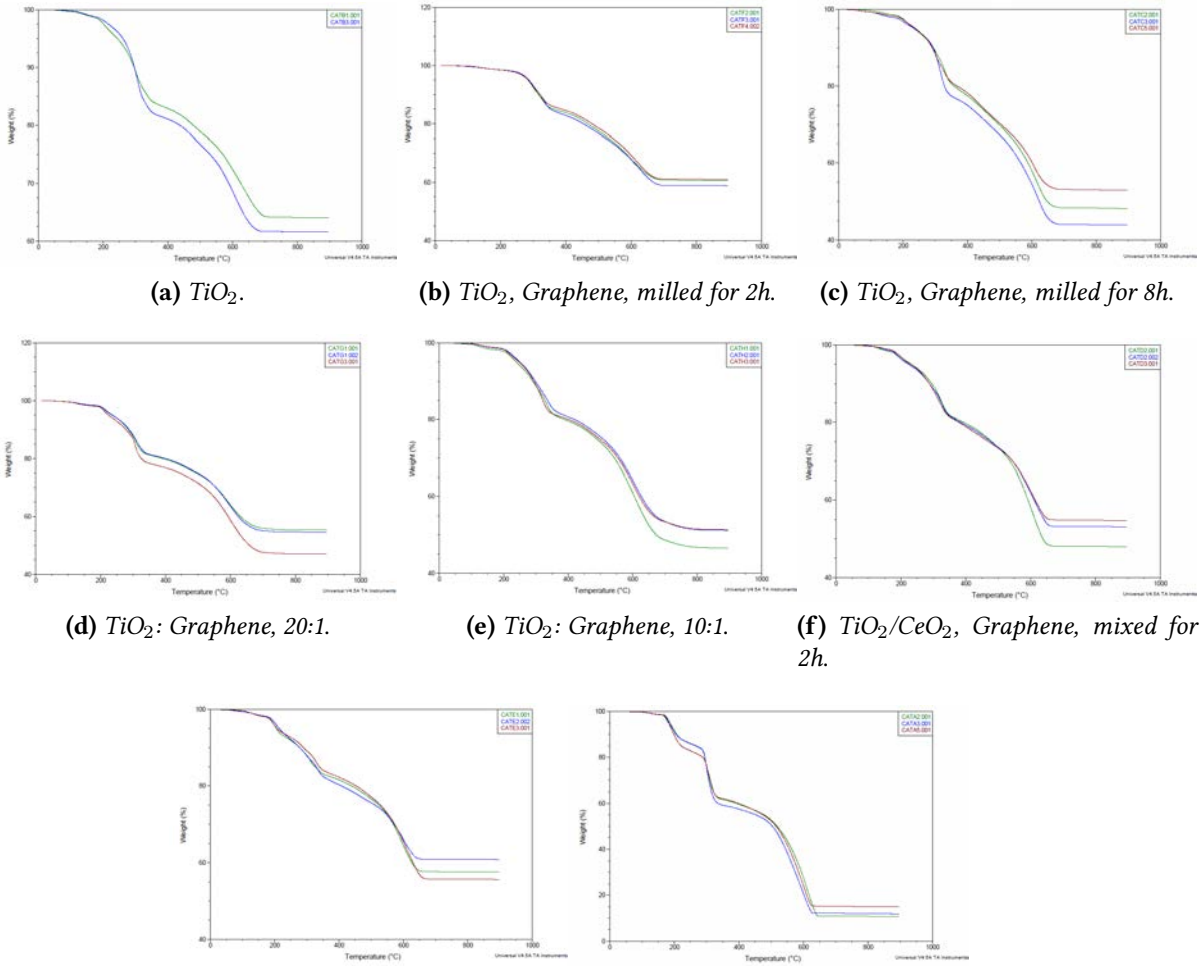

(a) *TiO_2.* **(b)** *TiO_2, Graphene, milled for 2h.* **(c)** *TiO_2, Graphene, milled for 8h.*

(d) *TiO_2: Graphene, 20:1.* **(e)** *TiO_2: Graphene, 10:1.* **(f)** *TiO_2/CeO_2, Graphene, mixed for 2h.*

(g) *TiO_2CeO_2, Graphene, milled for 2h.* **(h)** *CeO_2, Graphene, milled for 8h.*

Figure 5.7: Thermogravimetric analysis of the membranes

5.4.1 TiO_2

The membrane with TiO_2 P25 is characterized by means of TGA and SEM. TGA result is reported in Fig.5.7a. TGA plot shows a non-perfectly uniform deposition on the surface, due to very large surface that the electrospinning jet needs to cover, (the residues are not perfectly overlaid). The mean catalyst weight fraction is 67.63% of the total weight, which leads to a concentration of catalyst per surface area of 1.043 mg/cm^2. The membrane area

illuminated by the radiation, assuming a cylinder of diameter 4 cm and height 21.5 cm (the construction geometrical details are reported in the next Chapter) is therefore 270.2 cm^2. So, the total catalyst loading is 281.8 mg. The catalyst concentration is high with respect to other works (*Lauria A. M.*) in which the catalyst per surface was in the range of (0.5-0.8) mg/cm^2.

XRD pattern of TiO_2 P25 is represented in Fig. 5.8. The peaks at 2θ values of 25.3, 37.8, 48.0, 53.9, 55.1, 62.7, 68.8, 70.3 and 75.0 can be indexed to the (101), (004), (200), (105), (211), (204), (116), (220) and (215) crystal planes of anatase (JCPDS card n 71-166). In addition, also the characteristic diffraction peaks of rutile (JCPDS card n 05-4165) at 27.4, 36.1, 41.2 are observed, which correspond to the (110), (101) and (111) faces of rutile in TiO_2.

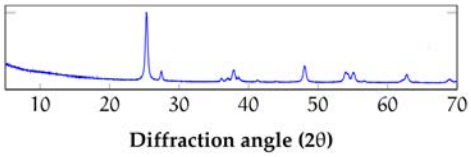

Figure 5.8: XRD pattern of TiO_2 P25

5.4.2 TiO_2 Graphene, milled for 2h

Due to the very small amount of catalyst available, the catalyst is added with titania P25, to give a total weight of 1000 mg. The membrane is characterized with TGA: the results are reported in Fig. 5.7b. From the plot, it can be seen that the distribution of the catalyst over the membrane is uniform (the residue composition in the three different membrane slices is similar), resulting in a weight fraction of 60%, a catalyst density of 1.25 mg/cm^2 and a total catalyst concentration of 337.5 mg. The XRD analysis is reported in Fig. 5.9: the co-presence of anatase and rutile are pointed out, while graphene is not revealed.

5.4.3 TiO_2 Graphene, milled for 8h

The membrane is characterized by TGA: the results are reported in Fig. 5.7c. In this case, the catalyst is not uniformly distributed on the surface: the mean weight fraction is 48%,

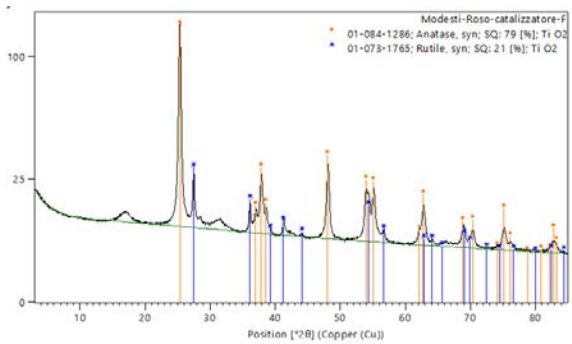

Figure 5.9: XRD pattern of TiO_2 Graphene, milled for 2h

the catalyst per unit surface is 0.792 mg/cm^2, resulting in an overall weight of 214 mg.

XRD analysis is reported in Fig. 5.10: the peaks correspond to the presence of anatase and rutile.

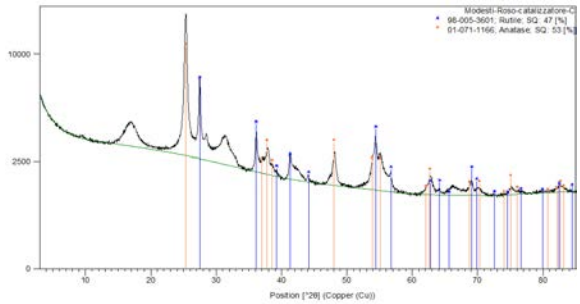

Figure 5.10: XRD pattern of membrane with TiO_2, Graphene, milled for 8h

The membrane is characterized also by means of SEM: the results are reported in Fig. 5.11a-5.11b: the catalyst is aggregated in big clusters (up to 10 µm on diameter) on the electrospun fibers.

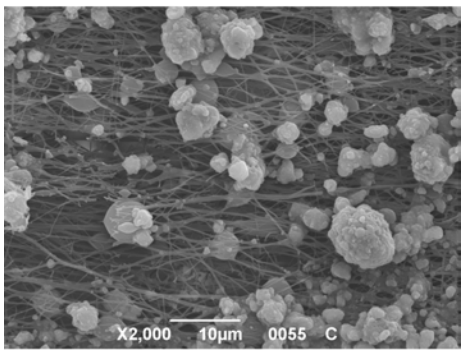

(a) *Nanofibers and the catalyst.*

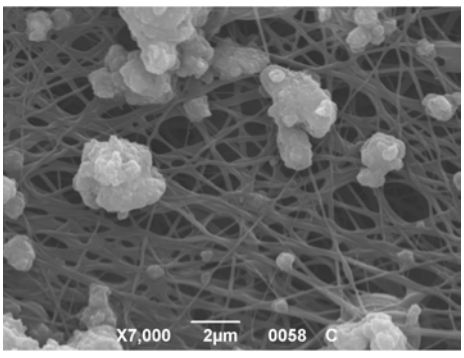

(b) *Particular of the fibers.*

Figure 5.11: SEM of membrane with TiO_2, Graphene, milled for 8h

5.4.4 TiO_2 : Graphene 20:1

This membrane is characterized by TGA: the results are reported in Fig. 5.7d. The medium percentual content is 52.57%, with a concentration of 0.77 mg/cm^2, leading to an overall content of 208 mg. Figure 5.12 is the XRD pattern of this membrane: anatase and rutile peaks are found.

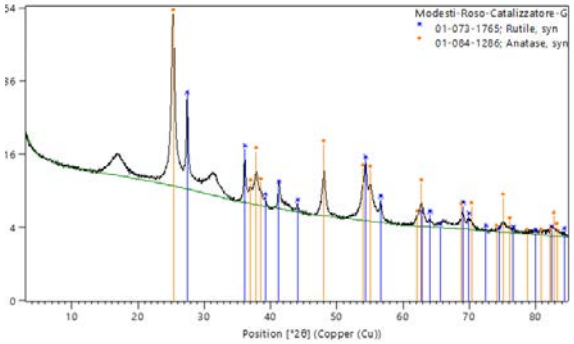

Figure 5.12: XRD pattern of membrane with TiO_2 : Graphene 20:1

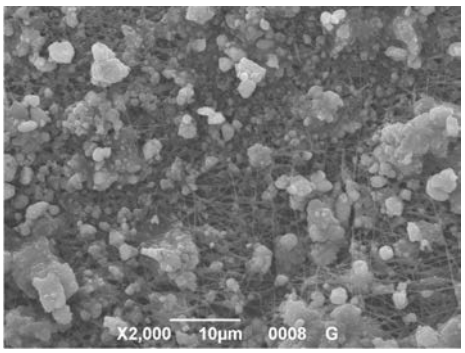

(a) *Nanofibers and the catalyst.*

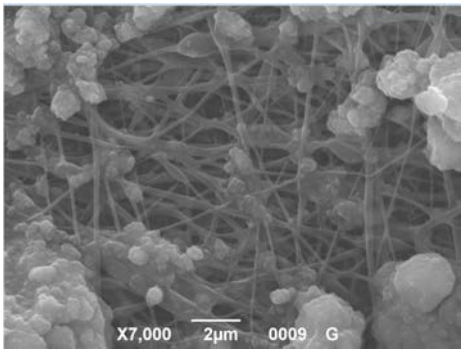

(b) *Particular of the fibers.*

Figure 5.13: SEM of membrane with TiO_2 : Graphene 20:1

SEM results are displayed in Figure 5.13a-5.13b. Looking at Fig. 5.13a it is clear that the catalyst loading is high: this information is confirmed also by TGA. There is a high concentration of the catalyst that partially covers the fibers (Fig. 5.13a).

5.4.5 TiO_2 : Graphene 10:1

This membrane is characterized by TGA: the results are reported in Fig. 5.7e. The medium percentual content is 49.94%, with a concentration of 0.634 mg/cm^2, leading to an overall content of 171.3 mg. XRD pattern is represented in Fig. 5.14. Beside anatase and rutile, in this sample, XRD reveals a small amount of graphite (semi-quantitative analysis, graphite concentration: 5%).

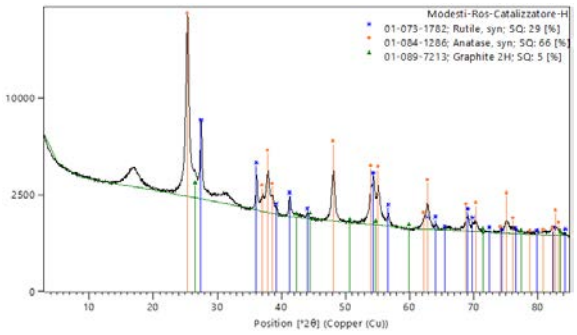

Figure 5.14: XRD pattern of membrane with TiO_2 : Graphene 10:1

5.4.6 TiO_2/CeO_2 Graphene, mixed for 2h

Due to the very small amount of catalyst available, the catalyst is added with titania P25, to yield an overall weight of 1000 mg. The membrane is characterized by TGA: the results are reported in Fig. 5.7f.

Also in this case the concentration of the catalyst is not completely homogeneous on the surface. The mean catalyst weight fraction is 54.27% of the total weight, which leads to a concentration of catalyst per surface area of 0.985 mg/cm^2, and an overall weight of 266 mg. Also in this case, because of the excessive loading, the catalyst fully covers the fibers. XRD pattern is displayed in Fig. 5.15: the peaks of rutile and anatase are present.

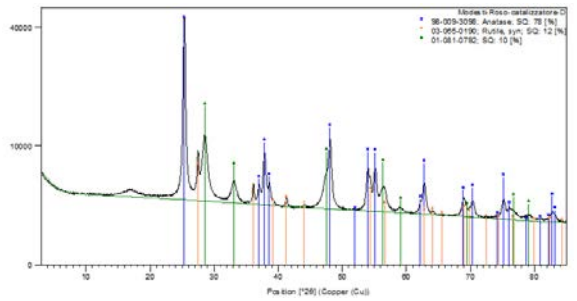

Figure 5.15: XRD pattern of membrane with TiO_2/CeO_2 Graphene, mixed for 2h

5.4.7 TiO_2/CeO_2 Graphene, milled for 2h

Due to the very small amount of catalyst available, the catalyst is added with titania P25, to yield a total weight of 1000 mg. The membrane is characterized by TGA: the results are reported in Fig. 5.7g.

Also in this case the concentration of the catalyst is not completely homogeneous on the surface. The mean catalyst weight fraction is 57.5% of the total weight, which leads

to a concentration of catalyst per surface area of 0.9125 mg/cm^2, and an overall weight of 246.6 mg.

XRD analysis is reported in Fig. 5.16. From this analysis the co-presence of cerium dioxide and the two crystalline phases of titania (anatase and rutile) are found. Furthermore, the presence of a fourth species (Ce_2O_3) is highlighted.

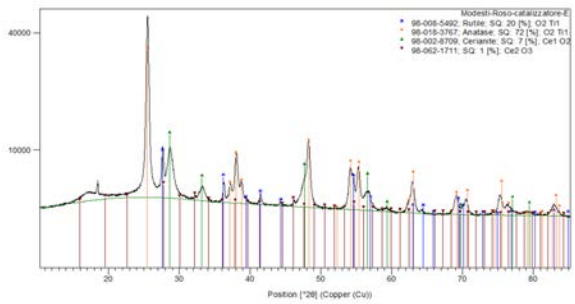

Figure 5.16: XRD pattern of membrane with TiO_2/CeO_2 Graphene, milled for 2h

SEM images are reported in Fig. 5.17a-5.17b: on the right-hand side of Fig. 5.17a a big aggregate is present, formed by the catalyst: it therefore covers the electrospun fibers. On the right hand side some fibrous structure appear: Fig. 5.17b is a magnification of the fibers.

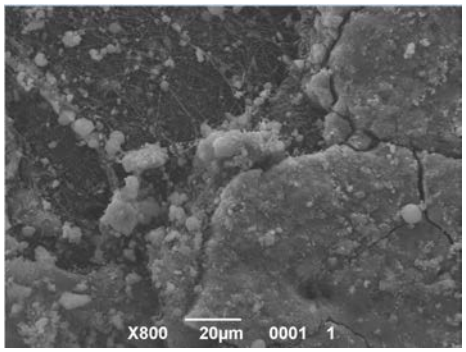

(a) *Nanofibers and the catalyst.*

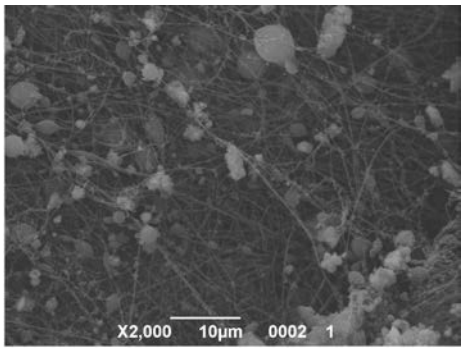

(b) *Particular of the fibers.*

Figure 5.17: SEM of membrane with TiO_2/CeO_2 Graphene, milled for 2h

5.4.8 CeO_2 Graphene, milled for 8h

The membrane is characterized by TGA: the results are reported in Fig. 5.7h.

In this case the content of catalyst is homogenous in the surface. The mean catalyst weight fraction is 12% of the total weight, which leads to a concentration of catalyst per surface area of 0.1204 mg/cm^2, and an overall weight of 32.53 mg. In this case, the catalyst

content is very low. SEM images are reported in Fig. 5.18a-5.18b: the images confirm the low quantity of catalyst dispersed on the polymeric fibers. In this case, the low quantity of the catalyst on the membrane can be due to the non-effective dispersion of the catalyst on the solvent.

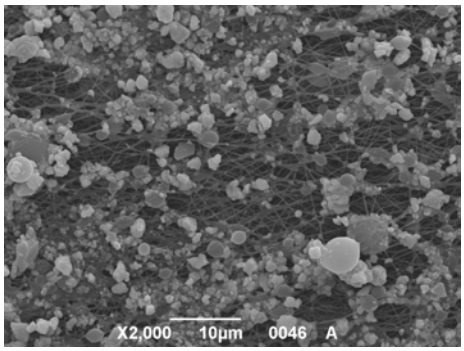

(a) *Nanofibers and the catalyst.*

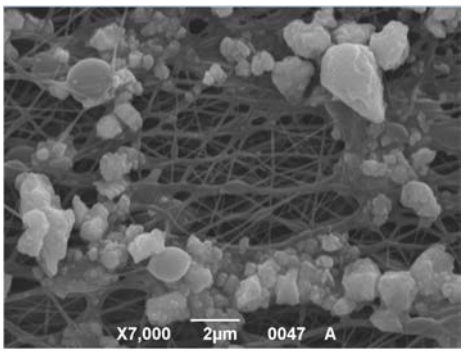

(b) *Particular of the fibers.*

Figure 5.18: SEM of membrane with CeO_2, Graphene, milled for 8h

XRD analysis is represented also in Fig. 5.19. Also in this case the graphene is not detected, only cerium dioxide is detected.

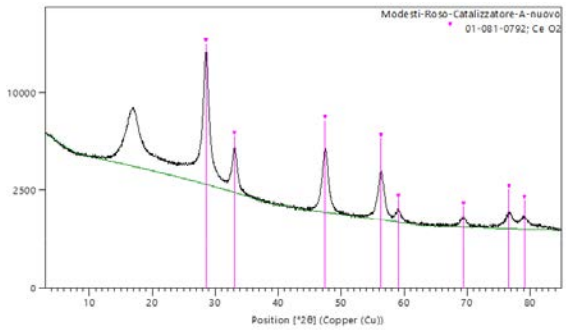

Figure 5.19: XRD pattern of membrane with CeO_2 Graphene, milled for 8 h

XRD reveals for samples TiO_2 G milled for 2 and 8 hours and for the samples TiO_2 G 10:1 and 20:1 the presence of an amorphous phase, which is responsible for large peaks at 2θ=31, 42: it is not possible to determine the chemical composition.
From morphological viewpoint, the narrower size distribution and the finer particle dimension is given by pure titania, whereas other catalysts display a broader distribution, with aggregates whose dimension can reach 30 µm. As final remarks, it is worth to say

Table 5.3: Catalysts content of membranes

n.	Catalysts	Catalyst content [mg]
1	TiO_2 P25	281.8
2	TiO_2 Graphene milled 2h	337.5
3	TiO_2 Graphene milled 8h	214
4	TiO_2:Graphene 20:1	208
5	TiO_2:Graphene 10:1	171.3
6	TiO_2/CeO_2-T Graphene mixed 2h	266
7	TiO_2/CeO_2-T Graphene milled 2h	246.6
8	CeO_2-T Graphene milled 8h	32.53

that the electrospinning process, considering the actual setup, is not able to guarantee a perfect catalyst distribution homogeneity over a so large surface. Furthermore, specific dispersant agents are to be found to better disperse cerium dioxide and graphene in ethanol. The catalyst content for each membrane is reported in Table 5.3.

Chapter 6

Photo-catalytic oxidation of methanol

In this Chapter the photo-catalytic performances of the membranes characterized in the previous Chapter are discussed. The first part deals with the reactor design and the lab-scale plant used to test the membrane, the second part refers to the tests of the membranes in the oxidation of methanol.

6.1 Lab-scale Plant

The lab-scale plant used to perform catalytic oxidation of methanol is here described: a simplified graphical representation is reported in Fig. 6.1. The experimental lab-scale plant is reported in Fig. 6.2

Technical air from the tank is controlled via a digital flowmeter and controller Bronkhorst. With this controller, it is possible to modulate the air flowrate that enters the plant: the range is 0-500 mL/min. The ”clean” air is polluted when it enters in a specific cell (similar to an Arnold diffusive cell), in which the liquid pollutant is stored. The cell is maintained at 0℃ by means of a melting ice bath, in order to decrease its vapor partial pressure. The ”clean” air strips the vapor fraction of methanol that is able to evaporate and then, before entering the reactor, flows across a flowmeter indicator. The polluted streams enter the reactor (the reactor is fully described in the following section). By switching two valves, the reactor can be run either continuously or batchwise.
If the reactor works continuously the outlet from the reactor is simply purged; otherwise a recycling pump is used to maintain the reactor in a batchwise mode: in this case, the outlet of the reactor is recirculated as the reactor inlet, in order to give the pollutant more

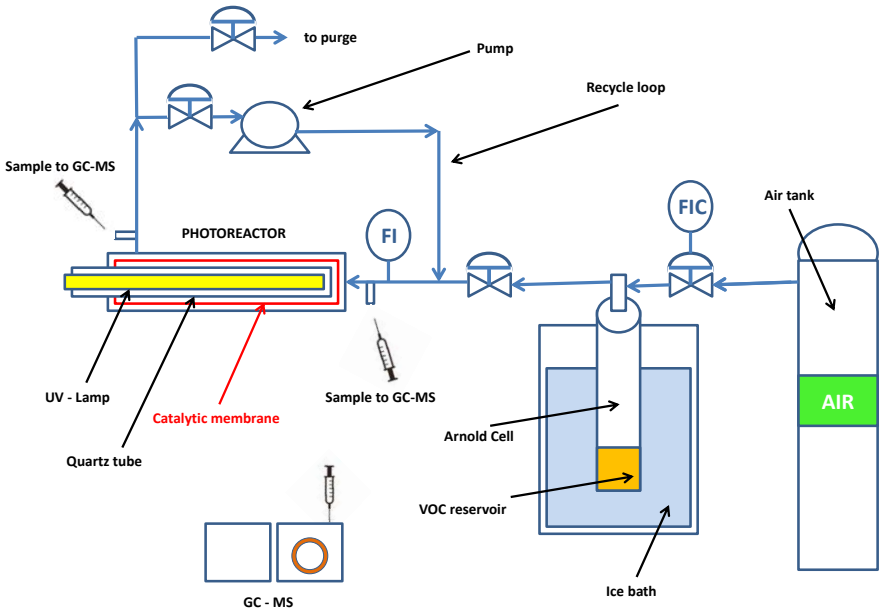

Figure 6.1: Schematic representation of the photocatalytic lab-scale plant

time to react.

6.1.1 Photoreactor

The photoreactor is designed according to a geometrical similarity. In previous works (*Lauria A. M.*, et al., 2016) a different photoreactor was adopted. In this "old" photoreactor, the UV-lamp is placed in the middle of the reactor, and the membranes are arranged in a sort of scaffold: membranes are of annulus shape, the center is occupied by the UV-lamp. In the present reactor, instead, the single membrane is arranged in a coaxial arrangement, with respect to the lamp: therefore, the irradiance is maximized. In the old reactor the scaffold was constituted of 5 membranes, with external diameter 10 cm, internal diameter 4, leading to a surface of 66 cm^2/membrane: the overall area is 330 cm^2. The same area is obtained in the "new" reactor employing a single membrane with diameter 4 cm and height 26.7 cm (surface: 335 cm^2). The membrane placed inside the two plastic meshes is inserted and welded in two membrane-holders. The supports have a diameter of 4 cm and a height respectively of 2.55 and 2.65 cm. Therefore, the useful area needs to be recomputed, subtracting the area of the two membrane holders, and leads to 270 cm^2. One of the two membrane holders has a hole, which enables the insertion of a quartz tube in which the UV-lamp is inserted.

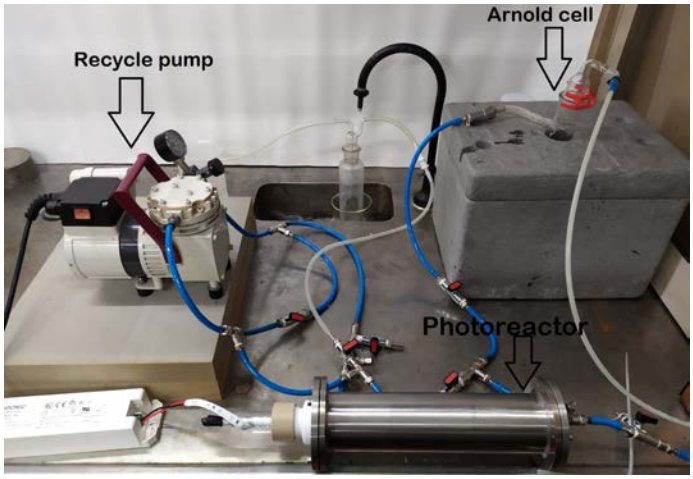

Figure 6.2: Photocatalytic lab-scale plant

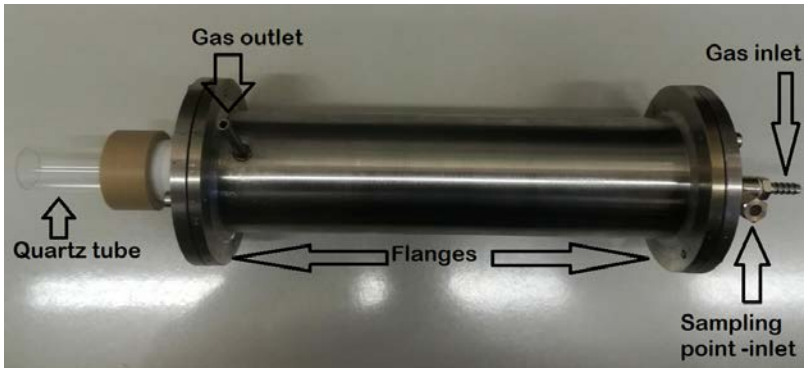

Figure 6.3: Photoreactor

The reactor is made in stainless steel (Fig. 6.3). The geometrical features are reported in Table 6.1.

The effective length of the membrane is computed as [4] = [1] - [2] - [3] = 21.5 cm^2, while the free volume for air is computed as [9] = [5] - [6] - [7] - [8] = 745 cm^3. Membrane holder 1 is screwed on the inlet flange: therefore, it has a small hole that guarantees the gas inlet. On the other side membrane holder 2 has a annulus shape, since the quartz tube that contains the UV-lamp needs to be inserted in the central hole. The membrane holder can slide on the reactor length, up to the opposite flange: the contact between the membrane holder and the flange is made by silicone grease. The quartz tube is sealed to the reactor, with a Teflon gasket. The opened reactor is reported in Fig. 6.4.
Furthermore, the reactor is equipped with two sampling points: one at the gas inlet, the other at the gas outlet, made by a silicon rubber septum. Employing this reactor has several advantages, for example: (i) with respect to the previous one, the UV radiation intensity is maximized, since the membrane is orthogonal to the light flux; (ii) the dimen-

Table 6.1: Construction details of the reactor

Part	Dimension	Value [cm]	Area [cm^2]	Volume [cm^3]
Reactor	Length	26.7 [1]		
	Internal diameter	6.55		
	External diameter	7.0		
	Total volume			899.7 [5]
Flange	Thickness	0.8		
	Diameter	10.75		
Membrane holder 1	Thickness	2.55 [2]		
	Diameter	4		
	Volume			33.66 [6]
Membrane holder 2	Thickness	2.65 [3]		
	External diameter	4		
	Internal diameter	2.5		
	Volume			21.98 [7]
Quartz tube	Length	20.2		
	Diameter	2.5		
	Volume			99.16 [8]
Membrane	Diameter	4		
	Length	26.7		
	Effective length	21.5 [4]		
	Surface		270.2	
	Free volume			745 [9]

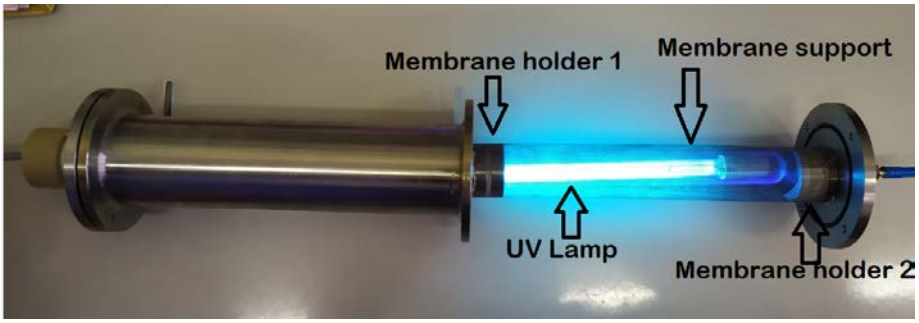

Figure 6.4: Photoreactor, split view

sions are limited; (iii) it is very versatile, since the membranes can be easily changed, the lamp can be changed too (provided it suits in the quartz tube) and the diameter of the membrane can be varied and optimized, changing the membrane holders at the top and the bottom.
An improvement could be the insertion in the reactor of a temperature controller, to monitor the temperature inside the reactor, equipped also with a hygrometer, to study the reaction in different condition of temperature and humidity.

6.1.2 Arnold diffusion cell

To pollute the air stream with methanol before entering the reactor, the Arnold diffusion cell is employed, Fig. 6.5. The cell is formed by a narrow tube filled with 41 g of pure methanol. The cell is immersed in a melting-ice bath (at around 0℃) in order to keep low the amount of contaminant present in the vapor phase. The methanol is therefore maintained during experiments at the same temperature and pressure. On the top of the cell the air flows: air has a negligible solubility in methanol, and it is chemically inert to the pollutant. Methanol vaporizes and diffuses into the gas phase: the rate of vaporization may be physically measured and expressed in terms of the molar mass flux.

The concentration of methanol in the gas phase is function of different parameters: the vapor pressure of the pollutant (which depends on the temperature), the air flow rate, the distance between the liquid top and the gas flow. Increasing the air flow rate has the effect of decreasing the methanol vapor fraction.

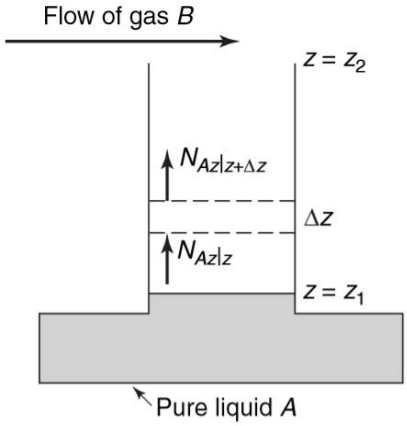

Figure 6.5: Arnold diffusion cell

6.1.3 Lamps

In this work, two lamps are employed, they are briefely described in the following sections.

6.1.3.1 UV-A Lamp

The lamp is purchased by Led Point. It is a strip (length 5 meters), consistued by 300 Leds (60 Leds/m): the strip can be cutted every 6 Leds (10 cm). The emission wavelength is 365 nm (UV-A). Its spectral flux is estimated as 300mW/m. (The spectral flux is the radiant energy emitted, reflected, transmitted or received, per unit time, per unit frequency or wavelength). The employed strip is long 90 cm, and it is rolled on a aluminum support to better dissipate the heat produced by the LED strip. The support is holed in the center and, to better dissipate the heat, compressed air is flown inside.

6.1.3.2 UV-C Lamp

This lamp is purchased by Light Progress, it is UV-Stylo E-16. The emitted wavelength is 254 nm (UV-C) and it has a power of 16 W. In previous work (*Lauria A. M.*, 2016) it has been characterized by means of a photometric analysis. The irradiance flux density is computed, (it is the radiant flux received by a surface per unit area, and its dimension is [W/m^2]. The measure is carried out employing a digital photo-radiometer (HD 9021, Delta Ohm), with a UVC probe (LP 9021, Delta Ohm). It is used to assess the light flux along the lamp length. Two configurations are explored. In the first one the probe is

placed perpendicular with respect to the radiation: it therefore simulates the presence of the membrane in the scaffold of the previous photoreactor. Figure 6.6a represents the irradiance flux density as a function of the lamp coordinate: the irradiance is maximized at z=18 cm. Eleven measures at different coordinates are taken (step size = 3 cm). The calculated average irradiance flux density is therefore 1.35 W/m^2.

In the second arrangement, the probe is placed frontally with respect to the lamp, in a similar way of the actual reactor. Eleven measures are carried out, varying the position of the probe along the lamp (step size = 3 cm, distance from the lamp = 1.5 cm). The maximum flux density is obtained at z=9 cm, Fig. 6.6b. The averge flux density in this case is 13.84 W/m^2. These results confirm that the flux intensity is maximized in the second arrangement, in which the membrane is coaxial with respect to the lamp (the intensity is one order of magnitude bigger in the second case, with respect to the first one). Furthermore, the distribution along the lamp coordinate is not uniform: there is a maximum intensity at different lengths.

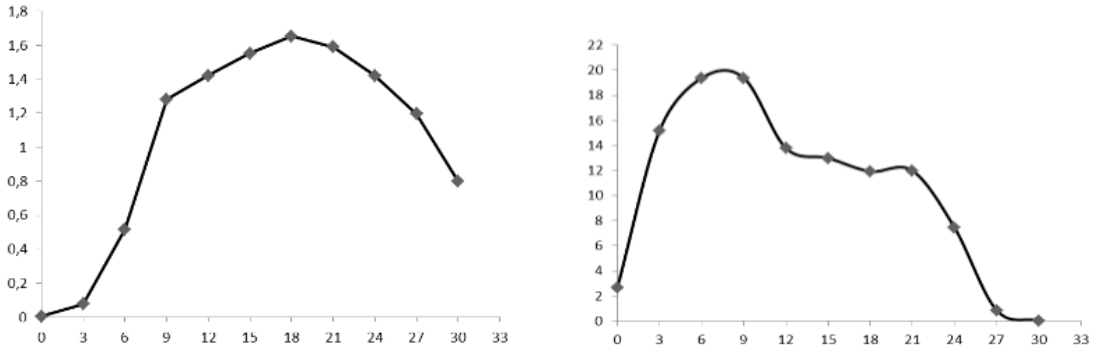

(a) *Perpendicular configuration.* **(b)** *Co-axial configuration.*

Figure 6.6: Irradiance Flux Intensity function of the coordinate of the lamp in two configurations (*Lauria A. M*, 2016)

6.2 GC-MS analysis

The samples withdrawn from the reactor by means of a plastic syringe are injected and analyzed with gas chromatography coupled with mass spectrometry. The time-temperature program is reported in Fig. 6.7. The temperature inside the oven is kept isothermal at 60℃ for 10 minutes, then there is a ramp from 60 to 250℃ at 20℃/min, the final temperature is kept isothermal at 250℃ for 3 minutes.

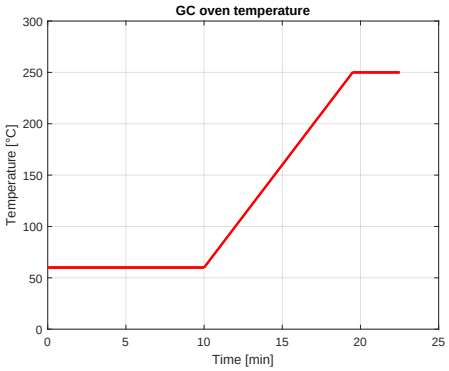

Figure 6.7: GC oven temperature

A sample chromatogram is reported in Fig. 6.8. Different peaks are analyzed, namely the peak at m/z=31 (first row), 44 (second row), 60 (third row), while the first and second column refer to different sampling time: initial time ($t = 0$ min) and final time ($t = 360$min). The first peak (m/z = 31) refers to molecular oxygen present in the air, while the second (with higher retention time) refers to methanol. It is clear that methanol concentration decreases over time. Also, there is a small peak that is present at time $t = 360$ min, which corresponds to methyl formate formation (also in fragment m/z = 60). Fragments 44 takes into account the formation of carbon dioxide during the reaction: the first intense peak is the carbonic anhydride present in the air, while the second small peak is due to the reaction.

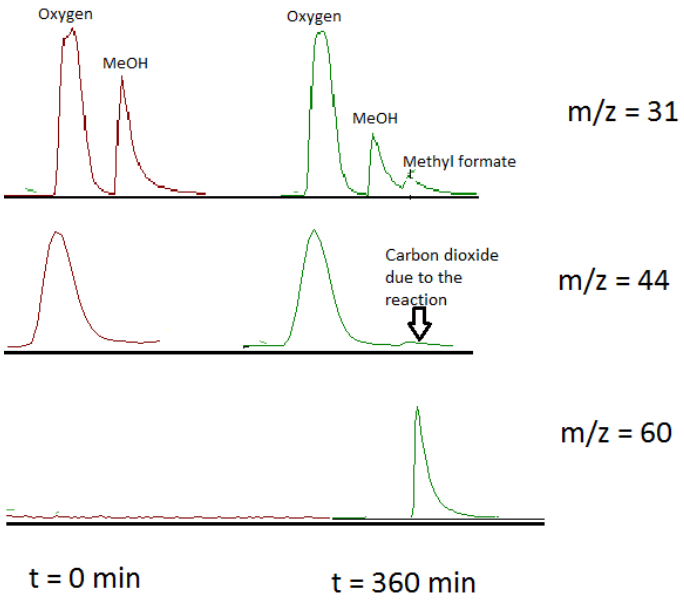

Figure 6.8: GC chromatogram: SIR fragments: m/z = 31, 44, 60 at time 0 (red curves) and 360 minutes (green curves)

Table 6.2: Parameters of GC-MS analysis

Parameter	Value
Injector temperature [℃]	230
Split ratio [-]	5
Split flow [mL/min]	25
Carrier flow [mL/min]	5
Gas saver time [min]	0
Transfer line temperature [℃]	250
Ionic source temperature [℃]	260
Mass range (full scan) $[m/z]$	25-380
Fragments (SIR) $[m/z]$	29, 31, 44, 60

The parameters of the GC-MS are synthetized in Table 6.2: the injector, transfer line, ionic source temperatures are there reported. The analysis are carried out by means of a 100µL gas loop: it therefore allows to work always with the same quantity of the sample, without the need to use an internal standard. The injection is characterized by a split of 5 (i.e. one part enters in the column, 5 parts are purged). Data acquisition are done both in full scan, from 25 to 380 m/z, both in SIR mode: the fragments are reported in the table.

In Figure 6.9a-6.9b are reported mass spectrum respectively for methanol and methylformate (a by-product that forms during the reaction). Methanol main fragments are=31,32,29, smaller peaks are=15,30,28,33. Methanol parent peak is at m/z=32, however the base peak is at m/z=31: this peak is used to carry out the quantitative analysis. It is important to recall that 31 fragment is due also to the atmospheric oxygen present in the air. Methyl formate main fragments are=31,32,29,60, smaller peaks are=15,30,28,33,59,61. Peaks at m/z=$\{$29,31,32$\}$ are common to methanol and methylformate. For this reason, when the byproduct starts to be produced, a double peak appears. Methyl formate has a fragment ion peak at m/z=60, which is peculiar of this compound, and it is used to carry out integration. Carbonic anhydride, instead as a peculiar peak m/z=44.

For a quantitative analysis a calibration curve is employed. Methanol samples at different temperatures (placed in a climatized chamber) are used. Namely, five different temperatures are explored: -30,-40,-45,-50,-60℃. The vapor phase composition in equilibrium with the liquid one is calculated by means of the Raoult-Dalton equation:

$$y_i p = x_i \gamma_i p_i^{sat}(T) \tag{6.1}$$

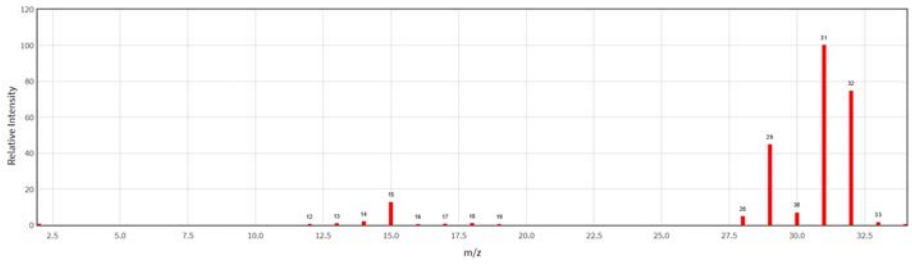

(a) *Methanol.*

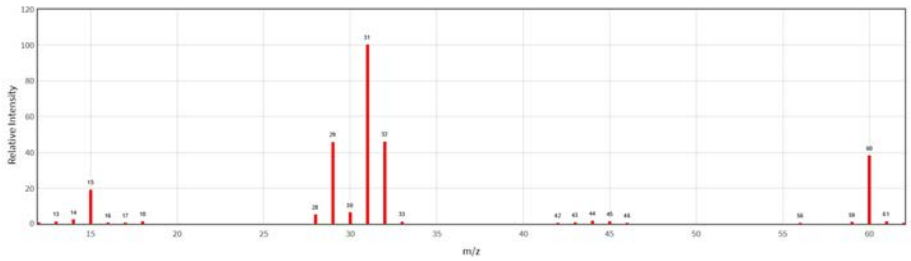

(b) *Methyl formate.*

Figure 6.9: Mass spectra

where y_i and x_i are the molar fractions in the vapor and in the liquid phases, respectively, $p_i^{sat}(T)$ is the saturation pressure at the temperature T, γ_i is the activity coefficient of species i. The liquid is pure methanol, so the activity coefficient can be assumed unitary, also the liquid molar fraction x_i. The saturation pressure is retrieved in process simulator software ProII, function of the temperature. Assuming that the pressure is atmospheric, the vapor fraction is calculated, simplifying Eq. 6.1, to yield:

$$y_i = \frac{x_i \gamma_i p_i^{sat}(T)}{p} = \frac{p_i^{sat}(T)[kPa]}{101.325[kPa]} \tag{6.2}$$

The bubble point is computed with Soave-Redlich-Kwong equation in ProII process simulator. In Fig. 6.10 there are reported the experimental points, marked with stars and the fitted curve (continuous line). Furthermore, error bars are reported: for each of these points at least 4 measurements have been done. The y-axis reports the peak area on the GC spectrum, while on the x-axis there is the vapor molar fraction of methanol, according to Eq. 6.2 expressed in parts per million [ppm]. The fitting is linear, therefore the expression that links area to vapor fraction is the following:

$$A = 298077 \cdot y \tag{6.3}$$

where A stands for GC area, where y stands for methanol vapor molar fraction in ppm.

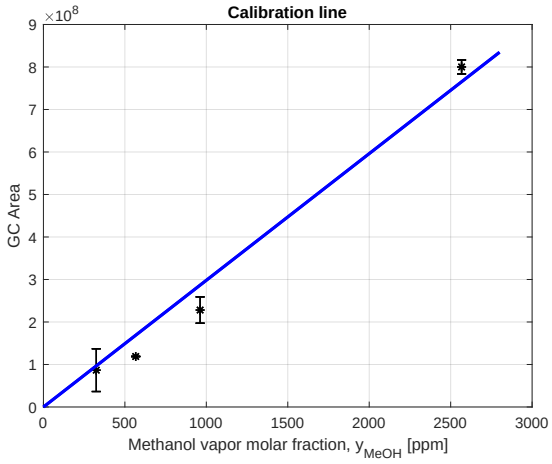

Figure 6.10: GC calibration line

6.3 Photocatalytic tests

The sequence of operation in a photocatalytic test follow this procedure:

1. The air (with the pollutant) flows continuously in the reactor, from the inlet to the outlet, until the concentration of methanol at the inlet sampling point is equivalent to the concentration of the outlet sampling point. The reactor in this way is a sort of continuous PFR, the pump is off, this conditioning phase lasts around 1 hour. The air flowrate is controlled via a flowrate controller, (labeled as FIC in Figure 6.1): during this phase, is 500 mL/min (which corresponds to the 100% valve opening). The flowrate is set at maximum to decrease as much as possible the methanol vapor fraction in the inlet. FI (Flowrate Indicator, as it is labeled in Fig. 6.1), shows a value of 470 mL/min, due to small leakage of air in the Arnold cell.

2. As soon the two concentration at the inlet and the outlet are similar, two valves are switched. Namely, they are: the valve that controls the feed to the reactor from the reservoir and the one that allows the stream to exit the reactor. Switching the valve allows to switch the reactor from continuous to batch. At the same time the recirculation pump is switched on, allowing the recycling of the non-reacted methanol to the top of the reactor. This second phase ends when the concentration at the top is similar to the one at the bottom sampling point, and it lasts around 1 h. The air flow rate that circulate in the reactor is function of the opening of the bypass of the pump: in this case the opening is set to 46% of the total (flowrate 230 mL/min). Opening or closing the valve has a direct impact on the residence time

on the reactor.

3. At the end of these two conditioning phases, the lamp is switched on: this moment is considered as ”time zero”, used to define the initial concentration of pollutant (c^0_{MeOH}).

4. The experiment time: during this time, the lamp and the pump are switched on. Samples are withdrawn from the reactor with a frequency of one every 30 minutes. The reaction time is set on 300-360 minutes. The samples are analyzed by means of GC-MS.

5. When the experiment time ends, the last phase of ”cleaning” is carried out: this time, ”clean” air, without the pollutant is used to strip away from the reactor and to desorb methanol molecules that might be adsorbed on the membrane surface. This last phase lasts until the concentration of the pollutant is negligible.

Each photocatalytic test (as it is described) is repeated for each membrane 2/3 days.

6.3.1 Reaction parameters

In order to quantify the photocatalytic activity two parameters are employed (methanol conversion, methanol mole reacted per catalyst load). The conversion is defined, assuming that the number of moles does not vary, according to this equation:

$$X_{MeOH} = \frac{y_{MeOH,0} - y_{MeOH}(t)}{y_{MeOH,0}} \tag{6.4}$$

in this Equation $y_{MeOH,0}$ and $y_{MeOH}(t)$ are respectively the molar fraction of methanol at time 0, and at time t. The approximation of constant number of moles holds, due to the very low content of methanol in the air (in the range of ppm).

The second index is the number of moles reacted normalized with catalyst load. This index is useful, if the comparison between different membranes, catalysts, reactor setups are wanted. Assuming to work with ideal gas law, it is possible to calculate the total number of moles as:

$$n_{tot} = \frac{pV}{RT} \tag{6.5}$$

where R is the gas constant ($8.314\,\mathrm{J\,mol^{-1}K^{-1}}$), p is the pressure (101325 Pa), V is the volume (745 cm^3), T is the temperature in K. The temperature inside the reactor is maintained at room temperature (around 23℃). Employing the total number of moles, it is possible to compute the reacted mole of methanol with the following formula:

$$n_{react}(t) = n_{MeOH,0} - n_{MeOH}(t) \tag{6.6}$$

and, finally, it is possible to calculate the moles reacted per catalyst loading, dividing the results of the Equation 6.6 with the grams of the catalyst present in each membrane (the value is obtained via TGA analysis).

$$\tilde{n} = \frac{n_{react}(t)}{W_{cat}} \tag{6.7}$$

in which W_{cat} is the weight expressed in grams of the catalyst, while $\tilde{n}$ is expressed in [moles/g].

6.3.2 Preliminary tests

Before conducting the photocatalytic tests, several preliminary tests are carried out to verify the absence of factors that, coupled with photocatalysis might lead to methanol abatement. This test are called ”blank test”. Several tests are carried out, in particular: (i) catalytic membrane without lamp, (ii) polymeric membrane without lamp and catalyst, (iii) polymeric membrane without catalyst, but illuminated, (iv) plastic mesh without lamp, (v) plastic mesh with lamp. All these test lead to the conclusion that these factors are not responsible of methanol abatement.
It is worth to underline that, with respect to other works (*Lauria A. M.*, *Bandiziol N.*) the reactor in this work is kept isothermal at 25℃, while in the previous work the reactor was kept at 50℃. Furthermore, unlike other tests (*Lauria A. M.*, *Folli M.*), the methanol is less concentrated at the inlet. The function $1-X$ (1 - methanol conversion) is reported in Fig. 6.11.-6.12. The catalytic performance of each catalyst is briefly described: the mean conversion is computed, averaging the conversion of the different days of reaction.

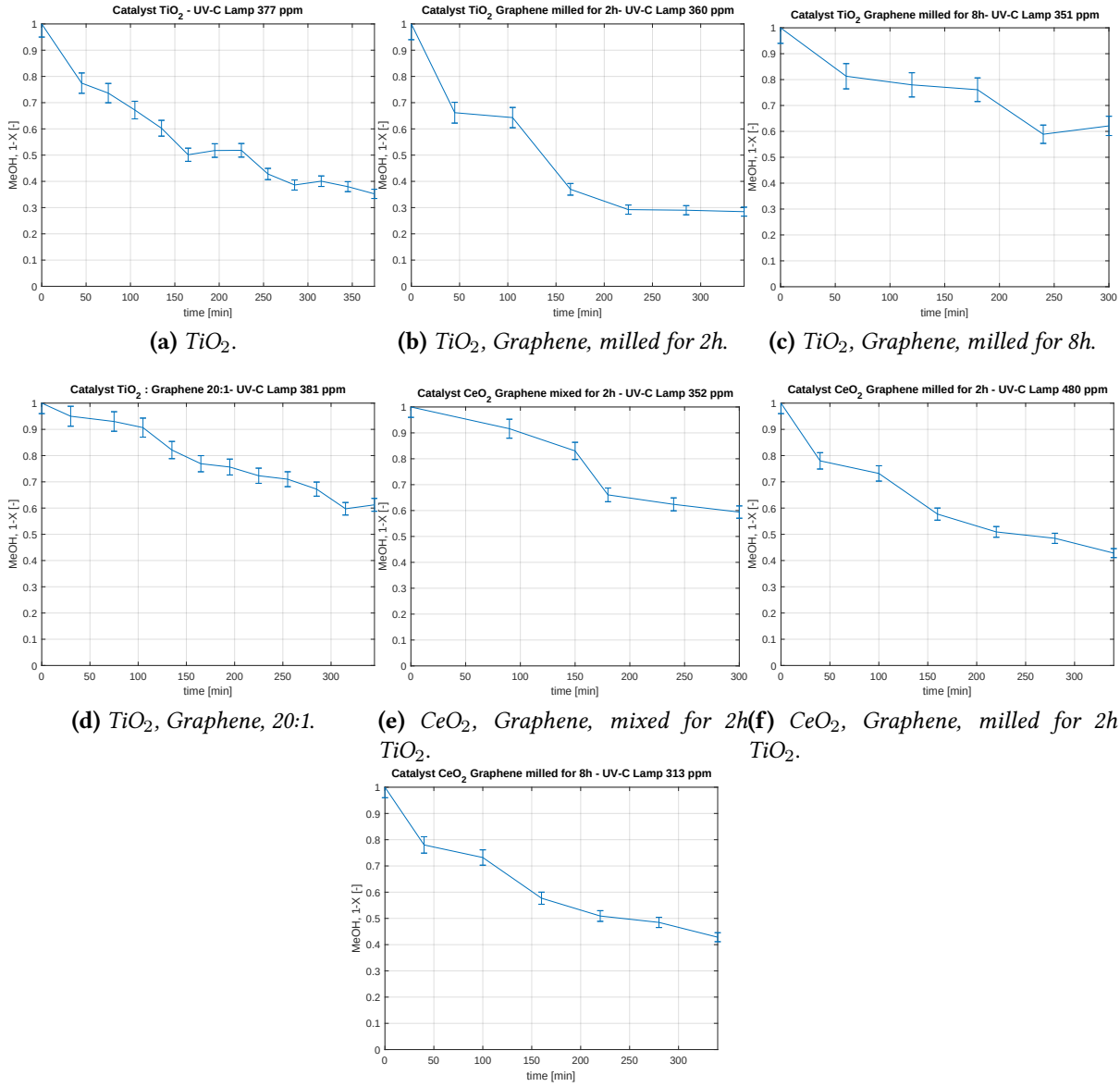

(a) *TiO_2.* **(b)** *TiO_2, Graphene, milled for 2h.* **(c)** *TiO_2, Graphene, milled for 8h.*

(d) *TiO_2, Graphene, 20:1.* **(e)** *CeO_2, Graphene, mixed for 2h TiO_2.* **(f)** *CeO_2, Graphene, milled for 2h TiO_2.*

(g) *CeO_2, Graphene, milled for 8h.*

Figure 6.11: Photocatalytic tests, with UV-C Lamp

6.3.3 Catalysts performances

1. The catalyst tested is TiO_2 P25.

   This catalyst is tested with UV-A Lamp for three days. In different works, the performance of the catalyst improves with the time of exposure to UV light: for that reason, photodegradation is tested for different days. However, in this case, the radiation flux is too low to trigger a photocatalytic reaction with a significant methanol abatement.

   Then, the catalyst is employed with UV-C Lamp. The initial concentration of methanol is 377 ppm. The final methanol vapor fraction (after 375 minutes) is 132 ppm, (total conversion of 65%). The results are reported in Fig. 6.11a

2. The catalyst tested is TiO_2 Graphene, milled for 2h.

   Also in this case, the catalyst is employed with UV-A Lamp but it does not give any significant results.

   This catalyst is tested also with UV-C Lamp. The conversion after 345 minutes is 71.5%, which is slightly better than the pure titania catalyst. The results are reported in Fig. 6.11b. The final methanol vapor fraction is 102 ppm.

3. The catalyst tested is TiO_2 Graphene, milled for 8h.

   The performances with UV-A Lamp are poor also in this case.

   The membrane is tested employing UV-C Lamp. The conversion after 300 minutes of irradiation is 37.9%, (final concentration of 218 ppm). The performance of this catalyst are poor, with respect both to pure titania and to titania, graphene (milled for 2h): it seems that longer milling time does not imply better catalytic performances The results are reported in Fig. 6.11c.

4. The catalyst tested is TiO_2 Graphene 20:1.

   Employing UV-A radiation does not lead to any significant results in term of conversion.

   The inlet methanol vapor fraction is 381 ppm, the minimum vapor fraction after 345 minutes is 233 (with an overall conversion of 38.77%). The kinetic behavior is reported in Fig. 6.11d.

5. The catalyst tested is TiO_2 Graphene 10:1.

The catalytic activity employing UV-A radiation are not significative.
The results obtained in this case are not promising, since, after 250 minutes, the conversion is low (around 10%). The small performances of this catalyst can be due to the low content of titanium, with respect to graphene.

6. The catalyst tested is TiO_2/CeO_2 Graphene mixed for 2h TiO_2.
   The catalyst under UV-A irradiation does not provide significative results.
   The initial concentration of methanol is 352 ppm, after 300 minutes, the final concentration is 209 ppm (the conversion is 40.6%). The behavior of this catalyst are reported in Fig. 6.11e.

7. The catalyst tested is TiO_2/CeO_2 Graphene milled for 2h TiO_2.
   The catalyst is tested with UV-A Lamp, starting from a concentration of 692 ppm. The final concentration at 270 minutes is 526 ppm, resulting in a total conversion of 24%.
   The catalyst is employed also with UV-C. The test uses an inlet methanol vapor fraction of 480 ppm, and after 340 minutes, the final conversion is 0.5717 (206 ppm). The results are reported in Fig. 6.11f.

8. The catalyst tested is CeO_2 Graphene milled for 8h. The inlet vapor fraction of methanol is 313, after 300 minutes the conversion is 39.97%, leading to an outlet vapor fraction of 188 ppm. The results are reported in Fig. 6.11g.

Then, a fitting procedure is done: the results are reported in Fig. 6.12. The fitted parameters of L-H equation are reported in Table 6.3: the first column is the kinetic constant k_0, the second column refers to the adsorption constant K, while the third column refers to the function that needs to be minimized (SSE: sum of squared errors). Looking at the results in Table 6.3 it is possible to infer that the kinetic constant k_0 is in all the cases higher with respect to pure titania: therefore, the different catalysts are able to speed the reaction with respect to the one activated by the pure titania. The higher kinetic constant is in the catalyst TiO_2 Graphene milled for 2 hours (3.2386 min^{-1}). This catalyst is the one that can provide, after 6 hours of reaction, the highest absolute methanol conversion (71.5%).

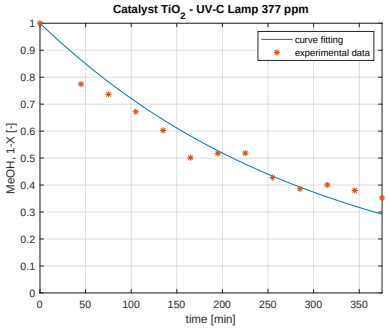

(a) *TiO_2.*

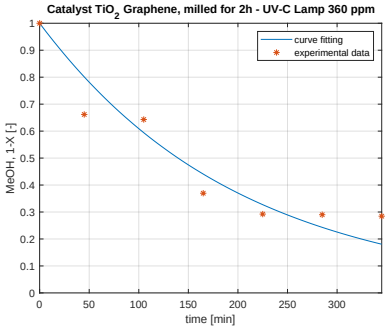

(b) *TiO_2, Graphene, milled for 2h.*

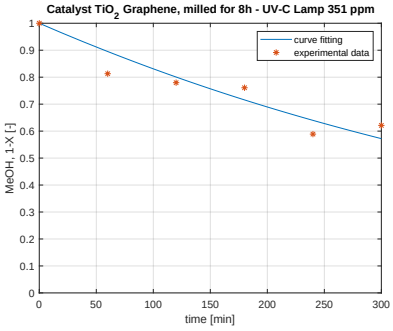

(c) *TiO_2, Graphene, milled for 8h.*

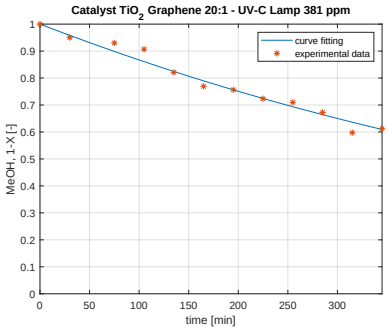

(d) *TiO_2, Graphene, 20:1.*

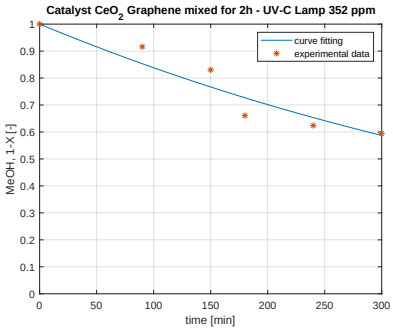

(e) *CeO_2, Graphene, mixed for 2h TiO_2.*

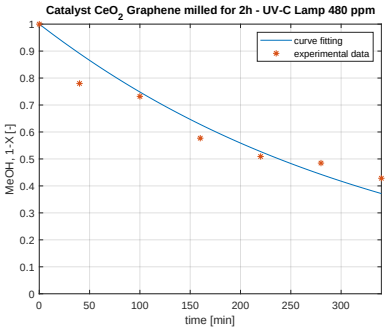

(f) *CeO_2, Graphene, milled for 2h TiO_2.*

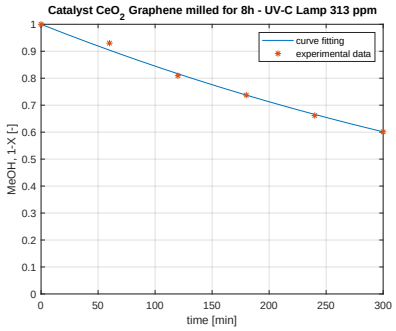

(g) *CeO_2, Graphene, milled for 8h.*

Figure 6.12: Photocatalytic tests, with UV-C Lamp and fitted L-H isotherm (blue continuous curve)

Table 6.3: Fitted parameters of L-H isotherm

Catalyst	k_0 [min^{-1}]	$K \times 10^3$	SSE
TiO_2	1.07	3.10	0.17446
TiO_2 Graphene milled 2h	3.24	1.53	0.20268
TiO_2 Graphene milled 8h	1.66	1.26	0.11936
TiO_2 : Graphene 20:1	1.57	0.918	0.073696
TiO_2/CeO_2 Graphene mixed 2h	1.15	1.19	0.11531
TiO_2/CeO_2 Graphene milled 2h	2.43	12.0	0.14325
CeO_2 Graphene milled 8h	1.25	1.36	0.02728

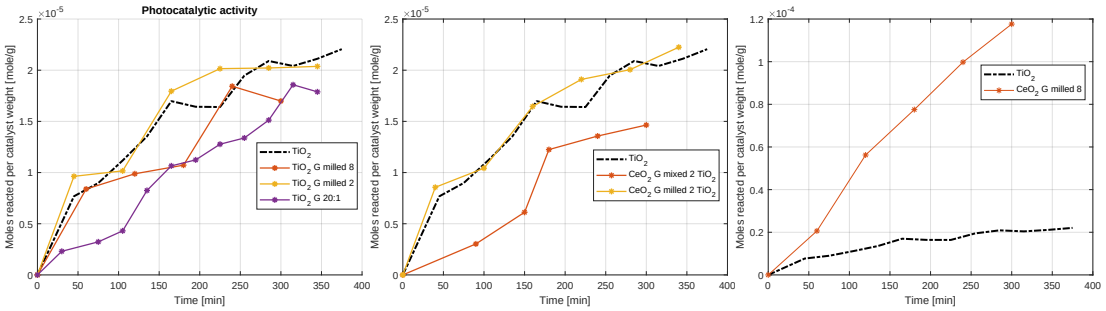

(a) *TiO_2 Graphene based catalysts.* **(b)** *CeO_2, Graphene based catalysts.* **(c)** *CeO_2, Graphene, milled for 8h.*

Figure 6.13: Specific photocatalytic activities

6.3.4 Results discussion

During the reaction, along with the abatement of the pollutant, the formation of two by-products is found: namely carbon dioxide and methyl formate, employing GC-MS. However, the formation of these two compounds is not quantified, since the calibration curves are in this case difficult to be built.

Looking at the final concentration of methanol for each catalyst, it is possible to recognize that no catalyst is able to perform a complete methanol abatement (unitary conversion). The degradation rate can be ehanced (leading to smaller reaction time): some optimization processes are needed to improve the catalytic performance of this nanostructured materials. The performance is evaluated also taking into account the effective weight of the catalyst, (this information is obtained by means of the residue computed with TGA), according to this formula:

$$\frac{n_{react.}}{W} = \frac{X(t) y^0_{MeOH} pV}{RTW} \tag{6.8}$$

where $n_{react.}$ is the number of reacted moles, $X(t)$ stands for the conversion at time t and y^0_{MeOH} is the initial vapor fraction of methanol (at time $t = 0$). Figure 6.13 compares the specific photocatalytic activities of the different catalyst with respect to the ”pure” titania catalyst, marked with discontinuous black line.

In Figure 6.13a the titania-graphene based catalysts are compared: the worst photocatalytic activity is displayed by the catalysts TiO_2 Graphene 20:1, while a similar activity to the ”benchmark” titania is displayed by the catalyst TiO_2 Graphene, milled for 2 hours. The milling time does not provide the catalyst a better performance, since the catalyst

TiO_2 Graphene, milled for 2 hours shows a higher photoactivity with respect to the one milled for 8 hours (it is worth to recall that in the sample milled for 2 hours titania is added (700 mg)).

In Figure 6.13b the comparison between ceria-based catalyst and titania is carried out. The catalyst CeO_2 Graphene milled for 2 hours with the addition of TiO_2 displays a catalytic activity similar to the pure titania, while the sample in which ceria and graphene are not milled but only mixed have a lower performance in terms of moles reacted per gram of catalyst. It is possible to claim that mechano-chemical synthesis, in this case, has improved the catalytic performances.

In Figure 6.13c the comparison between CeO_2 Graphene, milled for 8 hours is carried out with respect to ”pure” titania. This catalyst is characterized by a small amount measured by means of TGA. For that reason, the specific photocatalytic activity is so high, even though the conversion after 300 minutes is not very high (39.88%). The enhancement of the performance is due to the low amount of catalyst present on the surface (32.53 mg with respect to other catalyst that have 200-300 mg). This behavior can be explained with some screening effects: the excessive loading of the catalyst could have an adverse effect on photocatalysis. For that reason, an optimization process should be carried out to optimize the concentration of catalyst on the fibers.

Further studied can be carried out to evaluate the influence on the kinetics of methanol concentration, in particular it would be interesting to explore reaction rates at even lower methanol concentration, in order to better simulate real pollution conditions.

Furthermore, it is possible to recognize that the milling time does not have a profound effect on the catalysis: the performances of Titania Graphene milled for 2 and 8 hours are similar.

Conclusions

The objective of this work was to design a membrane photoreactor to perform methanol photocatalytic oxidation and to evaluate different nanostructured catalysts obtained with mechano-chemical synthesis and top-down processes. Also, the evaluation of performances allowed to assess the improvement of the catalyst activity given by the synthetic routes employed. Membrane are prepared via electrospinning, while the catalysts are deposited by means of electrospraying. The membranes display a non-completely uniform distribution, due to the very large area the electrospraying jet needs to cover.

UV-A light is employed: however, due to the low irradiance flux intensity it was not able to trigger photocatalytic reaction: only the catalyst formed by cerium oxide milled for 2 hours with graphene, shows a modest activity towards methanol; the other seven catalysts are not able to favor the reaction.

Then UV-C is employed. The most promising catalyst (TiO_2 Graphene, milled for 2 hours) is responsible for a final conversion of 71.5% after 6 hours of reaction. The catalysts obtained via mechano-chemical synthesis have specific performances similar to the benchmark titanium dioxide, further studies are needed to evaluate the milling time in the catalytic performances. It is shown, however, that the milling process favors the intimate contact between catalysts, which are more active with respect to catalysts that are simply mixed together.

This work dealt with innovative catalysts prepared with novel routes, new photoreactor and membrane-light arrangement, however some future studies are needed to investigate further this issue. For example, the catalyst loading on the membrane needs to be optimized to avoid screening effects that can lower the performances. Then, smaller methanol fraction can be used in the reactor inlet to better simulate real pollution situations.